

**OPTIMIZED DESIGN OF THE OFFSHORE  
MONOPILE FOUNDATION UNDER EXTREME  
CONDITION**

**LOH KEIN YUIN**

**A project report submitted in partial fulfilment of the  
requirements for the award of the degree of  
Bachelor of Engineering Civil Engineering  
(Environmental) with Honours**

**Faculty of Engineering and Green Technology  
Universiti Tunku Abdul Rahman**

**May 2025**

## DECLARATION

I hereby declare that this project report is based on my original work except for citations and quotations which have been duly acknowledged. I also declare that it has not been previously and concurrently submitted for any other degree or award at UTAR or other institutions.

Signature : \_\_\_\_\_

Name : LOH KEIN YUIN


ID No. : 20AGB03649

Date : 16th May 2025

### APPROVAL FOR SUBMISSION

I certify that this project report entitled **“OPTIMIZED DESIGN OF THE OFFSHORE MONOPILE FOUNDATION UNDER EXTREME CONDITION”** was prepared by **LOH KEIN YUIN** has met the required standard for submission in partial fulfilment of the requirements for the award of Bachelor of Civil Engineering (Environmental) with Honours at Universiti Tunku Abdul Rahman.

Approved by,

Signature :  \_\_\_\_\_

Supervisor : Dr. Zafarullah Nizamani

Date : 19.05.2025

The copyright of this report belongs to the author under the terms of the copyright Act 1987 as qualified by Intellectual Property Policy of Universiti Tunku Abdul Rahman. Due acknowledgement shall always be made of the use of any material contained in, or derived from, this report.

© 2025, Loh Kein Yuin. All right reserved.

Specially dedicated to  
my supervisor, lecturers, beloved mother,  
father and two loving sisters.

## **ACKNOWLEDGEMENTS**

I would like to thank everyone who had contributed to the successful completion of this project. I would like to express my gratitude to my research supervisor, Dr. Zafarullah Nizamani for his invaluable advice, guidance and his enormous patience throughout the development of the research.

In addition, I would also like to express my gratitude to my loving parents, sisters, lecturers and friends who had helped and given me encouragement throughout my tough and challenging times.

# **OPTIMIZED DESIGN OF THE OFFSHORE MONOPILE FOUNDATION UNDER EXTREME CONDITION**

## **ABSTRACT**

This thesis investigates advanced analysis and design methodologies for monopile foundations supporting offshore wind turbines, leveraging the PISA (Pile Soil Analysis) framework based on Timoshenko beam theory. The study emphasizes the role of monopile foundations in ensuring structural integrity and long-term operational performance in challenging offshore environments. The initial chapters establish the core design principles, including structural components, theoretical underpinnings, load transfer mechanisms, and methodological approaches. Critical factors influencing design such as site-specific geotechnical properties, hydrodynamic forces from wave action, and wind-induced loading are examined in detail. To identify the governing design condition, a comprehensive load combination analysis was conducted. The most severe case was found to be an extreme operating gust at rated wind speed combined with a 50-year return period wave height. Under these conditions, and for a water depth of 60 meters, a lateral eccentric load of 5,777 kN applied at 90 meters height results in an overturning moment of 709 MNm at the mudline. The study integrates both one-dimensional and three-dimensional finite element modelling techniques to capture the structural behaviour under extreme loads more accurately. A key component of the analysis involved the use of PLAXIS Monopile Designer software, which enabled a rigorous simulation of soil-structure interaction based on site-specific parameters. Through the integration of PISA-based soil response curves and finite element modelling, the tool was used to optimize the foundation design, ensuring reliability and material efficiency. The resulting optimized monopile foundation for a 6.0 MW offshore wind turbine features an outer

diameter of 8 meters, a wall thickness of 0.06 meters, an embedment depth of 43 meters, and a total length of 103 meters. The proposed design demonstrates improved performance and cost-effectiveness while complying with modern offshore design standards.

Keywords: Offshore, Wind Turbine, Monopile, Structural Modelling, Plaxis Monopile Designer

Subject Area: TC1501-1800 Ocean engineering



## TABLE OF CONTENTS

<b>DECLARATION</b>	<b>ii</b>
<b>APPROVAL FOR SUBMISSION</b>	<b>iii</b>
<b>ACKNOWLEDGEMENTS</b>	<b>vi</b>
<b>ABSTRACT</b>	<b>vii</b>
<b>TABLE OF CONTENTS</b>	<b>ix</b>
<b>LIST OF TABLES</b>	<b>xiv</b>
<b>LIST OF FIGURES</b>	<b>xv</b>
<b>LIST OF SYMBOLS / ABBREVIATIONS</b>	<b>xvii</b>
<b>LIST OF APPENDICES</b>	<b>xx</b>

## CHAPTER

<b>1</b>	<b>INTRODUCTION</b>	<b>1</b>
1.1	Background	1
1.2	Problem Statements	2
	1.2.1 Problem Background: Climate on Equator	3
	1.2.2 Problem Motivation: The Demand for Renewable Energy	3
	1.2.3 Problem Description	4
	1.2.4 Justification of The Research: Sustainable Issues	5
	1.2.5 Previous Work	6

1.2.5.1	Performance Evaluation of The Monopile Foundation Using PISA Methodology Under Extreme Loading Conditions In Malaysia	6
1.2.5.2	Design and Fatigue Analysis of Monopile Foundation to Support the DTU 10 MW Offshore Wind Turbine	6
1.2.5.3	Renewable Wind Energy Resources in Offshore Low Wind Speeds Regions Near the Equator	7
1.3	Aims and Objectives	7
1.4	Research Methodology (Critical Appraisal)	8
1.4.1	p-y method	8
1.4.2	Pile Soil Analysis (PISA) Method	9
1.5	Scope of Work	10
1.6	Limitations of Work	10
1.7	Outline of The Thesis	10
<b>2</b>	<b>LITERATURE REVIEW</b>	<b>11</b>
2.1	Type of Wind Turbines	13
2.1.1	Horizontal Axis Wind Turbine	14
2.1.2	Vertical Axis Wind Turbine	14
2.1.3	Wind Turbines for Low Wind Regions	15
2.2	Types of Foundations	16
2.3	Joints Connection for Monopile Foundations	18
2.4	Failure Modes of The Monopile Foundation	19
2.5	Types of Loads	22
2.5.1	Self-weight	22
2.5.2	Live Load	22
2.5.2.1	Cyclic Load by Rotor and Wind Blade	23

	2.5.3 Environmental Loads	24
	2.5.3.1 Aerodynamic Loads	24
	2.5.3.2 Hydrodynamic Loads	26
	2.5.3.3 Current Loads	27
2.6	Type of Soil Properties	27
2.7	Plaxis Monopile Designer	29
	2.7.1 Rule-based Design and Numerical-base Design	30
	2.7.2 Finite Element Model	30
	2.7.3 Timoshenko Beam Theory	33
2.8	Limit States	34
	2.8.1 Ultimate Limit State	34
	2.8.2 Serviceability Limit State	35
	2.8.3 Fatigue Limit State	36
<b>3</b>	<b>METHODOLOGY</b>	<b>37</b>
3.1	Obtaining Site and OWT Data	38
	3.1.1 Offshore Soil Properties of Kuala Terrenganu	38
	3.1.2 Offshore Wind Speed in Kuala Terrenganu	39
	3.1.3 Offshore Wave Properties in Kuala Terrenganu	42
	3.1.4 Offshore Wind Turbine Specifications	42
3.2	Aerodynamic Loading Analysis	43
3.3	Hydrodynamic Loading Analysis	48
3.4	Initial Geometry Estimation	51
3.5	Design Technique	53
	3.5.1 Soil Mode	53
	3.5.2 Calibration Mode	54
	3.5.2.1 Parametrization of Soil Reaction Curves	56
	3.5.3 Analysis Mode	57
	3.5.4 Results Mode	59
	3.5.4.1 Optimizations of Monopile Geometry	60
	3.5.4.2 Construct 3D FEM for Verification	60

<b>4</b>	<b>RESULTS AND DISCUSSIONS</b>	<b>61</b>
4.1	Loads Analysis	61
4.1.1	Self-weight	61
4.1.2	Aerodynamic Load Analysis	62
4.1.2.1	Normal Turbulence Scenario	62
4.1.2.2	Extreme Turbulence Scenario	64
4.1.2.3	EOG Model at Rated Wind Speed	66
4.1.2.4	EOG Model at Cut-out Wind Speed	67
4.1.3	Hydrodynamic Loads Analysis	68
4.1.3.1	One-Year Return Period Wave Profile	72
4.1.3.2	Fifty-Year Return Period Wave Profile	75
4.1.4	Loads Analysis Discussion	78
4.2	Initial Geometry Estimation	81
4.3	Monopile Calibration Modes Results	84
4.4	Plaxis Monopile Designer Results and Discussion	87
4.4.1	Results of Horizontal Force Againsts Lateral Displacement for Optimised Monopile Design	90
4.4.2	Results of Overturning Moment Against Mudline Rotation for Optimised Monopile Design	92
4.4.3	Calibrated Design Space Check	94
4.5	Connection Joint Design	95
4.6	Sustainability Impact from This Research	98
<b>5</b>	<b>CONCLUSION AND RECOMMENDATIONS</b>	<b>100</b>
5.1	Conclusion	100
5.2	Recommendation	102
5.2.1	Consider Environmental and Geotechnical Uncertainties	102
5.2.2	Implement Performance-Based Assessment	102
5.2.3	Refine Numerical Simulations	102

**REFERENCES****103****APPENDICES****110**

## LIST OF TABLES

<b>TABLE</b>	<b>TITLE</b>	<b>PAGE</b>
2.0	Papers on Monopile Foundation Analysis and Design	11
3.1.1	Offshore Soil Profile of Kuala Terengganu	39
3.1.2	Recorded Wind Speed in Abu Kecil	40
3.1.3.1	Wave Data of Abu Kecil	42
3.1.3.2	OWT Specification and Weight	42
3.5.1	Required Parameters for Soil Profile at Site	53
3.5.2	Geometry Datasets of Monopiles for Calibration	40
4.1.1	Total Structural Weight	61
4.1.3.1	Tabulated Results of N	69
4.1.3.2	Calculation for Maximum Wave Height and Period	70
4.1.3.3	Tabulated Results of $H_m$ and $T_m$	71
4.1.3.4	Hydrodynamic Force Parameter and Description	71
4.1.4	Tabulated Data of Metocean Loads	78
4.2.1	Steel Properties of The Monopile	82
4.2.2	Initial Monopile Geometry	83
4.4.1	Optimized Monopile Geometry	88
4.5.1	Transition Piece Geometry	96

## LIST OF FIGURES

<b>FIGURE</b>	<b>TITLE</b>	<b>PAGE</b>
2.1.2	Types of Wind Turbines	15
2.2.1	Spar-supported Floating OWTs	17
2.2.2	Types of Foundation	18
2.6.2.1	Geeneral FE Analysis and Modelling Procedure	30
2.6.2.2	1D FEM Illustration	32
3.1.1	Location of Suriya-B, Kuala Terengganu	38
3.1.2.1	Recorded Wind Direction in Peninsular Malaysia	40
3.1.2.2	Center Location of Abu Kecil	40
3.1.2.3	Distance from The Centre of Abu Kecil to The Nearest OnShore Area	41
4.1.4.1	Horizontal Force Acting on The Structure	78
4.1.4.2	Overturning Moment Acting on The Structur	79
4.3.1	Colour Coding for Respective Geometry Dataset	84
4.3.2	Horizontal Force vs Lateral Displacement for Calibrated Monopile Geometries	84
4.4.1	Interface for The Analysis Mode of The Plaxis Monopile Designer.	87
4.4.2	Horizontal Force (kN) Against Lateral Displacement (m) for 65 m of embedment.	87
4.4.3	Overturning Moment (kMn) Against Mudline Rotation (rad.) for 65 m of embedment.	88
4.4.4	Optimised Monopile Geometry and Soil Layers Generated in Plaxis 3D.	89

4.4.1.1	Horizontal Force (kN) Against Lateral Displacement (m) for 43 m of embedment.	89
4.4.2.1	Overturning Moment (kMn) Against Mudline Rotation (rad.) for 43 m of embedment.	91
4.4.3.1	Final Design Case in The Design Space	94
4.5.1	Cross-section Design of The Transition Piece.	96
4.5.2	Optimised Monopile Design.	97
4.5.3	Conceptual Design of Monopile-supported 6.0 MW Wind Turbine with 43 m Embedment Depth in 60 m Water Depth.	97



## LIST OF SYMBOLS / ABBREVIATIONS

$F_{th}$	wind thrust force, kN
$C_{th}$	thrust coefficient
$\rho_a$	air density, kg/m <sup>3</sup>
$A_R$	rotor swept area, m <sup>2</sup>
$U$	mean windspeed, m/s
$\bar{U}$	windspeed component, m/s
$u$	turbulent wind speed component, m/s
$S$	mean water depth, m
$Z_{hub}$	hub height, m
$M_{wind}$	overturning moment due to wind, kNm
$F_{D,max}$	wave drag force component, kN
$F_{I,max}$	wave inertia force component, kN
$M_{wave}$	overturning moment due to wave, kNm
$k$	wave number
$n$	surface elevation, m
$H_s$	significant height, m
$D_s$	substructure diameter, m
$\rho_w$	water density, kg/m <sup>3</sup>
$H_m$	maximum height, m
$T_s$	significant wave period, s
$T_m$	wave inertia force component, kN

$C_m$	inertia coefficient
$C_d$	wave coefficient
$K_0$	lateral earth pressure coefficient at rest
$h$	monopile head, m
$D_{out}$	outer diameter, m
$t_p$	wall thickness, m
$v_g$	target relative displacement at mudline, m
$W$	pile unit weight, kN/m <sup>2</sup>
$E$	young's modulus, kN/m <sup>2</sup>
$\nu$	Poisson's ratio, kN/m <sup>2</sup>
$s$	wind speed Weibull distribution shape parameter
$L_k$	turbulence integral length scale, m
$U_R$	rated wind speed, m/s
$n_h$	modulus of subgrade reaction, MN/m <sup>3</sup>
$A$	subgrade coefficient
$L_T$	total pile length, m
$U_{out}$	Cut out wind speed, m/s
$t_{TP}$	thickness of transition piece, m
$t_G$	grout thickness, m
$g$	gravity acceleration, m/s <sup>2</sup>
$N$	total number of waves
$D_t$	tower top diameter, m
$D_b$	tower bottom diameter, m
$I_{ref}$	reference turbulence intensity, %
$w_R$	rotor weight, t
$U_{in}$	Cut-in wind speed, m/s
$D_r$	rotor diameter, m
$D_{out}$	outer diameter, m

$t_p$	wall thickness, m
$v_g$	target relative displacement at mudline, m
$\sigma_u$	standard deviation of wind speed
$N_s$	sample size
$U_i$	value for observation, m/s
$f_{1P,max}$	maximum rotor frequency, Hz
$f_{yk}$	ultimate yield strength, MPa
$\gamma_m$	material factor
$\gamma_L$	environmental load factor
$I_p$	moment of inertia, mm <sup>4</sup>
$D_s$	substructure diameter, m
$L_G$	length of grouting, m

**LIST OF APPENDICES**

<b>APPENDIX</b>	<b>TITLE</b>	<b>PAGE</b>
A	Depth Variation Functions	110
B	Publications	111

## CHAPTER 1

### INTRODUCTION

#### 1.1 Background

Energy sources are the foundation of modern society, powering every sector from residential, commercial, transportation, and industrial activities. These sources can be divided into two primary categories: non-renewable and renewable. Non-renewable energy sources include obtaining energy from the combustion of coal, oil, and natural gas. These current conventional methods are finite and emit substantial greenhouse gases upon combustion, thereby contributing to climate change. Conversely, renewable energy sources, including wind, solar, hydroelectric, and geothermal energy, are derived from natural processes that are consistently replenished and generally have a lower environmental impact.

As of 2024, the global energy mix still primarily relies on non-renewable sources, about 70%-80%, but for renewable sources it only accounts for an approximate of 30% (McKinsey & Company, 2023). The global demand for energy however is anticipated to continue growing rapidly with a shift towards cleaner and more sustainable energy sources that is essential to ensure a secure and environmentally friendly energy future. Modern policies such as the Paris Agreement (2015) and global frameworks such as the Sustainable Development Goals (SDGs), particularly on “Goal 7: Affordable and Clean Energy”, also encourages the rapid growth and demands for sustainable energy source alternatives.

In Malaysia, the Sustainable Energy Development Authority (SEDA) is responsible for implementing renewable energy policies like the Renewable Energy Act 2011 and managing Feed-in Tariff (FiT) schemes. The FiT provides financial incentives for renewable energy projects and guarantees certain tariffs according to the energy produces over a fixed periods which attracts investments in renewable

energy (SEDA, n.d.). Not only that, SEDA also provides support and resources for feasibility studies and project developments. Hence, it is agreeable that renewable energy methods are a futuristic alternative to be invested on.

Among Malaysian sources of renewable energy, hydropower is the most prominent source as of 2024 and has been dominating the industry for decades. This is primarily due the abundance of natural streams and available technology in Malaysia. Other sources include solar energy and biomass or biogas which are also gradually progressing in the industry due to rapid technological advancement and supportive government policies. However, wind powered energy is not yet a major contributor to the country's renewable energy mix due to geographical and climatic factors. The tropical climate and equatorial geography generally have lower and less consistent wind speeds. The best potential for large-scale wind power generation in Malaysia would be in the coastal and offshore regions. Higher wind speeds in Malaysian offshore regions provide a promising future for the development of wind energy to contribute to the country's renewable energy mix.

## **1.2 Problem Statements**

The wind speed in Malaysian offshore is relatively low and it only increases with further distances from shore, where the depth of the ocean increases as well. According to Manwell (2024) offshore winds are generally more powerful than those onshore up to 50 kilometres from the coast, with reduced shear and lower natural turbulence. Monopile foundations are support structures for the wind turbines and are usually ideal for depths of 20-40 meters (Wu et. al., 2019). The issue arises during the design of a suitable foundation for offshore wind turbines in greater ocean depths such as 60 meters. Additional depth exerts additional loads to the monopile and hence the design needs to be optimised.

### **1.2.1 Problem Background: Climate on Equator**

The region around the equator, known as the doldrums, typically experiences low wind speeds. This is because the trade winds from both hemispheres converge here, leading to a neutralization effect that results in weaker winds. The Earth's atmospheric circulation patterns like the Hadley cells influence wind speeds. Hadley cells are large-scale atmospheric circulation patterns extending from the equator to about 30° latitude in both hemispheres. They are driven by intense solar heating at the equator, where warm air rises, creating a low-pressure zone. As the air ascends, it cools and moves poleward at high altitudes. Around 30° latitude, this cooler, denser air descends, forming high-pressure zones. The resulting surface winds, known as trade winds, flow back toward the equator. However, where these trade winds converge near the equator, they create an area of low pressure and calm conditions, known as the Intertropical Convergence Zone (ITCZ), leading to reduced wind speeds typical of the doldrums. In offshore regions near the equator, the oceanic conditions further contribute to low wind speeds. The vast expanse of water tends to stabilize the atmosphere, reducing temperature differences that could otherwise drive stronger winds.

### **1.2.2 Problem Motivation: The Demand for Renewable Energy**

Renewable energy is the way forward for a sustainable future. According to Morten and Ben (2021), many big oil and gas companies expect to achieve carbon neutrality by 2050. Carbon neutrality refers to the concept of achieving a net-zero carbon footprint, as encouraged by the United Nations. Thus, there is a rush to develop available alternatives such as wind energy in Malaysia to replace conventional methods for maintaining the country's economic activities. Given the promising wind speeds in offshore regions of the country, wind turbines are a good solution to be analysed and advanced for better construction of wind farms in the future. Although hydropower, solar power, and biogases are in the market, wind power can be an additional asset to the generation of electricity for the country.

### **1.2.3 Problem Description:**

Monopile foundations are not originally designed for deep-water applications beyond 40 meters. In Malaysian offshore zones, where water depth can reach 60 meters, conventional monopile designs experience increased lateral forces and overturning moments. This challenges the structural stability and suitability of standard monopile configurations in deeper marine environments.

Offshore wind turbines are exposed to harsh and unpredictable conditions, such as extreme wind gusts and high return-period waves. Without an optimized design, these extreme load combinations can lead to excessive deformation, instability, or even structural failure of the monopile foundation, jeopardizing the safety and lifespan of the turbine.

Conventional design approaches like the p-y method, while widely used in geotechnical engineering, often fall short when applied to large-diameter monopiles. These methods, initially developed for smaller structures, may not capture the full complexity of soil-structure interactions in offshore environments. As a result, they can lead to overly conservative and costly designs.

Most monopile design methodologies are based on environmental and soil conditions found in regions like the North Sea, which differ significantly from those in Southeast Asia. Malaysia's tropical climate, unique wind patterns, and seabed characteristics demand tailored design strategies. Applying generalized international standards without modification can lead to structural inefficiencies.



#### **1.2.4 Justification of the Research: Sustainable Issues (Environment, Economy, Social)**

The Malaysian government has set ambitious renewable energy targets to reduce its carbon footprint and meet global climate commitments. Offshore wind energy is indefinitely one of the methods to help achieve these goals. However, offshore wind turbines (OWTs) require expertise in engineering design and must extensively consider soil conditions, dead loads, live loads, environmental loads and structure materials to ensure structural stability and longevity. OWT's structures are preferred to be designed in a more cost-effective option, typically monopile foundations to reduce the overall project cost. Since, monopiles are large structures, optimising the dimensions and design for this foundation type is crucial for yielding an economical product that is steady for optimal performance. It is also a concern for the construction phase where marine ecosystems may be heavily disturbed. Hence, an optimised monopile design can minimise environmental impacts. The efforts in researching monopile foundations can stimulate local industry and technological expertise to invest and build a domestic supply chain for wind energy infrastructure. This step will foster economic growth and create skilled employment opportunities in engineering, construction, and maintenance. On a global scale, a growing wind industry in Malaysia will attract international investors and partnership which will further advance the renewable energy sector to achieve sustainability.

### **1.2.5 Previous Work**

#### **1.2.5.1 Performance evaluation of the monopile foundation using PISA methodology under extreme loading conditions in Malaysia.**

This research evaluates the performance of offshore monopile foundations for wind turbines at 30- and 60-meter water depths, particularly using the PISA (Pile-Soil Analysis) methodology, to address the challenges of complex pile-soil interactions under extreme loading in Malaysia's offshore conditions. The study employs Timoshenko beam theory for structural analysis, considering wind and wave forces at various water depths. It introduces both 1D and 3D finite element models to optimize monopile design for a 3.6 MW wind turbine, focusing on minimizing lateral displacement and rotation. A key contribution is identifying that rotational behaviour becomes independent of embedment depth beyond 49 m, allowing for optimized monopile dimensions of 8 m outer diameter, 0.08 m wall thickness, and 41-45 m embedment depth. These findings provide insights into efficient monopile designs capable of withstanding Malaysia's offshore environmental conditions (Ng et.al., 2024).

#### **1.2.5.2 Design and Fatigue Analysis of Monopile Foundation to Support the DTU 10 MW Offshore Wind Turbine**

This study investigates the feasibility and challenges of extending monopile foundations to support larger wind turbines, specifically the DTU 10 MW turbine, in deeper waters. It introduces preliminary monopile designs for water depths of 20m, 30m, 40m, and 50m, accounting for pile-soil interactions and hydrodynamic loads using advanced finite element modelling tools like Plaxis 3D. The study also develops a Fatigue Damage Parameter (FDP) to streamline fatigue damage predictions based on environmental conditions, enhancing accuracy and computational efficiency. Results show that hydrodynamic loads become more significant with increasing water depth, and using at least 30% of environmental conditions achieves 90% prediction accuracy (Velarde et al., 2017).

### **1.2.5.3 Renewable Wind Energy Resources in Offshore Low Wind Speeds Regions Near the Equator.**

This research focuses on improving wind turbine performance in offshore low-wind-speed regions, particularly near the equator. It examines strategies like blade design optimization, aerodynamics, and economic viability in low-wind areas, proposing innovations like Concentrator Augmented Wind Turbines (CAWTs) and morphing trailing-edge blades to reduce cut-in speeds and increase energy capture. The study's contributions include technological advancements that enhance power output and efficiency, reduce material costs, and optimize turbine placement. Results show significant improvements in low-speed torque, blade efficiency, and power generation, making wind energy projects more sustainable and economically viable in low-wind regions (Nizamani et. al., 2024).

## **1.3 Aims and Objectives**

The objectives of the thesis are shown as following:

- 1.3.1 To investigate the environmental load effects on the wind turbine at 60m water depth.
- 1.3.2 To design, analyse and assess the optimised monopile cross sections with 6 MW turbine.
- 1.3.3 To compare the lateral displacements vs horizontal loads for different designs of monopiles.

## 1.4 Research Methodology (Critical Appraisal)

### 1.4.1 p-y method

The p-y method is a critical analytical technique in geotechnical engineering, widely used to evaluate the lateral response of piles subjected to forces such as wind or waves. This method models the interaction between soil and pile through a series of nonlinear springs, represented by  $p$ - $y$  curves. These curves illustrate the relationship between the lateral soil resistance (denoted as  $p$ ) and pile deflection (denoted as  $y$ ) at various depths. The development of these  $p$ - $y$  curves is essential for capturing the complex soil-pile interaction, where soil resistance increases as the pile moves laterally.

The shape and behaviour of the  $p$ - $y$  curves vary depending on the type of soil, whether it is sand, clay, or rock. In sandy soils, the  $p$ - $y$  curves tend to show more rapid stiffening as the pile deflects. Conversely, in clay soils, the curve typically shows high initial stiffness at first, then gradually flattens out as the soil reaches its ultimate bearing capacity. These curves are often developed from empirical formulas based on extensive field tests, which provide the basis for analysing pile behaviour in different soil conditions.

In practice, the p-y method is applied to the design of pile foundations, particularly for structures like offshore platforms, wind turbines, and bridges that are exposed to significant lateral loads. By applying  $p$ - $y$  curves to model soil resistance along the pile, engineers can calculate critical parameters such as pile deflection, bending moments, and shear forces at different depths. This ensures the stability and efficiency of pile designs, which are crucial for the safety and performance of the structure.

However, the p-y method does have some limitations. It assumes a one-dimensional interaction between soil and pile, which might oversimplify the complex three-dimensional behaviour of soil around a pile. The accuracy of the method also depends heavily on the quality of the empirical data used to create the  $p$ - $y$  curves. Additionally, certain soil types, such as liquefiable soils, may require special adjustments to the standard p-y method.

### **1.4.2 Pile Soil Analysis (PISA) method**

The PISA method is an advanced approach developed to improve the design of offshore wind turbine foundations, specifically focusing on large-diameter monopile foundations. Traditional pile design methods, which were originally developed for smaller-diameter piles, often resulted in overly conservative designs for large monopiles. To address this, the PISA method introduces a more refined analysis by considering the specific characteristics of the pile-soil interaction for large-diameter piles, particularly in offshore conditions.

PISA uses a combination of numerical modelling and field testing to derive more accurate soil reaction curves (also known as p-y curves) for the specific site conditions where the monopile will be installed. These curves describe the lateral response of the soil as the pile moves, helping engineers to better predict the pile's behaviour under load. The method relies on large-scale testing and high-resolution numerical simulations that consider the non-linear behaviour of soils, including factors such as soil layering and stiffness.

A key aspect of the PISA method is that it tailors the design process to different soil types, recognizing that soils such as clays, sands, and silts respond differently to the large loads imposed by offshore wind structures. By incorporating field data and improved modelling techniques, PISA reduces the uncertainties inherent in pile design, leading to more efficient and cost-effective foundation solutions.

## **1.5 Scope of Work**

1.5.1 Finite Element Analysis.

1.5.2 Metocean Analysis.

1.5.3 Determination of Loads Acting on Structure.

1.5.4 Designing an Optimised Monopile Foundation for The Structure.

1.5.5 Determination of Lateral Displacement and Cross-section Rotation at mudline.

## **1.6 Limitations of Work**

1.6.1 Not focused on the fatigue life design.

1.6.2 Not considering the environmental impact on marine life.

1.6.3 Not including scouring.

1.6.4 Not analysing the construction methods and cost.

## **1.7 Outline of The Thesis**

In this thesis Chapter 1 includes the introduction of the topic, explains problem statements and the objectives for this final year project to be proceeded. Most of the required knowledge and literature reviews are stated in Chapter 2 for verification and exploration of better equipped information in this studied field. Chapter 3 then suggest a detailed methodology to achieve the main objectives. Subsequently, Chapter 4 applies the methodology to obtain results of the project, and the discussions are also done. Lastly, Chapter 5 concludes the whole project and provides recommendations to the optimised results.

## CHAPTER 2

### LITERATURE REVIEW

Table 2.0 Papers on Monopile Foundation Analysis and Design

Author	Journal Title	Objectives/Goals of Paper	Remarks
Bhattacharya, S., 2019.	<i>Design of foundations for offshore wind turbines.</i> John Wiley & Sons.	This book aims to bridge the knowledge gap between the foundation design methods traditionally used for offshore oil and gas structures and those required for OWTs. It addresses key issues such as dynamic sensitivity, different design criteria.	The book provide procedure for foundation design for OWTs, focusing on dynamic loading, soil-structure interaction, and cyclic loads. It highlights the types of foundation, emphasizing fatigue analysis, stability, and durability under environmental forces, with practical methods for cost-effective design.
Ng Chee Cong et al., 2024	Performance evaluation of the monopile foundation using PISA methodology under extreme loading conditions in Malaysia	The main objective was to use the PISA design framework to analyse and optimize the monopile foundation for supporting a 3.6 MW wind turbine at 30-meter and 60-meter ocean depth, taking into account the specific soil profile and loading	Wave load decreased as depth increase but overturning moment increased due to lever arm increment. The optimised monopile for 30 and 60 m both have an outer diameter of 8 m and wall thickness of 0.08 m.

		conditions of the site.	Their embedment depth however differs with 41 m and 45 m respectively.
Joey Velarde et al., 2017	Design and Fatigue Analysis of Monopile Foundation to Support the DTU 10 MW Offshore Wind Turbine	The study aims to design and analyse monopile foundations for varying water depths (20m, 30m, 40m, and 50m) and assess the impact of factors such as pile-soil interaction and hydrodynamic loads on the foundation's performance.	The study found that extending monopile foundations to support large wind turbines in deeper waters is feasible, with optimized designs managing increased hydrodynamic loads and accurately predicting fatigue damage using a streamlined method, enhancing reliability and cost-effectiveness.
Taşbaşı, A.D., 2024	Preliminary Geotechnical Design of Offshore Wind Turbine Monopiles in Türkiye Using FEM	To determine preliminary optimum monopile dimensions (diameter and embedded length) for offshore wind turbines at various sites in Türkiye by using Finite Element Method (FEM), specifically the PISA method via PLAXIS MoDeTo, under different generic soil profiles and	The study demonstrated that the PISA method implemented in PLAXIS MoDeTo is effective for preliminary monopile design across different Turkish offshore sites, identifying medium dense sand and medium stiff clay as



		loading conditions.	manageable soil profiles, while highlighting soft clay as the most challenging for monopile foundations.
Zafarullah Nizamani et al. 2024	Renewable wind energy resources in offshore low wind speeds regions near the equator.	This paper aims to improve wind turbine efficiency in regions with low wind speeds, concentrating on optimal turbine placement, blade design, aerodynamics, and economic feasibility, with a special focus on the levelized cost of energy in these low wind speed areas.	Turbines in low wind areas require a minimum wind velocity of 6.0 m/s for commercial power generation. Concentrator Augmented Wind Turbines (CAWTs) significantly enhance power output by optimizing turbine configurations and dimensions.

## 2.1 Types of Wind Turbines

There are several of design options for offshore wind turbines (OWTs) which are optimised respectively depending on environmental conditions, installation locations, wind speed and power output requirements

### 2.1.1 Horizontal Axis Wind Turbine (HAWT)

The most common type of OWT is the Horizontal Axis Wind Turbine (HAWT). It features blades that rotate around a horizontal axis which is parallel to the sea level. Key components include rotor blades (usually 2 or 3) that capture wind energy, a nacelle housing the generator and gearbox which sits on the tower, and a yaw system to adjust the turbine's direction. The blades spin as wind passes over them, creating lift and turning a shaft connected to a gearbox or generator, which then produces electricity. The tower height of HAWTs, typically ranging from 80 to 150 meters, helps them capture stronger winds (Hau, 2013). These turbines convert kinetic wind energy into electrical energy efficiently through aerodynamic design and control systems.

### 2.1.2 Vertical Axis Wind Turbine (VAWT)

The Vertical Axis Wind Turbine (VAWT) which is less common (e.g. Savonius WT) are used in areas with low wind speed or locations that experiences turbulent conditions. It has a vertical rotor shaft and a generator that is quieter and compact which makes them easier to install, and minimise visual impact. VAWTs are designed to allow wind capture from any direction without reorientation and has the ability to operate in turbulent winds. However, VAWTs are typically smaller and less efficient than HAWTs due to their aerodynamic limitations and lower lift generation. Offshore VAWTs, though still experimental, could be beneficial in deep waters where their simpler design allows for easier maintenance and reduces the need for complex yaw systems. For example, Darrieus Wind Turbine is a type of VAWT with curved blades like an egg beater. It is suited for low wind speed environments and can generate power in turbulent wind conditions.

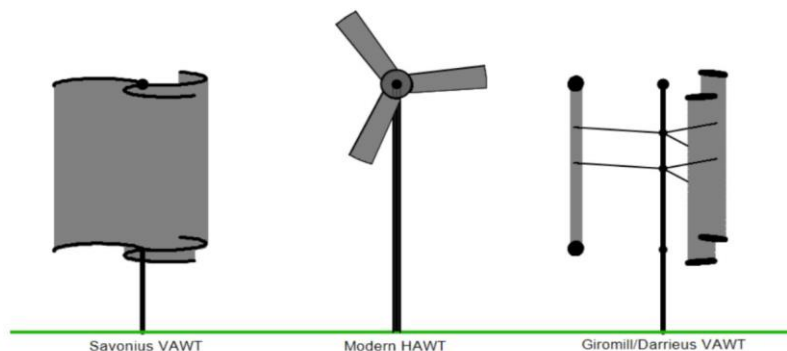


Figure 2.1.2: Types of Wind Turbines (Maurizio Collu, 2015).

### **2.1.3 Wind Turbines for Low Wind Region**

Nizamani et. al. (2024) stated that turbines in low wind regions need a minimum wind speed of 6.0 m/s to generate commercial power, emphasizing the critical need for low-speed start-up capabilities. Design challenges at low wind speeds require adjustments in rotor configurations and geometry, as well as the use of aerodynamic profiles tailored to produce high lift at low Reynolds numbers. Therefore, equipping a wind turbine with dual generators, each with different rated capacities optimized for low wind conditions, is a sensible approach. A larger rotor diameter enhances wind capture, leading to increased electricity generation. Even in areas with lower wind speeds, longer blades can harness more wind than shorter ones (Nizamani, 2024). This is supported by data from the Office of Energy and Renewable (2022), showing a 600% increase in rotor swept area since 1998, allowing for effective wind collection even in low wind regions.

Based on Nizamani et. al. (2024) research, Concentrator Augmented Wind Turbines (CAWTs) boost power output by refining turbine designs and dimensions. Morphing trailing-edge (MTE) blades and dimpled rotor blades enhance efficiency by improving aerodynamic performance, lowering cut-in speeds, and increasing torque. MTE blades, in particular, achieve a 40% reduction in cut-in speeds and a 600% increase in low-speed shaft torque. Slat-airfoil configurations help delay flow separation, leading to reduced material costs. Additionally, variable ratio gearboxes (VRG) optimize power generation by adjusting rotor speeds to match changing wind conditions.

## 2.2 Types of Foundations

There are three classifications of foundations which are gravity based, monopile and jacket foundations. The **gravity-based foundation** is usually situated on the seabed in depths of less than 10 meters. It is appropriate for sandy soil bed, compacted clay and rock. Their construction requires dredging of seabed. The structure consists of a large concrete or steel structure as it relies on the weight of the foundation for stability. Main characteristics include stability, durability and ability to withstand extreme weather conditions. Their large size and weight make them expensive to transport or install. **Gravity-based foundations** depend on the weight and friction between the foundation bottom and the seabed. By using its own weight, the structure resists forces of wind, waves and current. The stability can be improved by adding ballast or other materials to increase its weight.

**Jacket foundations** are installed in intermediate water depths of 5-50 meters. They are suitable for locations with stiff clays and medium-to-dense sands. Installations can be done by piles or suction caissons. Soft soil installations are feasible with longer pile lengths that can enhance friction resistance. These foundations have a steel frame that is fixed to the seabed with piles. The turbine tower is then attached to the top of the jacket. Main characteristics include suitability for deep water and good stability performance. However, the design of jackets requires a significant amount of steel and the cost of transporting and storage is high.

The **tripod foundation** is a subcategory of jacket type which is suitable for water depth of 10-35 meters. It is suitable for locations similar to the jacket type but is also suitable for even softer soils. They consist of three legs supporting a central column. They offer good stability in deep water and are suitable for soft soil conditions. Main characteristics include suitability for deep water, lightweight, relatively low cost and easy installation. However, their design required careful consideration of dynamic loading. Seabeds with more than 60 meter depths are currently being studied with floating systems. In short, the choice of foundation depends on the water depth, seabed conditions, site circumstances, turbine and loading characteristics as well as the economy. **Jacket and Tripod foundations** depend on the geometry, frame dimension, depth and diameter of the piles, suction

anchors and soil conditions. Their frames are to withstand the turbine and environmental loads. The piles and suction anchors provide sufficient bearing capacity and resistance to uplift while the large diameter helps resist bending and lateral forces.

The **spar-supported floating OWTs** uses catenary mooring and suction caisson anchors. It is required to calculate the upper limit of the ultimate load on the anchor. The ultimate load is achievable when the setup of the mooring line is fully stretched and not resting on the bottom, similar to a single taut mooring line. In this scenario, the load is transferred directly to the anchor without being influenced by soil friction along the horizontal portion of the mooring line. Moreover, the angle of the mooring line will be maximal which causes an inverse catenary shape at the anchor.

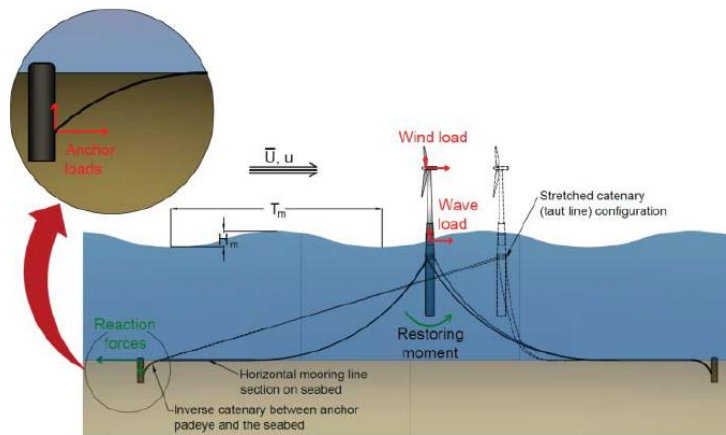


Figure 2.2.1 Spar-supported floating OWTs (Bhattacharya, 2019).

The **monopile foundation** is the most commonly used. It is usually situated in depths between 20-40 meters. Usage of impact hammer and vibratory driving is required during installation of monopiles at clayed and sandy seabeds. At rocky seabeds, bored piling and drilling are required. Monopiles are easy to manufacture, manage and install with relatively low cost. They consist of a single large steel pipe with diameters of 3-8 meters. Their main characteristics include cost-effectiveness, easy installation, and suitable for relatively shallow depths. Monopiles have a slenderness ratio of less or equal to 10, where slenderness ratio,  $SR = \text{embedment depth} / \text{diameter}$ . They usually have an outer diameter of 4-12 meters and a penetration depth of 20-40 meters. **Monopile foundations** depend on the pile depth, diameter, steel thickness and soil conditions. The pile must be deep enough to provide

sufficient bearing capacity and resistance to uplift. Their large diameter is to resist bending and lateral forces. Their thickness is to resist axial load from the turbine and environmental conditions. The soil conditions must be optimized to support the weight of the foundation and imposed loads.

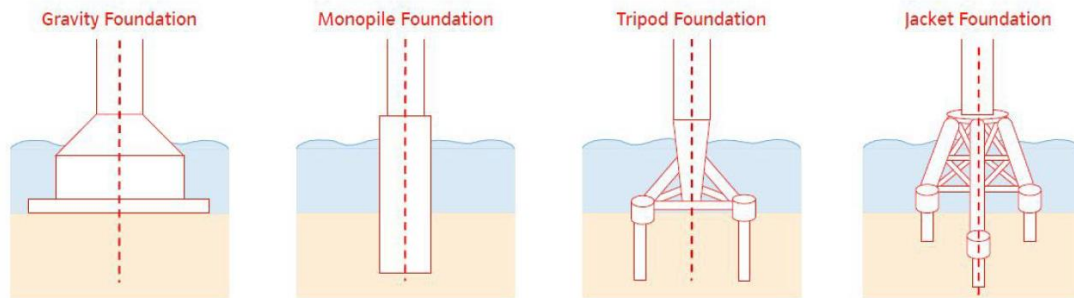


Figure 2.2.2 Types of Foundation (Wu et al., 2019).

### 2.3 Joints Connection or Monopile Foundations

In monopile foundations for offshore wind turbines, the integrity of connection joints both at the embedment depth and the tower interface are essential to the structural performance and long-term durability of the system. Historically, grouted connections were commonly used to join the transition piece (TP) to the monopile. However, experience from early offshore projects highlighted performance issues under cyclic loading, including settlement, cracking, and slippage, particularly in designs without shear keys (Bhattacharya, 2019). These issues have led to the adoption of improved solutions such as bolted flanges and conical connectors, which offer better resistance to fatigue and greater reliability over time.

At the embedment level, where the monopile interacts with the soil, the joint must be designed to transfer axial, lateral, and moment loads efficiently. This zone is governed by soil-structure interaction, typically modelled using  $p$ - $y$  curves and verified through geotechnical analysis. The connection must maintain structural capacity and stiffness while accounting for soil degradation under cyclic loading.

Design requirements for these joints are governed by three principal limit states. Under the Ultimate Limit State (ULS), the structure must remain stable during extreme events, such as 50-year return period storms. The Serviceability Limit State

(SLS) sets limits on rotation and displacement to ensure the turbine remains within operational tolerances which typically allowing less than 0.5 degrees of tilt at the mudline, with accumulated tilt not exceeding 0.25 degrees over the structure's life. The Fatigue Limit State (FLS) is especially critical, as the joints are subject to millions of load cycles caused by wind, wave, and operational forces. Fatigue assessments typically rely on S–N curves and focus on welded and bolted components, following standards such as DNV-RP-C203. When properly designed in accordance with industry guidelines, such as DNV-OS-J101 and IEC 61400-3, these connections can be expected to perform reliably over a design life of 20 to 25 years, with the possibility of extending to 30 years through routine inspection and maintenance.

## **2.4 Failure Modes of The Monopile Foundations**

Monopile foundations are susceptible to several types of failure, which can generally be grouped into geotechnical, structural, and environmental categories. One of the most critical geotechnical concerns is lateral load failure, where horizontal forces from wind, waves, or currents cause excessive displacement or rotation at the seabed. Design against this mode typically involves the use of lateral soil resistance models, such as p–y curves, in accordance with *Eurocode 7* (EN 1997-1:2004, Cl. 7.4.1). Although not explicitly defined in the code, it is common practice to limit pile head rotation to approximately 0.25° to 0.5°, and lateral displacement to 0.1 to 0.2 metres under service conditions.

Axial failure, either in compression or tension, occurs when vertical loads surpass the soil's capacity to resist them. The design methodology follows the recommendations in *EN 1997-1* (Cl. 7.6.2), applying partial resistance factors, typically 1.1 for compression and 1.3 for tension (EN 1997-1:2004, Table A.6). While compression resistance is derived from both shaft and base friction, tension relies solely on shaft friction. In cases of combined loading, where vertical, horizontal, and moment forces act simultaneously, designers must ensure that the interaction of these loads does not exceed the pile's overall capacity. This is addressed in *Eurocode 7* (Cl. 7.6.2.3), often using interaction formulas or numerical modelling to evaluate the combined effects.

Long-term cyclic loading from environmental forces can also result in degradation of soil strength and stiffness, leading to gradual rotation or displacement of the pile. Though *Eurocode 7* does not provide specific guidance on cyclic effects, standards such as *ISO 19901-4* and *DNV-RP-C212* recommend incorporating cyclic degradation models into the design. Industry practice generally limits long-term pile head rotation to less than  $0.5^\circ$  over the structure's lifespan. From a structural perspective, failure can result from material yielding, buckling, or fatigue. According to *Eurocode 3* (EN 1993-1-1:2005), structural elements must be designed so that the applied moment does not exceed the plastic resistance of the section. The fatigue life of the pile, especially at welds and transition zones, is assessed using SN-curves and damage accumulation methods as described in *EN 1993-1-9:2005*.

Scour and corrosion are important environmental factors that can reduce the effective embedded length and structural capacity of the pile. *Eurocode 7* (Cl. 2.4.6.2) requires scour to be considered in ultimate limit state checks, typically assuming worst-case scour depths of 1 to 2 pile diameters. For corrosion, *Eurocode 3: Piling* (EN 1993-5:2007, Cl. 4.3.2) advises incorporating a corrosion allowance, commonly ranging from 2 to 6 mm, depending on environmental exposure and design life.

Furthermore, monopile foundations are subject to several potential failure modes, including sliding, overturning, and bearing capacity failure. Each failure mode is influenced by environmental factors, construction quality, and soil interaction. Understanding these failure modes and their causes is essential for ensuring the structural integrity and longevity of monopile foundations, especially in harsh offshore environments where environmental and operational loads can be unpredictable.

Sliding failure in monopile foundations occurs when horizontal forces, such as those caused by waves or wind, overcome the frictional resistance between the foundation and the underlying soil. This type of failure is more likely when the shear stress acting on the foundation exceeds the soil's frictional capacity, leading to lateral movement of the foundation. Overloading, steep soil slopes, and improper anchorage of the foundation can all contribute to sliding failure. Visible signs of this failure mode include significant horizontal displacement of the foundation from its original position.



Overturning failure happens when the horizontal loads acting on the monopile, such as wind or current forces, create a moment that exceeds the soil's capacity to provide a resisting moment. When this imbalance occurs, the monopile can rotate or tilt, leading to instability. This failure mode is often exacerbated by soil degradation over time, extreme weather conditions, and construction errors. Offshore wind turbines, in particular, are vulnerable to overturning due to the large moments generated by wind and wave loads. Early signs of overturning failure include noticeable tilting or rotation of the foundation, often coupled with vertical displacement.

Bearing capacity failure is another significant failure mode, particularly concerning the vertical load-carrying capacity of monopile foundations. This occurs when the foundation's vertical bearing strength is insufficient to support the turbine's axial load, causing the monopile to settle excessively or sink unevenly into the seabed. Bearing failure can also result from changes in soil properties due to environmental factors like erosion, as well as improper design or maintenance. Indications of bearing failure include the development of vertical or diagonal cracks in the structure and differential settlement, leading to misalignment of the turbine.

## **2.5 Types of Loads**

### **2.5.1 Self-weight (Deadloads)**

**Dead loads** are the constant, permanent forces acting on the structure due to the weight of the components like the turbine, hub, tower and monopile. The specifications of a Siemens SWT-6.0-120 OWT has a rated power of 6 MW, cut-in wind speed of 3.0 m/s, rated wind speed of 12 m/s, and cut-out wind speed of 25.0 m/s has a tower-head weight of approximately 350 T, hub weight of 18 T and tower weight of 190 T (*Siemens SWT-6.0-120*, 2024).

### **2.5.2 Live Load**

Live loads refer to variable or transient forces acting on a foundation structure. They are influenced by factors such as the weight of maintenance personnel, equipment, and operational activities, all of which can fluctuate over time. For offshore wind turbines, operational activities like maintenance and repair tasks, the transport of personnel and equipment, and the installation or removal of components all contribute to live loads on the foundation. The weight of workers and tools during maintenance can add extra stress to the foundation, while the transportation of equipment and parts to and from the turbine introduces dynamic loads. The duration of these loads varies based on the specific tasks being undertaken, the number of personnel and involved equipment.

### 2.5.2.1 Cyclic Load by Rotor and Wind Blade

1P Load (Rotor frequency) is the load caused by vibration at hub level due to mass and aerodynamic imbalance of rotor. This load has a frequency equal to the rotational frequency of rotor. Since industrial wind turbines typically operate at variable speeds, 1P spans a band of frequencies associated with the lowest and highest rpm rather than a single frequency. Monopiles have a slenderness ratio of less or equal to 10, where  $S_R$  = embedment depth / diameter. These vibrations arise from the blade shadowing effects. When the blades of a wind turbine pass in front of its tower, they momentarily reduce the force on the tower due to a shadowing effect. For a three-bladed turbine, these vibrations occur at a frequency three times the turbine's rotational speed (3P). For a two-bladed turbine, these vibrations occur at a frequency two times the turbine's rotational speed (2P). The 2P/3P frequencies are obtained by multiplying the 1P frequency band limits by the number of blades. The magnitude of this load depends on the rotational speed of the turbine. If the natural frequency of the structure is more than five times the forcing frequency, the loading can be considered cyclic and inertia of the system may be ignored.

The interaction between the soil and the structure under cyclic loading is crucial for stability. OWT foundations typically experience millions of load cycles over their lifetime, leading to potential soil densification around monopiles, which could increase the foundation stiffness. These loads generate cyclic overturning moments at the foundation level, particularly at the mudline, where the monopile interacts with the soil. This must be carefully modelled and accounted for in the design.

### 2.5.3 Environmental Loads

Environmental loads are forces exerted on a structure by natural elements such as wind, waves, currents, and temperature changes. In offshore wind turbines, aerodynamic (wind) loads act on the turbine's blades and tower. Besides that, hydrodynamic loads such as wave, tidal or current forces impacts the foundation and overall structure. Additionally, temperature variations can cause expansion or contraction, contributing to thermal stresses. These environmental loads are hard to predict as they are dynamic and vary over time, making them critical factors in the design and stability of offshore structures.

#### 2.5.3.1 Aerodynamic (Wind) Loads

Wind loads are a major component which is calculated using the aerodynamic properties of the turbine and the characteristics of the wind at the site. It is produced by the wind thrust on the turbine blades and tower. The cyclic component of this load is influenced by the turbulence in the wind at the location, which is subject to variations over time and turbine operating conditions. According to Ng et. al. (2023) evaluation on this matter, different models such as the Extreme Operating Gust Model, were used to evaluate the impact of wind on the monopile foundation.

Wind turbulence can be estimated as a fluctuating wind speed component,  $u$ , superimposed on the mean wind speed,  $\bar{U}$ . Hence, the total wind speed can be written as  $U = \bar{U} + u$ . The turbulence intensity,  $I$ , is used to describe the degree of turbulence and is given by the equation:

$$I = \sigma_u / \bar{U}$$

where  $\sigma_u$  is the standard deviation of wind speed around the mean  $\bar{U}$ . The turbulence intensity varies with mean speed, site location, surface roughness, and is also modified by the turbine itself. Taylor (1938) assumed that the characteristics of **eddies** can be considered constant (frozen) in time and this statement is acceptable for wind turbine designs. The turbulence is usually analysed in the frequency domain by a Power Spectral Density (PSD) function that explains how various frequencies contribute to the overall variance of wind speed. The size of eddies is correlated with the frequency of turbulence. Greater eddy size results in low-frequency variations in

wind speed, whereas smaller vortices cause short high-frequency wind speed variations. Large turbulent eddies with a high energy content usually have length scales of several km. As turbulent energy dissipates to heat, the huge eddies tend to decay to smaller and smaller eddies with higher frequencies.

Kaimal spectrum is a power spectrum of turbulence and it is commonly used for modelling the atmospheric boundary layer and can be connected to foundation designs. The energy in this spectrum is contained in a little wider frequency range and is significantly less peaked. The surrounding landscape can alter the Kaimal's spectrum as the intensity of turbulence increases with surface inhomogeneity. The stratification is also an important consideration whether or not it is stable, unstable or neutral. Near-neutral conditions are regular for medium and high wind speeds and are necessary for fatigue damage calculation. The equation below represents the theoretical Kaimal spectrum for a fixed reference point in space for a neutral stratification atmosphere  $S_{uu}(f)$  as suggested by Det Norske Veritas (DNV):

$$S_{uu}(f) = \frac{\sigma_u^2 \left( \frac{4L_k}{U} \right)}{\left( 1 + \frac{6fL_k}{U} \right)^{\frac{5}{3}}}$$

As the DNV code suggest;  $L_k = 5.67z$  for  $z < 60\text{m}$ ;  $L_k = 340.2\text{m}$  for  $z \geq 60\text{m}$ , where  $z$  is the height above sea level.  $f$  is the frequency,  $\bar{U}$  is the mean wind speed (from site measurements), and  $\sigma_U$  is the standard deviation of wind speed. Although the Kaimal spectrum can be computed at any low frequency, its use is restricted to high-frequency fluctuations.

The turbulence aspect of the wind flow is taken into account in the quasi-calculation method. In this case, the wind speed ( $\bar{U}$ ) is divided into two parts: the sum of the average wind speed and the turbulent wind speed component ( $U + u$ ). This total wind speed is defined individually for each wind speed component.

$$\bar{U} = U + u$$

Generally aerodynamic loads that include the estimation of the wind thrust force ( $F_{th}$ ), overturning moment can be calculated with their respective equations:

$$F_{th} = C_{th} \frac{1}{2} \rho_a A_R (U + u)^2$$

$$M_{wind} = F_{th} (S + Z_{hub})$$

which are discussed in Chapter 3 with more details.

### 2.5.3.2 Hydrodynamic loads

This load occurs when waves bombard the substructure of the OWT, particularly the parts of the structure exposed to wave and current action. **Wave loads** magnitudes can be calculated using higher-order hydrodynamic theories such as the Stokes waves or Dean's stream function theory for more precise estimates. In this study, the linear theory is applied for simpler load calculation using the Morison equation:

$$F_{wave}(t) = \int_0^{d_w} (f_D + f_I) dz_w$$

which is explained in better details in Chapter 3, considering sea state factors like different wave heights, periods, direction and current velocity. The most critical wave scenario identified involves combinations of 1-year and 50-year extreme wave height and other operational conditions.

### 2.5.3.3 Current loads

Ocean currents which affect OWT's foundations, can be modelled when calculating the forces exerted on the substructure. Ocean currents are mainly caused by wind and tidal effects, which vary with depth. **Wind-induced currents** dominate near the surface of the water, where the wind pushes the water particles, while **tidal currents** and become more influential deeper in the water. The speed of the current usually decreases with depth, reaching zero at the seabed. However, because there is significant uncertainty in predicting actual current speeds at different depths, a conservative modelling approach is often used, with the assumption of a **constant current velocity** along the entire depth of the water. The **constant current velocity** is assumed to be the maximum expected over a 50-year period. A commonly used rule is to set the current speed at 1% of the extreme mean wind speed expected over 50 years (Bhattacharya, 2019). Once the constant velocity profile is set, the **drag force** acting on the substructure from the current can be estimated similarly to how drag loads due to wind are calculated. This provides a safe estimate of the forces on the foundation, ensuring it can withstand extreme conditions.

## 2.6 Type of Soil Properties

The soil properties of the ocean floor at deep depths are critical in determining the design and stability of OWT foundations. **Sandy soils** are common at these depths and offer good drainage, making them ideal for supporting structures like monopile or jacket foundations. Sands may vary from fine to coarse but are often compacted over time, providing higher bearing capacity. In contrast, **silt and clay soils** are typically found in low-energy environments and can exhibit low permeability and significant consolidation. This can lead to settlement over time, which must be accounted for in foundation design to ensure long-term stability. In areas with stronger currents, **gravel and cobbles** may be present, offering higher strength but posing challenges during pile installation (Byrne & Houlsby, 2003).

The **shear strength** of seabed soils is a key factor for assessing the load-bearing capacity of offshore wind turbine foundations. Sandy soils typically provide higher shear strength, which allows for efficient load transfer from the turbine to the seabed. In soft clays, undrained shear strength plays a crucial role, as these soils can exhibit low shear strength, requiring more complex foundation designs like piled foundations to distribute loads effectively (Houlsby et al., 2005). The overall bearing capacity of the seabed must be evaluated carefully, particularly in areas where soft clays or silts may be present, as these soils can lead to long-term settlement under the constant loading from the turbine.

**Permeability and drainage** characteristics of ocean floor soils also influence the design of wind turbine foundations. Sands are highly permeable, allowing rapid dissipation of pore water pressure and minimizing the risk of excess settlement. However, silts and clays have low permeability, which can result in slow consolidation and potentially significant settlement over time. The build-up of pore water pressure in these soils during loading from turbine operation or installation can reduce their strength and stability, making drainage considerations essential for foundation design.

**Soil consolidation and settlement** are particularly important in OWT projects, as the continuous loading from turbines can cause gradual settlement, especially in fine-grained soils like silts and clays. These soils often consolidate slowly under load, potentially leading to long-term foundation movement (LeBlanc et al., 2010). In contrast, sands tend to consolidate more quickly with less risk of significant settlement. Additionally, offshore wind turbines are subjected to cyclic loading from wind, waves, and currents, which can lead to soil fatigue and gradual weakening, especially in sandy soils (Byrne & Houlsby, 2003).

Various geotechnical hazards must be considered when designing foundations for offshore wind turbines. **Liquefaction** is a major concern in saturated sandy soils, particularly in seismic regions or under strong wave action. This phenomenon, where the soil temporarily loses strength and behaves like a fluid, can undermine the stability of monopile or jacket foundations (Whitehouse et al., 2011). Additionally, **scour** is a significant issue in sandy and silty soils. It occurs when water currents erode material around the base of the turbine foundation, potentially compromising its



stability. Mitigation measures, such as scour protection, are often necessary to prevent foundation failure.

In some offshore regions, seabed sediments may contain carbonate-rich materials, particularly in tropical and subtropical areas. These calcareous sediments, made up of coral and shell fragments, may be cemented, increasing their strength but also making them brittle. This can complicate the installation of pile foundations, as cemented soils resist penetration and may fracture under loading. Moreover, high pore water pressure in these sediments, especially under dynamic loads from turbines, can further reduce their stability (Randolph et al., 1994).

At greater ocean depths, the seabed often exhibits layered soil profiles, where different types of soils are stacked. For instance, loose sands may be found in the upper layers, while deeper layers may consist of stiff clays or compacted sediments. These variations require detailed geotechnical investigations to determine the most appropriate foundation design for each specific location (LeBlanc et al., 2010).

## **2.7 Plaxis Monopile Designer**

The Plaxis Monopile Designer is an offshore foundation design software tool developed by Bentley Systems that integrates with PLAXIS 3D, a Geotechnical Design Software. It is a finite element (FE) software designed for analysing monopile foundations and practices the Pile Soil Analysis (PISA) method. The software is able to generate and evaluate 3D FE models and able to derive, normalize, and parameterize soil reaction curves to calibrate 1D beam models (Ng et.al., 2024). The software optimizes monopile foundation design to reduce overall steel fabrication, transportation and installation cost.

### 2.7.1 Rule-based Design (RBD) and Numerical-based Design (NBD)

In the Rule-Based Design (RBD) approach, the soil parameters used for analysis come from standard soil investigation data, with calibration data for the 1D finite element (FE) model often imported from previously calibrated numerical models from other projects or published studies. The accuracy of predicting the monopile's response depends on factors such as variations in soil profiles, differences in loading conditions, and how closely the monopile geometries in the current study match the original calibration cases. Due to these dependencies, the RBD method is most suitable for **preliminary conceptual design**, providing a broad overview before more detailed analysis.

However, in the Numerical-Based Design (NBD) approach, 3D finite-element (FE) models specific to the site are used for a more thorough and precise analysis. This involves performing 3D FE calculations using high-quality soil profile data from laboratory tests, field investigations, and an initial selection of monopile geometries. These models are used to calibrate the soil constitutive models in Plaxis 3D. This method is ideal for **detailed design** as each 3D FE model corresponds to a specific scenario within the target design study. Once calibrated, the results from these 3D models are parametrized and applied to a faster 1D FE analysis. This method **will be used for this project**,

### 2.7.2 Finite Element Model

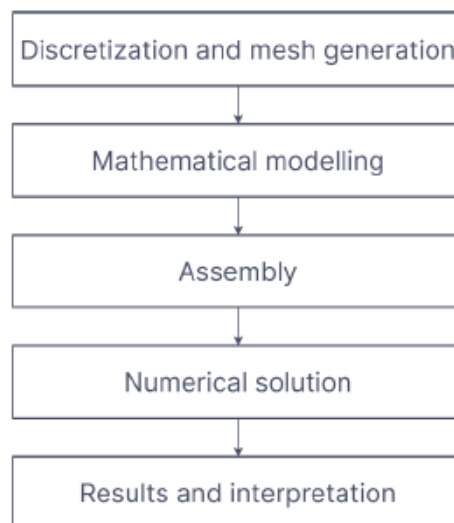


Figure 2.6.2.1: General FE Analysis and Modelling Procedure.

Finite element modelling (FEM) involves breaking down a structure or system into a finite number of smaller elements, each with distinct properties and behaviours. These elements are connected at specific points known as nodes. The structural responses are calculated by solving a series of equations that represent the physical behaviour of the elements and their interactions.

FEM begins with discretization, where a structure or object is divided into smaller, discrete elements. These elements are typically geometric shapes like tetrahedra, depending on whether the analysis is conducted in two or three dimensions (Cifuentes and Kalbag, 1992). Each element is connected at specific points known as nodes, creating a mesh that approximates the continuous system. The mesh is refined in critical areas, such as the monopile base or regions with high-stress concentrations. Once discretization is complete, mathematical equations are established at each node of the elements, based on the physical laws governing the system's behaviour. FEM utilizes mathematical models to represent the system's behaviour within each element, whether it involves stress and strain in structural mechanics or other phenomena.

The equations from the individual elements are then integrated into a global system that accounts for element interactions and adheres to the system's boundary conditions. This global system is usually represented by a sparse matrix, which contains numerous zeros due to the localized approach of the finite element method (Thompson, 2006). Solving this system of equations is a crucial part of FEM. Various numerical techniques, such as matrix inversion, iterative methods, and direct solvers, are employed to determine the system's key values, including displacements, temperatures, pressures, or other physical quantities relevant to the analysis. After obtaining the numerical solution, the results are visualized and interpreted through contour plots, stress maps, temperature profiles, or other relevant visual data that help to understand the behaviour of the system. These visual outputs are essential for making informed decisions and optimizing the design.

In a one-dimensional (1D) finite element analysis as shown in Figure 2.4.1.2, the structure or system is modelled as a one-dimensional object, meaning that the analysis focuses on deformation or flow in a single direction, typically along one axis (Koutromanos, 2018). This approach assumes that the behaviour in other dimensions

is consistent and does not significantly affect the analysis. This simplification allows for quicker computations and is useful when the effects in other dimensions are minimal or can be reasonably estimated. Conversely, 3D finite element modelling involves constructing a three-dimensional representation of the structure or system, considering deformation or flow in all three dimensions. This approach captures the full complexity of the geometry and behaviour, offering a more accurate depiction of the real-world system but requires more computational power and time to complete the analysis.

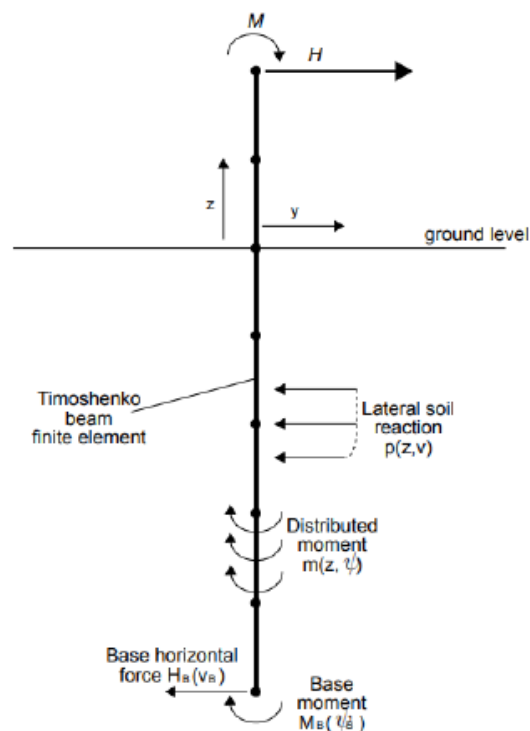


Figure 2.6.2.2: 1D FEM Illustration (Plaxis, 2018).

### 2.7.3 Timoshenko Beam Theory

The Timoshenko beam theory is an advanced framework for analysing beam behaviour, particularly useful when addressing the limitations of classical beam theories, such as Euler-Bernoulli beam theory. One of the primary distinctions of Timoshenko beam theory is its incorporation of shear deformation. While the Euler-Bernoulli theory assumes that plane sections of the beam remain perpendicular to the neutral axis during bending, Timoshenko's approach recognizes that this assumption does not hold in all cases, particularly for short and deep beams. By accounting for shear deformation, the Timoshenko theory provides a more accurate representation of how beams deform under various loading conditions. Another critical aspect of the Timoshenko beam theory is its consideration of rotational effects. The theory assumes that the rotation of a beam's cross-section results not only from bending but also from shear deformation.

Monopiles are cylindrical foundations widely used for offshore wind turbines and other structures, driven deep into the seabed to provide stability against various loads. Given their slender design and interaction with soil, the analysis of monopiles benefits significantly from Timoshenko beam theory, which accounts for both shear deformation and rotational effects

The Timoshenko beam theory is used in structural engineering to model beams, considering both bending and shear deformations. It captures how the monopile reacts to shear strain, which is the distortion caused when layers of material move parallel to each other. As monopiles become shorter relative to their diameter (length-to-diameter ratio decreases), the effect of shear strain on the monopile's behaviour becomes more important (Gupta and Basu, 2020). The 1D Finite Element (FE) model is a simplified model used to design monopiles as shown in Figure 3.4.3. The 1D model uses data from the parametrized soil reaction curves of the 3D FE models and existing soil reaction data. The 1D model helps calculate the optimal monopile foundation through a series of quick design calculations, making the process more efficient.

The monopile is subjected to a combination of horizontal force ( $H$ ) and moment ( $M$ ) applied at a certain height above the mudline. The monopile also experiences soil resistance from the embedded part. This key forces and moments in

the 1D model can be broken down into four main components. Firstly, the base horizontal force ( $H_B$ ) is the force exerted by the soil on the base of the monopile. Second is the distributed lateral load ( $P$ ) which is the force applied along the shaft of the monopile, similar to what is used in the standard p-y method.

Thirdly, is the distributed moment ( $M$ ) along the monopile shaft, caused by vertical shear tractions, forces acting parallel on the surface between the soil and the monopile due to the pile's rotation. These tractions are especially significant near the surface of the soil on the passive side of the monopile, where a wedge-type failure mechanism can occur when the pile is loaded to its maximum capacity (Burd et al., 2017). This means as the pile is pushed to its limits, the soil on the side opposite the load begins to fail in a wedge-like shape. The fourth resistance is the base moment ( $M_B$ ) which is applied at the base of the monopile. The relation between the length-to-diameter ratio of the monopile decreasing and the shear tractions play a significant role at the base of the monopile, where the base shear force ( $H_B$ ) and base moment ( $M_B$ ) is taken into consideration for the monopile's responds to loads Burd et al. (2017).

## **2.8 Limit States**

### **2.8.1 Ultimate Limit State (ULS)**

The **ULS** refers to the maximum load-bearing capacity of a foundation before failure or collapse occurs. In the context of offshore wind turbine foundations, ULS involves determining the maximum loads the foundation will face under various design load conditions, such as wind, wave, and operational forces. These loads are then compared with the structural capacity of the foundation to ensure that it can withstand the most extreme scenarios without failing. For monopile foundations, assessing ULS is crucial for ensuring structural integrity and stability, as it involves calculating the foundation's ability to resist these maximum applied loads throughout its operational life. The ULS must satisfy several criteria according to Bhattacharya (2019). Firstly, is that the axial pile capacity for geotechnical, if pile-head displacement is more than 10% of pile diameter, ultimate capacity is reached. The axial pile capacity for structural was mentioned that buckling can occur to laterally insufficient support piles

especially on the vulnerable long, slender thin-walled piles. As for the structural capacity of section will concern the maximum moment a pile section can withstand before pile material yields where pile geometry and material is a factor. Lastly, the moment-carrying capacity for geotechnical concerns where the soil surrounding the pile fails. Guidelines to achieve the ULS follows the DNVGL-ST-0126: "Support Structures for Wind Turbines" and DNVGL-ST-0437: "Loads and Site Conditions for Wind Turbines".

### **2.8.2 Serviceability Limit State (SLS)**

In offshore monopile foundation design, SLS refers to the condition where the foundation remains functional and meets performance requirements under typical operational and environmental loads. The SLS criteria aim to prevent excessive rotation that could impair the wind turbine's performance. Standards and guidelines, such as those from DNV and API, set SLS requirements for monopile foundations, taking into account operational loads, environmental factors, and the desired performance of the wind turbine system.

The allowable vertical and horizontal displacements for an offshore wind turbine monopile depend on serviceability limit states (SLS) criteria, primarily to ensure safe operation. These limits focus on deflections, rotations, and settlement that can affect the turbine's functionality. According to Bhattacharya (2019), vertical displacements and rotational limits should be kept under 0.5 degrees at the pile head or mudline to avoid excessive rotation or deflection that could impact non-structural components such as the generator and gearbox.

Lateral displacements are generally controlled to maintain structural stability and operational efficiency. According to the DNV guidelines, lateral displacement for monopile foundations under serviceability limit states (SLS) typically remains within 0.1 meters at the pile head, but it can vary based on soil conditions, design, and environmental load factors. This limit helps ensure the turbine remains operational without excessive deformation. These limits are set based on operational tolerances, turbine manufacturer requirements, and serviceability codes such as those from Det Norske Veritas (DNV) and IEC standards.

### **2.8.3 Fatigue Limit State (FLS)**

The FLS in offshore wind turbine foundation design focuses on ensuring the foundation's durability against cyclic loads and stresses over the turbine's operational life. The foundation must be capable of withstanding repeated loads without suffering from fatigue damage or failure. To meet FLS standards, design criteria such as fatigue life, stress range, and stress amplitude are carefully defined to maintain structural integrity and functionality. Addressing the FLS is vital for ensuring the long-term reliability and safety of the foundation, minimizing the risk of fatigue-induced failures throughout its service life. The FLS must define fatigue life, stress range, and stress amplitude following the DNV-RP-C203: "Fatigue design of offshore steel structures."



## **CHAPTER 3**

### **METHODOLOGY**

This chapter presents a structured approach that includes data collection and pre-processing, calculating extreme environmental loads, analysing load combinations, and evaluating structural responses using finite element methods. The wind load is determined by the structure's aerodynamic characteristics and the wind's speed, while the wave load is influenced by the wave height, wave period, depth and hydrodynamic properties. Additionally, the chapter explains the analysis techniques and design methods using Bentley Plaxis Monopile Designer and Plaxis 3D.

The following procedures are the steps to achieving the main objectives of this project.

- 3.1 Obtaining Site and Offshore Wind Turbine (OWT) Data
- 3.2 Aerodynamic Loads Estimation
- 3.3 Hydrodynamic Loads Estimation
- 3.4 Initial Geometry Estimation
- 3.5 Design Technique
  - 3.5.1 Soil Mode
  - 3.5.2 Calibration Mode
  - 3.5.3 Analysis Mode
  - 3.5.4 Results Mode



Table. 3.1.1: Offshore Soil Profile of Kuala Terengganu (Nadzari, 2007).

Soil Depth (m)	Description	$\gamma'$ (kN/m <sup>3</sup> )	$G_0$ (kN/m <sup>2</sup> )	$S_{u,top}$ (kN/m <sup>2</sup> )	$S_{u,bottom}$ (kN/m <sup>2</sup> )	$K_0$
0	Mudline					
-1.4	Very Soft to Soft Clay	7	3345	6	15	0.8
-19.5	Firm Clay	7	2.88E+04	25	40	0.8
-21.4	Stiff Clay	8	1.42E+05	80	80	0.8
-34.4	Firm to Stiff Clay	8	9.37E+04	45	70	0.8
-36.7	Stiff to Very Stiff Clay	6.5	1.93E+05	70	125	0.8
-40.5	Stiff to Very Stiff Clay	6.5	1.93E+05	125	70	0.8
-43	Very Stiff Clay	6.5	2.20E+05	150	150	0.8
-60	Stiff Clay	8	1.68E+05	85	100	0.8
-74	Very Stiff Silt	8	8.80E+04	88	128	0.8

Where:

$\gamma'$  = Submerged unit weight, (kN/m<sup>3</sup>)

$G_0$  = Small strain shear stiffness modulus in the middle of the soil layer, (kN/m<sup>2</sup>)

$S_{u,top}$  = Undrained shear strength at the top of the soil layer, (kN/m<sup>2</sup>)

$S_{u,bottom}$  = Undrained shear strength at the bottom of the soil layer, (kN/m<sup>2</sup>)

$K_0$  = Lateral earth pressure coefficient at rest.

### 3.1.2 Offshore Wind Speed in Kuala Terengganu

The wind in Peninsular Malaysia predominantly originates from the northeast and southwest directions, as illustrated in Figure 3.1.2.1, with its strength primarily influenced by the monsoon seasons. According to Wong Tian Heng (2022), the highest wind speed (V) recorded between 2010 and 2022 was observed in the offshore area of Terengganu (Abu Kecil) at various elevations. The wind data for Abu Kecil is presented in Table 3.1.2.

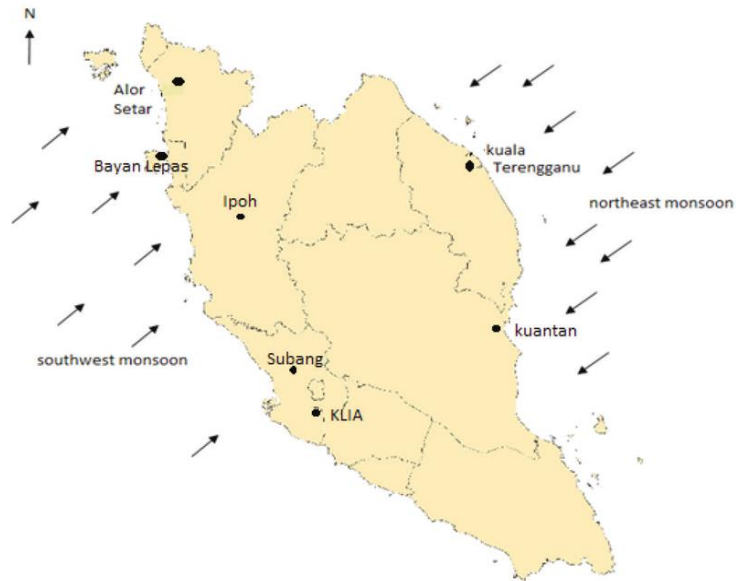


Figure 3.1.2.1: Recorded Wind Direction in Peninsular Malaysia (Satari et al., 2015).

Table 3.1.2: Recorded Wind Speed in Abu Kecil (Wong Tian Heng, 2022).

<b>Region: Abu Kecil</b> <b>Longitude: 105.337438 E, Latitude: 6.13418 N</b>					
Mean wind speed at 10 m (m/s)	Rated mean wind speed at 10 m (m/s)	Mean wind speed at 50 m (m/s)	Rated mean wind speed at 50 m (m/s)	Mean wind speed at 90 m (m/s)	Rated mean wind speed at 90 m (m/s)
4.9623	8.684065	6.24505	10.9288	6.79209	11.8862

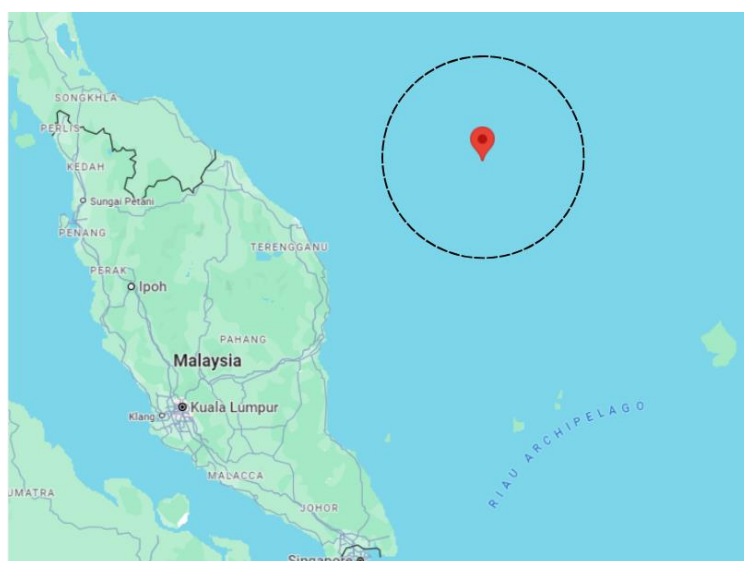


Figure 3.1.2.2: Centre Location of Abu Kecil (105.337438 E, 6.13418 N) based on Google Maps.

The distance from the targeted offshore region (Abu Kecil) to the closest onshore location (Pantai Batu Burok, Kuala Terengganu) measures 257.60 km, as illustrated in Figure 3.1.2.3.

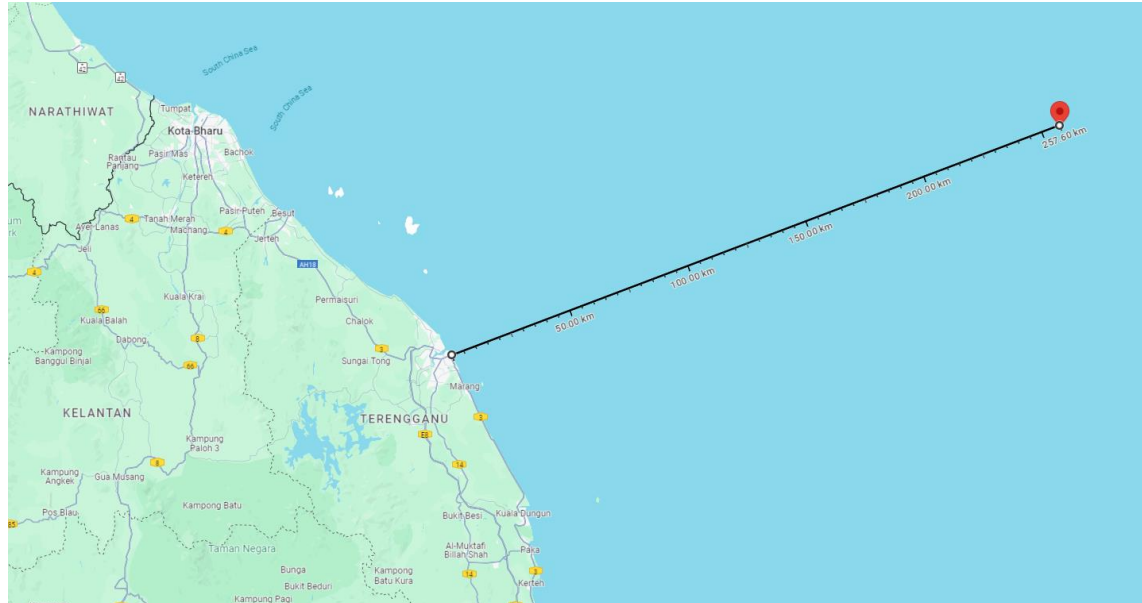


Figure 3.1.2.3: Distance from the centre of Abu Kecil to The Nearest Onshore Area (Pantai Batu Burok, Kuala Terengganu) based on Google Maps.

### 3.1.3 Offshore Wave Properties in Kuala Terengganu

The following wave data summarised it in Table 3.1.3.1 was retrieved from Petronas (2009). The direction follows a true magnetic north.

Table 3.1.3.1: Wave Data of Abu Kecil.

<b>Region: Abu Kecil</b>				
<b>Longitude: 105.306 E, Latitude: 6.1199 N</b>				
<b>Wave Parameters</b>	<b>1-year return period</b>	<b>10-year return period</b>	<b>50-year return period</b>	<b>100-year return period</b>
Significant wave height, $H_s$ (m)	4.2	4.9	5.2	5.3
Significant wave Period, $T_s$ (s)	6.6	7.0	7.2	7.2

### 3.1.4 Offshore Wind Turbine Specifications (Self-weight)

A 6.0 MW wind turbine is evaluated in the analysis and the design followed is known as Siemens SWT-6.0-120, and its specifications are presented in Table 3.1.3.2.

Table 3.1.3.2: OWT Specification and Weight.

<b>Manufacturer: Siemens</b>		
<b>Power Specification</b>	<b>Rotor Specification</b>	<b>Weight</b>
Rated power: 6.0 MW	Diameter: 120 m	Hub: 18 T
Cut-in wind speed: 3.0 m/s	Swept area: 11,500.0 m <sup>2</sup>	Tower max: 190 T
Rated-wind speed: 12.0 m/s	Blades number: 3	Tower-head weight: 350 T
Cut-out wind speed: 25.0 m/s	Max rotor speed: 11.0 U/min	
	Type: B58	

### 3.2 Aerodynamic Loading Analysis

Occurring loads on the structure due to wind forces are aerodynamic loads. The aerodynamic loading analysis required the evaluation of several conditions. Firstly, the conditions at normal turbulence scenario need to be estimated. Secondly is the condition at extreme turbulent scenario, and the final condition is the extreme operating gust (EOG) model at cut-out and rated wind speeds. The ultimate result is to achieve the maximum thrust force and overturning moment caused by aerodynamic loads, with the aid of numerous sub equations to consider.

At a **normal turbulence scenario**, a normal turbulence model (NTM) is used for evaluation of aerodynamic loads. The NTM calculation of the **maximum thrust force** ( $F_{wind,NTM}$ ) acting on the wind turbine uses the equation from Bhattacharya (2019):

$$F_{wind,NTM} = 0.5\rho_a A_R C_{th}(U_R + U_{NTM})^2 \quad (3.2.1)$$

where  $\rho_a$  is the density of air ( $\text{kg/m}^3$ );  $A_R$  is the rotor swept area ( $\text{m}^2$ );  $C_{th}$  is the thrust coefficient, which depends on the mean wind speed at hub (Bhattacharya, 2019).  $U_R$  is the rated wind speed ( $\text{m/s}$ ) and  $U_{NTM}$  is the **maximum turbulent intensity component** ( $\text{m/s}$ ).

Theoretically, it is assumed that the pitch control's time constant is synchronized with the rotor's rotation period, allowing the pitch control to effectively respond to wind speed changes that occur at frequencies lower than the turbine's rotational speed. To determine  $U_{NTM}$  the contribution of wind speed variations at frequencies higher than the rotor's maximum frequency must be calculated in relation to the overall standard deviation of the wind speed (Bhattacharya, 2019). The determination of  $U_{NTM}$  firstly requires the calculation of the standard deviation of normal turbulence ( $\sigma_{U,NTM}$ ) with the equation obtained from IEC (2005):

$$\sigma_{U,NTM} = I_{ref}(0.75U + b) \quad (3.2.2)$$

where  $I_{ref}$  is the reference turbulent intensity,  $U$  is the mean wind speed at 90 m above sea level (m/s) and  $b$  has a value of 5.6 m/s (Bhattacharya, 2019). This  $\sigma_{U,NTM}$  will then be incorporated into a formula based on a Kaimal spectrum model to obtain an overall standard deviation,  $\sigma_{U,NTM,f>f_{1p}}$  :

$$\sigma_{U,NTM,f>f_{1p}} = \sigma_{U,NTM} \sqrt{\frac{1}{\left(\frac{6Lk}{U_R} f_{1P,max} + 1\right)^{\frac{2}{3}}}} \quad (3.2.3)$$

Where  $f_{1P,max} = 0.2$  for a 6.0 MW wind turbine is the maximum rotor frequency (Hz). The **turbulence integral length scale ( $Lk$ )** is used to model the spatial distribution of turbulence in the wind flow. It provides a rough estimate of the average size of turbulent eddies and wind fluctuations that impacts the offshore structure as loads. The incorporation of this parameter into wind loads models ensures a safer and more accurate design for the structure in resisting turbulent effects and wind-induced forces.  $Lk$  can be calculated with the equation:

$$Lk = 300 \left(\frac{z}{300}\right)^{0.46+0.074 \ln(z_0)} \quad (3.2.4)$$

Where  $z_0$  is the terrain roughness of open sea with wave with a value of 0.01, and  $z$  is the height above sea level in meters. From Bhattacharya, (P-74), the equation provided to calculate the  $U_{NTM}$  is given as:

$$U_{NTM} = 1.28 \sigma_{U,NTM,f>f_{1p}} \quad (3.2.5)$$

The thrust coefficient ( $C_{th}$ ) between the cut-in wind speed and the rated wind speed is calculated is determined according Bhattacharya (2019), following the method outlined by Frohboese et al. (2010), with the equation:

$$C_{th} \frac{3.5 \frac{m}{s} (2U_R + 3.5 \frac{m}{s})}{U_R^2} \approx \frac{7 \frac{m}{s}}{U_R} \quad (3.2.6)$$



These value can then be applied to Eq (3.2.1) to generate the maximum thrust force ( $F_{wind,NTM}$ ) acting on the wind turbine under a NTM. Subsequently, the overturning moment caused by the thrust force on the wind turbine in a NTM can be obtained with the equation:

$$M_{wind,NTM} = F_{wind,NTM}(S + Z_{hub}) \quad (3.2.7)$$

where  $S$  is the water depth and  $z_{hub}$  is the tower hub height, both in meters. The environmental load factor of  $\gamma_L = 1.25$  must be incorporated to both the loadings as well.

When an **extreme turbulence scenario** is met, an extreme turbulence model (ETM) is used for evaluation of aerodynamic loads. Similarly, the ETM calculation of the **maximum thrust force** ( $F_{wind,ETM}$ ) acting on the wind turbine uses the equation from Bhattacharya (2019):

$$F_{wind,ETM} = 0.5\rho_a A_R C_{th}(U_R + U_{ETM})^2 \quad (3.2.8)$$

The parameters remain the same with the NTM model except for  $U_{ETM}$  which is the maximum turbulent intensity component (m/s) that differs. As for the ETM, the determination of  $U_{ETM}$  also requires the calculation of the standard deviation of normal turbulence ( $\sigma_{U,ETM}$ ) with the equation obtained from IEC (2005):

$$\sigma_{U,ETM} = cI_{ref} \left[ 0.072 \left( \frac{U}{c} + 3 \right) \left( \frac{U_R}{c} - 4 \right) + 10 \right] \quad (3.2.9)$$

where  $c = 2$  m/s according to Bhattacharya (2019),  $I_{ref}$  is the reference turbulent intensity,  $U$  is the mean wind speed at 90 m above sea level (m/s) and  $U_R$  is the rated wind speed. This  $\sigma_{U,ETM}$  will then similarly be incorporated into a formula based on a Kaimal spectrum model to obtain an overall standard deviation,  $\sigma_{U,ETM,f>f_{1p}}$  :

$$\sigma_{U,NTM,f>f_{1p}} = \sigma_{U,NTM} \sqrt{\frac{1}{(\frac{6Lk}{U_R} f_{1p,max} + 1)^{\frac{2}{3}}}} \quad (3.2.10)$$

where  $f_{1P,max} = 0.2$  for a 6.0 MW wind turbine is the maximum rotor frequency (Hz) and the turbulence integral length scale ( $Lk$ ). The equation provided from Bhattacharya, (P-74) to calculate the  $U_{ETM}$  is then given as:

$$U_{ETM} = 2\sigma_{U,NTM,f>f_{1P}} \quad (3.2.11)$$

The values obtained can then be applied to Eq (3.2.1) to generate the maximum thrust force ( $F_{wind,ETM}$ ) acting on the wind turbine under a ETM. Subsequently, the overturning moment caused by the thrust force on the wind turbine in a ETM can be obtained with the equation:

$$M_{wind,NTM} = F_{wind,ETM}(S + Z_{hub}) \quad (3.2.12)$$

where  $S$  is the water depth and  $z_{hub}$  is the tower hub height, both in meters. The environmental load factor of  $\gamma_L = 1.25$  must be incorporated to both the loadings as well.

The extreme operating gust (EOG) model is considered to exert the greatest wind load in one single event. By following the ultimate limit state (ULS) criterion, this aerodynamic load is derived based on the 50-year EOG and when this model occurs at the rated wind speed ( $U_R$ ), it will result in the most critical load scenario applied to the turbine rotor. For an EOG model at rated wind speed ( $U_R$ ), the 50-year EOG can be estimated based on the site's distribution of 10 minutes mean wind speed (DNV, 2014). The cumulative distribution function (CDF) [ $\Phi_{U10}(K,s)$ ] can be calculated with the formula from Bhattacharya (P-75):

$$\Phi_{U10}(K,s) = 1 - e^{-\left(\frac{U}{K}\right)^s} \quad (3.2.13)$$

where  $K$  is the Weibull scale parameter (m/s) with a value of 10.95 (m/s) and  $s$  is the Weibull shape parameter with a value of 1.38 (Bury, 1999). After this, the CDF of 1-year wind speed of 10-minutes interval can be determined with the equation:

$$\Phi_{U10,1-year}(K,s) = \Phi_{U10}(K,s)^{52596} \quad (3.2.14)$$

The number 52596 represents the number of 10-minute interval wind speed in a year (Bhattacharya, 2019). The extreme wind conditions for 50-year extreme wind speed ( $U_{10,50-year}$ ), has a CDF of 0.98, can then be calculated with the equation:

$$U_{10,50-year} = K[-\ln(1 - 0.98^{\frac{1}{52596}})]^{\frac{1}{s}} \quad (3.2.15)$$

According to Bhattacharya (P-75), the **extreme gust speed** ( $U_{EOG,U_R}$ ) at  $U_R$  is determined with the equations:

$$U_{EOG} = \min \left\{ 1.35(U_{10,1-year} - U_R) ; \frac{3.3\sigma_{U,c}}{1 + \frac{0.1D}{A_1}} \right\} \quad (3.2.16)$$

$$\sigma_{U,c} = 0.11 U_{10,1-year} \quad (3.2.17)$$

$$U_{10,1-year} = 0.8 U_{10,50-year} \quad (3.2.18)$$

where  $D$  is the rotor diameter and  $A_1 = L_k/8$ ,  $L_k$  is the integral length scale. After obtaining  $U_{EOG}$ , The total wind thrust force and the mudline bending moment can be estimated with the equations:

$$F_{wind,EOG} = Th_{EOG} = 0.5\rho_a A_R C_{th} (U_R + U_{EOG,U_R})^2 \quad (3.2.19)$$

$$M_{wind,EOG} = F_{wind,EOG} (S + Z_{hub}) \quad (3.2.20)$$

and the environmental load factor of  $\gamma_L=1.25$  must be incorporated to both the loadings as well.

For an **EOG model at a cut-out wind speed** ( $U_{out}$ ) scenario, the wind turbine experiences an EOG with the highest operational wind speed also known as the cut-out wind speed ( $U_{out}$ ). In this condition, the thrust coefficient expression of Frohboese et al. (2010) cannot be applied. The pitch control is assumed to maintain the constant power, indicating that the thrust coefficient is directly proportional to the rated wind speed ( $U_R$ ) and inversely proportional to the cut-out wind speed ( $U_{out}$ ) and hence, the thrust coefficient is calculated differently with the formula from Bhattacharya (P-76):

$$C_{th} = \frac{\frac{7}{8} U_R^2}{U_{out}^3} \quad (3.2.21)$$

The procedures to determine the extreme gust speed ( $U_{EOG,out}$ ) at  $U_{out}$  is similar to the  $U_{EOG,U_R}$  at  $U_R$ . The total wind thrust force and the mudline bending moment can be estimated with the equations:

$$F_{wind,EOG_{out}} = Th_{EOG_{out}} = 0.5 \rho_a A_R C_{th} (U_R + U_{EOG,U_{out}})^2 \quad (3.2.22)$$

$$M_{wind,EOG_{out}} = F_{wind,EOG_{out}} (S + Z_{hub}) \quad (3.2.23)$$

and the environmental load factor of  $\gamma_L=1.25$  must be incorporated to both the loadings as well

### 3.3 Hydrodynamic Loading Analysis

Hydrodynamic forces are evaluated based on the most sever cases where the wave heights ( $H$ ) are the largest. A common practice is to consider a 3-hour interval when obtaining the significant wave height ( $H_s$ ). During this time period, the significant wave height is calculated by averaging the highest one-third of the waves observed. As a result, many wave heights fluctuate throughout the 3-hour span, with the largest recorded height being the maximum wave height ( $H_{max}$ ). To accurately determine this value, it is essential to know the total number of waves ( $N$ ) within the 3-hour interval, as a higher number of waves increases the probability of encountering larger waves (Bhattacharya, P-257). The equation to calculate  $N$  is as follows:

$$N = \frac{10800s}{T_s} \quad (3.3.1)$$

where  $T_s$  is the peak wave period taken as:

$$T_s = 11.1 \sqrt{\frac{H_s}{g}} \quad (3.3.2)$$

where  $H_s$  is the significant wave height in meters and  $g$  is the gravitational acceleration.

According to DNV standards, wave load calculations focused solely on the most extreme wave conditions which are the 1-year and 50-year maximum wave heights that represents the wave conditions expected annually and accepted benchmark for **extreme events respectively**. Based on DNV (2014), the 1-year equivalent significant wave height ( $H_{s,1}$ ) and wave period ( $T_{s,1}$ ) can be derived from the 50-year return period significant wave height ( $H_{s,50}$ ) and wave period ( $T_{s,50}$ ) with equations from Bhattacharya (P-306):

$$H_{s,1} = 0.8H_{s,50} \quad (3.3.3)$$

$$T_{s,1} = 11.1 \sqrt{\frac{H_{s,1}}{g}} \quad (3.3.4)$$

where the value of  $H_{s,50}$  is 5.2 m and  $T_{s,50}$  is 7.2 based on the obtained site data from Petronas (2019). According to Bhattacharya (P-257), the  $x$  year return period, maximum wave height  $H_{m,x-year}$  and maximum wave period  $T_{m,x-year}$  is determined by:

$$H_{m,x-year} = H_{s,x-year} \sqrt{0.5 \ln(N)} \quad (3.3.5)$$

$$T_{m,x-year} = 11.1 \sqrt{\frac{H_{m,x-year}}{g}} \quad (3.3.6)$$

The hydrodynamic load on the submerged monopile foundation is made up of two main components which are the **drag force** that is related to the velocity of the water particles,  $u_x(t)$ , and the **inertial force** which is related to the acceleration of the water particles,  $\partial u_x(t)/\partial t$  (Morison et al., 1950). Morison's equation is commonly employed to calculate these drag and inertial forces acting on the submerged monopile foundation (e.g., Brouwers and Verbeek, 1983) as follows:

$$F_{wave}(t) = \int_0^{d_w} (f_D + f_I) dz_w$$

$$F_{wave}(t) = \int_0^{d_w} \left( C_D \rho_w \frac{D_p}{2} u_x(t) |u_x(t)| + C_m \rho_w \frac{\pi D_p^2}{4} \frac{\partial u_x(t)}{\partial t} \right) dz_w \quad (3.3.7)$$

where  $F_{wave}(t)$  is the hydrodynamic concentrated loading varying with time acting on the monopile foundation at the mean water level (MWL);  $f_D$  and  $f_I$  are drag force and inertial force at  $z_w$ , respectively;  $z_w$  is a given height above the pile bottom;  $\rho_w$  is the density of seawater;  $C_D$  and  $C_M$  are the drag coefficient and mass coefficient which are taken as 1.2 and 2.0 for a tubular section (Haldar et al., 2018).

The hydrodynamic loads can be calculated with simplified equations from Morison et al. (1950), where the wave load ( $F_{wave}$ ) can be calculated with the formula:

$$F_{wave} = F_{D,max} + F_{I,max} \quad (3.3.8)$$

where the drag force component  $F_{D,max}$  is calculated with:

$$F_{D,max} = 0.5\rho_w D_s C_D \frac{\pi^2 H^2}{T^2 \sinh^2(kS)} P_D(k, S, n) \quad (3.3.9)$$

$$P_D(k, S, n) = \frac{e^{2k(S+n)} - e^{-2k(S+n)}}{8k} + \frac{S+n}{2} \quad (3.3.10)$$

and the inertia force component  $F_{I,max}$  is calculated with:

$$F_{I,max} = 0.5\rho_w D_s^2 C_m \frac{\pi^3 H}{T^2 \sinh^2(kS)} P_I(k, S, n) \quad (3.3.11)$$

$$P_I(k, S, n) = \frac{\sinh(k(S+n))}{k} \quad (3.3.12)$$

The overturning moment ( $M_{wave}$ ) at the seabed level caused by the total wave loads is calculated from the equation:

$$M_{wave}(t) = \int_{-s}^n dF_d(S + z_{hub})dz + \int_{-s}^n dF_I(S + z_{hub})dz \quad (3.3.13)$$

$$M_{wave} = M_{D,max} + M_{I,max} \quad (3.3.14)$$

The overturning moment at the seabed level caused by the drag force of the wave loads ( $M_{D,max}$ ) is calculated from the equation:

$$M_{D,max} = 0.5\rho_w D_s C_D \frac{\pi^3 H^2}{T^2 \sinh^2(kS)} Q_D(k, S, n) \quad (3.3.15)$$

$$Q_D(k, S, n) = \left(\frac{S+n}{8k} - \frac{1}{16k^2}\right) e^{2k(S+n)} - \left(\frac{S+n}{8k} - \frac{1}{16k^2}\right) e^{-2k(S+n)} + \left(\frac{S+n}{2}\right)^2 + \frac{1}{8k^2} \quad (3.3.16)$$

The overturning moment at the seabed level caused by the inertia force of the wave loads ( $M_{I,max}$ ) is calculated from the equation:

$$M_{I,max} = 0.5\rho_w D_s^2 C_m \frac{\pi^3 H}{T^2 \sinh^2(kS)} Q_I(k, S, n) \quad (3.3.17)$$

$$Q_I(k, S, n) = \left(\frac{S+n}{2k} - \frac{1}{2k^2}\right) e^{k(S+n)} - \left(\frac{S+n}{2k} - \frac{1}{2k^2}\right) e^{-k(S+n)} + \left(\frac{1}{k^2}\right) \quad (3.3.18)$$

Where:

$k$  = wave number

$S$  = water depth, m

$n$  = surface elevation, m

$H$  = design wave height, m

$T$  = design wave period, s

$D_s$  = substructure diameter, m

$z_{hub}$  = hub height, m

$\rho_w$  = water density, kg/m<sup>3</sup>

After achieving the wave loads ( $F_{wave}$ ) and overturning moments ( $M_{wave}$ ), an environmental load factor  $\gamma_L = 1.25$  must be incorporated into the values.

### 3.4 Initial Geometry Estimation

A study by Velarde et. al. (2017) has examined the challenges and viability of expanding monopile technology to support larger wind turbines and in deeper waters with depths of 20, 30, 40 and 50 meters. Based on the report, the monopile located at a 50-meter depth was suggested a design with an outer diameter of 10.0 meter and thickness of 125 mm, as well as an embedment depth of 4.5D (45 m).

According to API (2005), the initial monopile wall thickness can be estimated with the equation:

$$t_p \geq 6.35 + \frac{D_{out}}{100} \text{ mm} \quad (3.4.1)$$

Where  $t_p$  is the monopile wall thickness (mm) and  $D_{out}$  is the monopile outer diameter (m). According to Bhattacharya (2019), the following condition must be satisfied to prevent yielding of pile:

$$\frac{D_{out}}{I_p} \leq \frac{2f_{yk}}{\gamma_m M_{wind,EOG}}; \text{ultimate yield strength, } f_{yk} > 316 \text{ MPa} \quad (3.4.2)$$



Where  $\gamma$  is the material factor with a value of 1.1. Due to this requirement to prevent yielding a, structural steel S355 of the industrial standard can be chosen as the pile material, which has an ultimate yield strength of 335 MPa. Correspondingly, the value of the Young's modulus, density and Poisson's ratio in the elastic range must be obtained from the EN 1993-1-1:2005+AC2:2009 Sections 3.2.1 & 3.2.6. Then, the moment of inertia ( $I_p$ ) has to be determined using the equation:

$$I_p = \frac{1}{8} (D_{out} - t_p)^3 t_p \pi \quad (3.4.3)$$

The embedment depth of the monopile is estimated with the equation:

$$L = 4.0 \frac{(E_p I_p)^{\frac{1}{5}}}{n_h} \quad (3.4.4)$$

The modulus of subgrade reaction ( $n_h$ ) is obtained with the equation:

$$n_h = \frac{A \times \gamma'}{1.35} \quad (3.4.5)$$

where  $A = 600$ , is the subgrade coefficient for medium soil (Bhattacharya, 2019), and the submerged unit weight  $\gamma' = 8 \text{ kN/m}^3$ .

The total length ( $L_T$ ) of the monopile foundation is determined by the type of grout connection between the transition piece, the foundation, and the water depth. Typically, apart from the embedment depth, the remaining length spans the distance from the seabed to the water surface.

### 3.5 Design Technique

The design follows the numerical based method as explained in Chapter 2 by using the Plaxis Designer Monopile (PMD) software as the main platform for data input and 1D modelling of the pile. The Plaxis 3D software is linked to PMD to help perform the 3D modelling of soil layers and the structure, mesh generations and staged constructions. The Plaxis 3D Output viewer will then be used to locate the targeted nodes to focus on results generation. The following procedures are the steps to achieving the final results for the horizontal force vs mudline lateral displacement graph and the overturning moment vs mudline rotation graph.

#### 3.5.1 Soil Mode

Prior to the calibration of 3D FE models, the first step is to define the soil profile in the soil mode, which involves entering specific soil property parameters into the software's soil model. For clayey soils, undrained behaviour is assumed and modelled using the NGI-ADP model (Plaxis, 2018). In the case of sandy soils, drained behaviour is assumed and represented by the HSsmall model (Plaxis, 2018). In PMD, the soil profile is inputted using the data shown in Table 3.1.1 earlier.

Table 3.5.1 Required Parameters for Soil Profile at Site.

Clayey Soil	Sandy Soil
Submerged unit weight, $\gamma'$ (kN/m <sup>3</sup> )	
Lateral earth pressure coefficient at rest, $K_0$	
Small strain shear stiffness modulus in the middle of the soil layer, $G_0$ (kN/m <sup>2</sup> )	
Undrained shear strength at the bottom of the soil layer, $S_{u,bottom}$ (kN/m <sup>2</sup> )	Effective angle of internal friction, $\phi'$ (°)
Undrained shear strength at the top of the soil layer, $S_{u,top}$ (kN/m <sup>2</sup> )	Angle of dilatancy, $\psi$ (°)

### 3.5.2 Calibration Mode

A number of pre-selected sets of monopile geometries, including parameters such as outer diameter, wall thickness, pile embedment depth, and applied load height, needs to be initially defined for 3D FE model calibration. This process aims to extract the raw soil reaction curves and monopile responses. At this stage, the calibration begins with the definition of both site-specific soil profiles and the selected monopile geometries. Two dimensionless parameters represent the design space which are the pile embedment depth to outer diameter ratio ( $L/D_o$ ) and the pile head to outer diameter ratio ( $h/D_o$ ). These parameters are selected to ensure that the final monopile design fits within the boundaries set by these calibration models. The accuracy of the final analysis is influenced by the number of calibrations, with a **minimum of 8-10 calibration models** required (Plaxis, 2018). The initial estimates for the monopile geometric parameters are based on data from existing monopile-supported offshore wind turbines and research articles from the literature reviews and are summarised as follows:

Table 3.5.2 Geometry Datasets of Monopiles for Calibration.

<b>Geometry Datasets</b>	<b>Water depth, h (m)</b>	<b>Embedment depth, L (m)</b>	<b>Outer Diameter, Dout (m)</b>	<b>Pile thickness, t (m)</b>	<b><math>v_g/D_{out}</math></b>
GeoDS_1	25.00	15.00	5.000	0.05000	0.2000
GeoDS_2	20.00	35.00	9.000	0.11000	0.2000
GeoDS_3	30.00	45.00	9.000	0.11000	0.2000
GeoDS_4	40.00	35.00	10.00	0.12500	0.2000
GeoDS_5	50.00	45.00	10.00	0.12500	0.2000
GeoDS_6	50.00	60.00	7.500	0.08135	0.2000
GeoDS_7	30.00	41.00	8.000	0.08000	0.2000
GeoDS_8	60.00	45.00	8.000	0.08000	0.2000
GeoDS_9	66.00	42.00	8.400	0.08500	0.2000
GeoDS_10	100.00	35.00	7.000	0.07000	0.2000

The monopile geometry dataset is characterized by several factors: the height at which an eccentric load is applied above the **mudline ( $h$ )**, the **embedment depth ( $L$ )**, the **outer diameter of the pile ( $D_{out}$ )**, the **wall thickness ( $t_p$ )**, and the **target relative displacement at the mudline ( $v_g/D_{out}$ )**. All these parameters except the latter are having units in meters. Additionally, the steel material's structural properties are specified according to the Eurocode standards. The structural steel properties include the automatically generated **pile unit weight ( $\gamma'$ )**, adjustable **Young's modulus ( $E$ )**, which has a default value and the **Poisson's ratio ( $\nu$ )**. The first two parameters are both programmed with units in  $\text{kN/m}^3$ .

The calibration of each pre-selected calibration model is analysed and computed individually in PMD, together with the specified soil profile, by clicking the generation button. Plaxis 3D software will automatically be launched separately, while maintaining a dynamic link to the existing project data. The 3D FEM monopile structure is then constructed for one pre-selected calibration geometry within the soil model, including mesh and node generation. Monopile slicing is also automatically generated by dividing each monopile into slices in Plaxis 3D. This step is to extract responses and raw soil reactions at each mesh layer. After that, the software assigns structural properties by applying the structural properties to the 3D FEM.

Subsequently, the software then performs numerical calculation to solve the system equations to obtain the three-dimensional distribution of the monopile response and soil reactions. Correspondingly, the calculation phases begin with an initial phase that generates the initial stress state. After that, phase 1 which introduce the monopile using the "wished in place" method. This phase is a modelling assumption where the monopile is introduced into the soil **without simulating the installation process**. It essentially means the element is **fitted** into its final position without disturbing the surrounding soil or inducing installation-related stresses or deformations. Then, phase 2 is continued by performing a small displacement calculation to capture the monopile's response at a displacement of approximately  $D_{out}/10000$ . Lastly, phase 3 conducts a large displacement calculation to capture the monopile's response in the large displacement region, where the lateral displacement at the mudline is about  $D_{out}/10$ . According to Plaxis (2018), the displacement

observed at the mudline is typically less than the specified input value for maximum displacement,  $V_{\max}$ . This process is repeated for all geometry dataset from the first to the tenth. Each model generation and calculation process are time-intensive, potentially requiring several hours to produce a model and soil reaction curves for a single dataset.

### 3.5.2.1 Parametrization of Soil Reaction Curves

When monopile foundations are modelled in 3D using finite element (FE) analysis, the initial results provide raw soil reaction curves, which represent how the soil reacts to the monopile. However, these curves are complex and need to be simplified (parametrized) to make them more useful for analysis. The steps for parametrization include **normalization** - adjusting the raw soil reaction curves so that they are in a standard form for easier comparison, **fitting mathematical models** - applying equations to each raw soil reaction curve and its parameters along the length of the monopile to describe the soil behaviour, and **deriving depth variation functions** - creating functions that describe how the soil reaction changes with depth along the monopile.

After these steps, the depth variation functions (DVF) have to be generated for each soil parameter, which shows the soil's behaviour changes along the length of the monopile. **DVFs** are crucial for defining the variation of soil reaction behaviour with depth in 1D finite element calculations. These functions determine how the lateral and moment soil resistances are distributed along the monopile and can either be **automatically generated via the calibration mode** or **manually specified**. These functions will be split into two categories: shaft (the sides of the monopile) and base (the bottom of the monopile). The fitting process will require 16 DVF parameters to model the soil reactions at different depths as shown in Appendix A. The results from this parametrization are needed to perform a quick 1D FE analysis, which will be compared to a more detailed 3D FE model for verification. The accuracy of these models can be measured using a metric ( $\eta$ ) to check how well they align, especially in terms of predicting mudline lateral displacement, which is important for ensuring the structure's stability.

### 3.5.3 Analysis Mode

The analysis mode in PMD enables efficient 1D finite element simulations to evaluate monopile behavior under lateral monotonic loading. Utilizing Timoshenko beam theory for the monopile and user-defined or calibrated soil reaction curves for the surrounding soil, this mode offers a streamlined yet robust approach to foundation assessment. Accurate outcomes depend on ensuring that the monopile's geometry and structural characteristics fall within the validated design space defined by the original 3D calibration models. For numerical-based designs, this compatibility is automatically embedded within the .dvf file (Plaxis, 2018). If the input parameters exceed the bounds of the calibration space, the software issues a warning to indicate potential inaccuracy in results. Unlike the calibration mode, the monopile can be modelled with varying wall thicknesses across segments, allowing for advanced geometric optimization. Once the analysis is complete, detailed outputs can be reviewed in the results mode for performance verification and design validation.

Earlier when the calibration mode has been executed, a system-generated “.dvf ” file is saved in the project directory and automatically re-imported every time the analysis mode is accessed, ensuring up-to-date and consistent data (Brinkgreve et al., 2020). This calibrated option becomes the default when available in analysis mode and is practiced in this study. Alternatively, the **custom** method allows engineers to manually import user-defined “.dvf ” files from a dropdown menu, enabling flexibility for site-specific data or advanced research applications. Once loaded, the file name appears under the “Selected file” label. This functionality supports a transparent and customizable workflow that ensures both design accuracy and flexibility in modelling varying soil conditions along the monopile shaft.

The setup of a monopile model in analysis mode involves defining key geometric and structural parameters critical for accurate simulation. Each calculation uses a single monopile geometry, including inputs such as the embedded depth ( $L$ ), the height ( $h$ ) of load application above the mudline, and the outer diameter ( $D_{out}$ ). Structural properties such as the Young's modulus ( $E$ ) are adjustable, while the software sets both the distributed weight ( $w$ ) and Poisson's ratio ( $\nu$ ) to zero by default. This simplification reflects the 1D beam modelling approach, where Poisson effects in thin-walled tubular sections are considered negligible. Loads applied at the monopile

head is specifically a horizontal force ( $H$ ) and moment ( $M$ ) which can be set with reference to a specific elevation, and an equivalent ground-level bending moment:  $M_g = H \cdot h + M$  is calculated accordingly.

The thickness variation tool also allows the segmentation of the pile into sections with different wall thicknesses ( $t$ ) for refined modelling. Segment boundaries and properties can be customized, with clear rules governing their insertion, deletion, and editing. From the defined inputs, key mechanical properties—such as cross-sectional area ( $A$ ), axial stiffness ( $EA$ ), flexural rigidity ( $EI$ ), shear stiffness ( $GA$ ), and moment of inertia ( $I$ ) are computed automatically, ensuring consistency and structural accuracy in the model. This integrated approach enables efficient optimization and precise representation of monopile behaviour under lateral loading.

The expert settings panel allows for fine control over the numerical aspects of the 1D finite element simulation, providing the flexibility to tailor the analysis for specific project needs. This includes setting a minimum monopile section length to ensure adequate discretization, particularly for longer piles or segmented geometries. The maximum number of calculation steps that can be defined (default of 1000) governs the resolution of the load application. A tolerance for numerical error is also included, with a default value of 0.0001, ensuring convergence is reached with sufficient precision. Load application per step is managed via the maximum load fraction, defaulting to 0.1, which helps maintain numerical stability during non-linear response phases. Users can set a maximum iteration count per step (default 100) to control solver efficiency. Finally, a limit on the displacement-to-diameter ratio (default 0.1) is included to prevent unrealistic pile deformations. These settings enable more accurate and stable simulations, especially when dealing with complex loading conditions or geometry variations.

The **results inspection** pane in PMD provides a comprehensive interface for reviewing and interpreting output data generated from the processed “.dvf ” file following a 1D finite element calculation. Accessed after initiating the simulation via the *Calculate* button, this pane is divided into three distinct tabs which are **Soil Reaction Curves**, **Shaft Depth Variation Functions**, and **Base Depth Variation Functions**, each offering specific insights into pile-soil interaction behaviour. In the **soil reaction curves** tab, the lateral response of the soil at multiple depths along the

embedded length of the monopile can be examined. The analysis divides the pile's embedded depth ( $L$ ) into ten equal intervals (from  $0.1L$  to  $1.0L$ ), with depths rounded to the nearest 0.5 meters to facilitate standardized output (Plaxis, 2018). These depths correspond to locations where the soil's lateral resistance is evaluated and displayed through parameterized curves derived from the “.dvf” data. These curves, shown clearly in the graphical interface, represent the soil's response to lateral displacement and help assess variation in stiffness and capacity along the pile shaft. A depth legend on the left side of the display provides quick reference, ensuring clarity in interpretation and assisting engineers in verifying design consistency and identifying depth-specific behaviours. This structured visualization plays a crucial role in validating design assumptions and refining monopile configurations based on site-specific soil response (Plaxis, 2018).

#### **3.5.4 Results Mode**

The results mode in PMD serves as the central hub for evaluating the output of 1D calculations conducted in analysis mode. It also offers the option to display and compare results from previously calibrated 3D models, enabling the assessment of the consistency and accuracy metrics of the simplified 1D approach against more detailed 3D simulations. To activate this comparison, the relevant 3D model must be manually selected from a drop-down list, ensuring that the chosen model matches the parameters of the 1D scenario under review. Results for both the 1D and 3D models are presented in the form of interactive graphs and structured tables, allowing selectively visualizing specific data such as displacements, reactions, or moment distributions based on their analysis needs. In this study, the focus is limited to the relationships between horizontal force against lateral displacement, and overturning moment against mudline rotation. According to the serviceability limit state (SLS) criteria, the lateral displacement must remain below  $0.1D_{out}$ , and the mudline rotation must not exceed 0.5 degrees.



#### **3.5.4.1 Optimization of Monopile Geometry**

Optimising monopile geometry in PMD requires a consistent and accurate workflow between the 1D and 3D modelling processes. This includes making adjustments by trial and error to pile dimensions, segment thickness, or loading conditions. The results mode allows the viewing of the outputs from the most recent 1D analysis to compare them directly with the already generated 3D model results.

#### **3.5.4.2 Construct 3D FEM for Verification**

It is important to understand that the results shown are not automatically updated for the 3D results. They reflect only the data from the last executed 1D calculation. If any changes are made to the monopile geometry and a new 1D model is introduced, the 3D analysis must be rerun to ensure that the comparison remains valid. This step is essential for maintaining data consistency and for making informed design decisions. Re-running the analysis after every modification allows the assessment performance metrics accurately and fine-tune the geometry for both structural efficiency and compliance with site-specific soil behaviour, supporting a more reliable and economical design.

If the calculation fails, the View button can be used to inspect the associated 3D model in Plaxis 3D for further analysis. Refinements can be made by adjusting the mesh to a finer resolution and reducing the maximum load fraction per step to enhance numerical stability and accuracy. Once all modifications have been completed and saved, both PLAXIS 3D and the Output Viewer should be properly closed before re-running the calculation in PLAXIS Monopile Designer. This step ensures that all updates are fully applied, allowing the analysis to proceed smoothly and ultimately produce valid results.

## CHAPTER 4

### RESULTS AND DISCUSSIONS

#### 4.1 Loads Analysis

##### 4.1.1 Self-weight

One of the main factors in load analysis is the wind turbine structure's self-weight since it has a big influence on the foundation requirements and tower design. The Rotor Nacelle Assembly (RNA) and the tower are the primary elements that contribute to the self-weight, as seen in Table 4.1.1. The tower itself, at 90 meters tall, weighs 190 tonnes, while the RNA, which consists of the hub and blades, weighs about 350 tonnes. A total of 540 tonnes, or 540,000 kg, make up the structural weight overall.

Table 4.1.1: Total Structural Weight (Siemens, 2025).

Components	Weight
Rotor Nacelle Assembly (RNA)	350 T
Blades x3	
Hub	
Tower max (90 meters)	190 T
<b>Total Structure Weight</b>	<b>540 T (540000 kg)</b>

A deadload safety factor of 1.35 is incorporated into the design process to accommodate for safety tolerances, and the mass is converted into force using the formula  $w=mg$ , where  $m$  is the mass and  $g$  is the gravitational acceleration of  $9.81 \text{ m/s}^2$ . These are used to calculate the self-weight that the structure exerts:

$$Gk = (1.35)(540000 \times 9.81) = 7151.490 \text{ kN}$$

It is necessary to precisely incorporate this self-weight, which operates vertically downward, into the structural design process using PLAXIS 3D. It effects the stability analysis against tipping, impacts the tower's load-bearing needs, and is crucial in determining the foundation's size. Maintaining the tower's stability in both typical operation and severe weather scenarios requires a thorough grasp of the self-weight.

## 4.1.2 Aerodynamic Load Analysis

### 4.1.2.1 Normal Turbulence Scenario

This scenario describes the wind load at normal operating conditions. At a normal turbulence scenario, a normal turbulence model (NTM) is used for evaluation of aerodynamic loads. The NTM calculation of the maximum thrust force ( $F_{wind,NTM}$ ) acting on the wind turbine uses the equation from Bhattacharya (2019):

$$F_{wind,NTM} = 0.5\rho_a A_R C_{th}(U_R + U_{NTM})^2$$

$$F_{wind,NTM} = 0.5(1.225)(11500)(0.61)(11.8862 + 0.957)^2$$

$$F_{wind,NTM} = 708729.09 \text{ N} = 708.73 \text{ kN}$$

where  $\rho_a$  is the density of air ( $\text{kg/m}^3$ );  $A_R$  is the rotor swept area ( $\text{m}^2$ );  $C_{th}$  is the thrust coefficient, which depends on the mean wind speed at hub (Bhattacharya, 2019).  $U_R$  is the rated wind speed ( $\text{m/s}$ ) and  $U_{NTM}$  is the maximum turbulent intensity component ( $\text{m/s}$ ). The determination of  $U_{NTM}$  firstly requires the calculation of the standard deviation of normal turbulence ( $\sigma_{U,NTM}$ ) with the equation obtained from IEC (2005):

$$\sigma_{U,NTM} = I_{ref}(0.75U + b)$$

$$\sigma_{U,NTM} = (0.21)(0.75(6.79) + 5.6)$$

$$\sigma_{U,NTM} = 2.25$$

where  $I_{ref}$  (0.21) from? is the reference turbulent intensity,  $U$  is the mean wind speed at 90 m above sea level ( $\text{m/s}$ ) and  $b$  has a value of 5.6  $\text{m/s}$  (Bhattacharya, 2019). This  $\sigma_{U,NTM}$  will then be incorporated into a formula based on a Kaimal spectrum model to obtain an overall standard deviation,  $\sigma_{U,NTM,f>f_{1p}}$  :

$$\sigma_{U,NTM,f>f_{1p}} = \sigma_{U,NTM} \sqrt{\frac{1}{(\frac{6Lk}{U_R} f_{1p,max} + 1)^{\frac{2}{3}}}}$$

$$\sigma_{U,NTM,f>f_{1p}} = (2.25) \sqrt{\frac{1}{(\frac{6(259.95)}{11.8862} (0.2) + 1)^{\frac{2}{3}}}}$$

$$\sigma_{U,NTM,f>f_{1p}} = 0.7478$$

Where  $f_{1p,max} = 0.2$ , is the rotor frequency for a 6.0 MW wind turbine is the maximum rotor frequency (Hz). The turbulence integral length scale ( $Lk$ ) is used to model the spatial distribution of turbulence in the wind flow.  $Lk$  can be calculated with the equation:

$$Lk = 300 \left( \frac{z}{300} \right)^{0.46+0.074 \ln(z_0)}$$

$$Lk = 300 \left( \frac{90}{300} \right)^{0.46+0.074 \ln(0.01)}$$

$$Lk = 259.95$$

Where  $z_0$  is the terrain roughness of open sea with wave with a value of 0.01, and  $z$  is the height above sea level in meters. From Bhattacharya, (P-74), the equation provided to calculate the  $U_{NTM}$  is given as:

$$U_{NTM} = 1.28 \sigma_{U,NTM,f>f_{1p}}$$

$$U_{NTM} = 1.28(0.7478)$$

$$U_{NTM} = 0.957$$

The thrust coefficient ( $C_{th}$ ) between the cut-in wind speed and the rated wind speed is calculated is determined according Bhattacharya (2019), following the method outlined by Frohboese et al. (2010), with the equation:

$$C_{th} \approx \frac{3.5 \frac{m}{s} (2U_R + 3.5 \frac{m}{s})}{U_R^2} \approx \frac{7 \frac{m}{s}}{U_R}$$

$$C_{th} \approx \frac{7 \frac{m}{s}}{U_R} \approx \frac{7 \frac{m}{s}}{11.5563} \approx 0.6057$$

These value can then be applied to Eq (4.1.2) to generate the maximum thrust force ( $F_{wind,NTM}$ ) acting on the wind turbine under a NTM. Subsequently, the overturning moment caused by the thrust force on the wind turbine in a NTM ( $M_{wind,NTM}$ ) can be obtained with the equation:

$$\begin{aligned}
 M_{wind,NTM} &= 1.35 \times F_{wind,NTM}(S + Z_{hub}) \\
 M_{wind,NTM} &= (708.73kN)(60 + 90) \\
 \mathbf{M_{wind,NTM} = 106.309 MNm}
 \end{aligned}$$

where S is the water depth and  $z_{hub}$  is the tower hub height, both in meters. The environmental load factor of  $\gamma_L = 1.25$  must be incorporated to both the loadings as well.

#### 4.1.2.2 Extreme Turbulent Scenario

Calculation of the **maximum thrust force** ( $F_{wind,ETM}$ ) acting on the wind turbine:

$$\begin{aligned}
 F_{wind,ETM} &= 0.5\rho_a A_R C_{th}(U_R + U_{ETM})^2 \\
 F_{wind,ETM} &= 0.5(1.225)(11500)(0.61)(11.8862 + 3.042)^2 \\
 \mathbf{F_{wind,ETM} = 957.522 kN}
 \end{aligned}$$

The parameters remain the same with the NTM model except for  $U_{ETM}$  which is the maximum turbulent intensity component (m/s) that differs. As for the ETM, the determination of  $U_{ETM}$  also requires the calculation of the standard deviation of normal turbulence ( $\sigma_{U,ETM}$ ) with the equation obtained from IEC (2005):

$$\begin{aligned}
 \sigma_{U,ETM} &= cI_{ref} \left[ 0.072 \left( \frac{U}{c} + 3 \right) \left( \frac{U_R}{c} - 4 \right) + 10 \right] \\
 \sigma_{U,ETM} &= (2)(0.21) \left[ 0.072 \left( \frac{6.79209}{2} + 3 \right) \left( \frac{11.8862}{2} - 4 \right) + 10 \right] \\
 \sigma_{U,ETM} &= (2)(0.21)[0.072(6.40)(1.943) + 10] \\
 \mathbf{\sigma_{U,ETM} = (2)(0.21)(10.89) = 4.576}
 \end{aligned}$$

where  $c = 2$  m/s according to Bhattacharya (2019),  $I_{ref}$  is the reference turbulent intensity,  $U$  is the mean wind speed at 90 m above sea level (m/s) and  $U_R$  is the rated wind speed. This  $\sigma_{U,ETM}$  will then similarly be incorporated into a formula based on a Kaimal spectrum model to obtain an overall standard deviation,  $\sigma_{U,ETM,f>f_{1p}}$  :

$$\sigma_{U,ETM,f>f_{1p}} = \sigma_{U,ETM} \sqrt{\frac{1}{(\frac{6Lk}{U_R} f_{1p,max} + 1)^{\frac{2}{3}}}}$$

$$\sigma_{U,ETM,f>f_{1p}} = (4.576) \sqrt{\frac{1}{(\frac{6(259.9)}{11.8862} (0.2) + 1)^{\frac{2}{3}}}}$$

$$\sigma_{U,NTM,f>f_{1p}} = 1.521$$

where  $f_{1p,max} = 0.2$  for a 6.0 MW wind turbine is the maximum rotor frequency (Hz) and the turbulence integral length scale ( $Lk$ ). The equation provided from Bhattacharya, (P-74) to calculate the  $U_{ETM}$  is then given as:

$$U_{ETM} = 2\sigma_{U,NTM,f>f_{1p}}$$

$$U_{ETM} = 2(1.521) = 3.042$$

The values obtained can then be applied to Eq (3.2.1) to generate the maximum thrust force ( $F_{wind,ETM}$ ) acting on the wind turbine under a ETM. Subsequently, the overturning moment caused by the thrust force on the wind turbine in a ETM can be obtained with the equation:

$$M_{wind,NTM} = 1.35 \times F_{wind,ETM} (S + Z_{hub})$$

$$M_{wind,ETM} = (957.522kN)(60 + 90) = 143.628 MNm$$

where  $S$  is the water depth and  $z_{hub}$  is the tower hub height, both in meters. The environmental load factor of  $\gamma_L = 1.25$  must be incorporated to both the loadings as well.

#### 4.1.2.3 Extreme Operating Gust (EOG) Model at Rated ( $U_R$ ) Wind Speed

The extreme operating gust (EOG) model is considered to exert the greatest wind load in one single event. Firstly, the cumulative distribution function (CDF) [ $\Phi_{U_{10}}(K, s)$ ] can be calculated with the formula from Bhattacharya (P-75):

$$\Phi_{U_{10}}(K, s) = 1 - e^{-\left(\frac{U}{K}\right)^s}$$

where  $K$  = Weibull scale parameter (m/s) and  $s$  = Weibull shape parameter. After this, the CDF of 1-year wind speed of 10-minutes interval can be determined with the equation:

$$\Phi_{U_{10,1-year}}(K, s) = \Phi_{U_{10}}(K, s)^{52596}$$

The number 52596 represents the number of 10-minute interval wind speed in a year (Bhattacharya, 2019). The extreme wind conditions for 50-year extreme wind speed ( $U_{10,50-year}$ ), has a CDF of 0.98, can then be calculated after rearranging the equation:

$$\begin{aligned} U_{10,50-year} &= K[-\ln\left(1 - 0.98^{\frac{1}{52596}}\right)]^{\frac{1}{s}} \\ U_{10,50-year} &= 10.95[-\ln\left(1 - 0.98^{\frac{1}{52596}}\right)]^{\frac{1}{1.38}} \\ U_{10,50-year} &= 77.06 \text{ m/s} \end{aligned}$$

According to Bhattacharya (P-75), the extreme gust speed ( $U_{EOG, U_R}$ ) at  $U_R$  is determined with the equations:

$$\begin{aligned} U_{EOG} &= \min\left\{1.35(U_{10,1-year} - U_R) ; \frac{3.3\sigma_{U,c}}{1 + \frac{0.1B}{A_1}}\right\}; \\ \sigma_{U,c} &= 0.11 U_{10,1-year} = 0.11(61.65) = 6.782 \text{ m/s} \dots (2) \\ U_{10,1-year} &= 0.8 U_{10,50-year} = 0.8(77.06) = 61.65 \text{ m/s} \dots (1) \end{aligned}$$

where  $D$  is the rotor diameter and  $\Lambda_1 = L_k/8$ ,  $L_k$  is the integral length scale. Therefore,

$$\Lambda_1 = 259.95/8 = 32.49 \text{ m}^2$$

$$U_{EOG} = \frac{3.3(6.782)}{1 + \frac{0.1(120)}{32.49}} = 16.344 \text{ m/s}$$

After obtaining  $U_{EOG}$ , the total wind thrust force and the mudline bending moment at rated wind speed ( $U_r$ ) can be estimated with the equations:

$$F_{wind,EOG} = Th_{EOG} = 0.5\rho_a A_R C_{th} (U_R + U_{EOG,U_R})^2$$

$$F_{wind,EOG} = 0.5(1.225)(11500)(0.61)(11.8862 + 16.344)^2$$

$$F_{wind,EOG} = 3424 \text{ kN}$$

$$M_{wind,EOG} = F_{wind,EOG} (S + Z_{hub})$$

$$M_{wind,EOG} = 3424 \text{ kN} (60 + 90) = 513.633 \text{ MNm}$$

and the environmental load factor of  $\gamma_L=1.25$  must be incorporated to both the loadings as well.

$$F_{wind,EOG} = 1.25(3424 \text{ kN}) = 4280 \text{ kN}$$

$$M_{wind,EOG} = 3424 \text{ kN} (60 + 90) = 513.633 \text{ MNm}$$

#### 4.1.2.4 Extreme Operating Gust (EOG) Model at Cut-Out ( $U_{out}$ ) Wind Speeds

For an EOG model at a cut-out wind speed ( $U_{out}$ ) scenario, the wind turbine experiences an EOG with the highest operational wind speed also known as the cut-out wind speed ( $U_{out}$ ). In this condition, the thrust coefficient expression of Frohboese et al. (2010) cannot be applied. The pitch control is assumed to maintain the constant power, indicating that the thrust coefficient is directly proportional to the rated wind speed ( $U_R$ ) and inversely proportional to the cut-out wind speed ( $U_{out}$ ) and hence, the thrust coefficient is calculated differently with the formula from Bhattacharya (P-76):

$$C_{th} = \frac{7 \frac{m}{s} U_R^2}{U_{out}^3}$$



$$C_{th} = \frac{7 \frac{m}{s} (11.8862)^2}{2.5^3} = 0.0633$$

The procedures to determine the extreme gust speed ( $U_{EOG,out}$ ) at  $U_{out}$  is similar to the  $U_{EOG,U_R}$  at  $U_R$ . The total wind thrust force and the mudline bending moment can be estimated with the equations:

$$F_{wind,EOG_{out}} = Th_{EOG_{out}} = 0.5 \rho_a A_R C_{th} (U_{out} + U_{EOG,U_{out}})^2$$

$$F_{wind,EOG_{out}} = 0.5(1.225)(11500)(0.0633)(25 + 16.341)^2 = 762.026 \text{ kN}$$

$$M_{wind,EOG_{out}} = F_{wind,EOG_{out}} (S + Z_{hub})$$

$$M_{wind,EOG_{out}} = 762.026 \text{ kN} (60 + 90) = 114.304 \text{ MNm}$$

and the environmental load factor of  $\gamma_L=1.25$  must be incorporated to both the loadings as well.

$$F_{wind,EOG_{out}} = (1.25) 762.026 \text{ kN} = 952.5325 \text{ kN}$$

$$M_{wind,EOG_{out}} = (1.25) 114.304 \text{ kN} = 142.88 \text{ MNm}$$

#### 4.1.3 Hydrodynamic Loads Analysis

It is essential to know the total number of waves ( $N$ ) within the 3-hour interval, as a higher number of waves increases the probability of encountering larger waves (Bhattacharya, P-257). The equation to calculate  $N$  is as follows and where  $T_s$  is the significant peak wave period taken as:

$$N = \frac{10800s}{T_s}$$

$$T_s = 11.1 \sqrt{\frac{H_s}{g}}$$

where  $H_s$  is the significant wave height in meters and  $g$  is the gravitational acceleration. Based on DNV (2014), the 1-year equivalent significant wave height ( $H_{s,1}$ ) and wave period ( $T_{s,1}$ ) can be derived from the 50-year return period significant wave height ( $H_{s,50}$ ) and wave period ( $T_{s,50}$ ) with equations from Bhattacharya (P-306):

$$H_{s,1} = 0.8H_{s,50} = (0.8)(5.2) = 4.16 \text{ m}$$

where  $(H_{s,50})$  and  $(T_{s,50})$  are obtained from a site data as shown in appendix (Petronas, 2009). The following tabulated data are calculated from the mentioned equations.

Table 4.1.3.1: Tabulated results of N.

<b>Region: Abu Kecil</b>				
<b>Longitude: 105.306 E, Latitude: 6.1199 N</b>				
<b>Wave Parameters</b>	<b>1-year return period</b>	<b>10-year return period</b>	<b>50-year return period</b>	<b>100-year return period</b>
<b>Significant wave height, <math>H_s</math> (m)</b>	4.2	4.9	5.2	5.3
<b>Significant wave Period, <math>T_s</math> (s)</b>	7.23	7.85	8.1	8.20
<b>The total number of waves within the 3-hour interval (<math>N</math>)</b>	1494	1376	1333	1317

According to Bhattacharya (P-257), the x-year return period, maximum wave height  $H_{m,x-year}$  and maximum wave period  $T_{m,x-year}$  is determined by:

$$H_{m,x-year} = H_{s,x-year} \sqrt{0.5 \ln(N)}$$

$$T_{m,x-year} = 11.1 \sqrt{\frac{H_{m,x-year}}{g}}$$

Table 4.1.3.2: Calculation for maximum wave height and period.

$H_{m,1-year} = 4.2\sqrt{0.5\ln(1494)} = 8.02$	$T_{m,1-year} = 11.1\sqrt{\frac{8.02}{9.81}} = 10.36$
$H_{m,10-year} = 4.9\sqrt{0.5\ln(1376)} = 9.31$	$T_{m,10-year} = 11.1\sqrt{\frac{9.31}{9.81}} = 10.81$
$H_{m,50-year} = 5.2\sqrt{0.5\ln(1333)} = 9.86$	$T_{m,50-year} = 11.1\sqrt{\frac{9.86}{9.81}} = 11.13$
$H_{m,100-year} = 5.3\sqrt{0.5\ln(1317)} = 10.04$	$T_{m,100-year} = 11.1\sqrt{\frac{10.04}{9.81}} = 11.23$

The significant wave height ( $H_s$ ), maximum wave height ( $H_m$ ), significant wave period ( $T_s$ ) and maximum wave period ( $T_m$ ) are compared. From the Table 4.1.3.3, it is noticeable that the maximum wave height and period are larger in values. Hence, these two parameters will be taken into calculation for each return period scenarios respectively. According to DNV (2021) and API (2014) offshore structure design guidelines, the 1-year and 50-year return periods of wave profiles are sufficient and commonly used in offshore and coastal engineering design to account for both frequent operational conditions and rare extreme events.

Table 4.1.3.3 Tabulated results of  $H_m$  and  $T_m$ .

Region: Abu Kecil				
Longitude: 105.306 E, Latitude: 6.1199 N				
	Significant wave height, $H_s$ (m)	Max. wave height, $H_m$ (m)	Significant wave Period, $T_s$ (s)	Max. wave Period, $T_m$ (s)
1-year return period	4.2	8.02	7.23	10.36
10-year return period	4.9	9.31	7.85	10.81
50-year return period	5.2	9.86	8.10	11.13
100-year return period	5.3	10.04	8.20	11.23

The drag force component  $F_{D,max}$  can then be calculated with the formula:

$$F_{D,max} = 0.5\rho_w D_s C_D \frac{\pi^2 H^2}{T^2 \sinh^2(kS)} P_D(k, S, n)$$

$$P_D(k, S, n) = \frac{e^{2k(S+n)} - e^{-2k(S+n)}}{8k} + \frac{S+n}{2}$$

Table 4.1.3.4 Hydrodynamic Force Parameter and Description.

Parameter	Description
$F_{wave}(t)$	hydrodynamic concentrated loading varying with time acting on the monopile foundation at the mean water level (MWL)
$f_D$	drag force at $z_w$
$f_I$	inertial force at $z_w$
$z_w$	given height above the pile bottom
$\rho_w$	density of seawater
$D_s$	substructure diameter (meters)
$C_D$	drag coefficient 1.2 (or 1.3) for a tubular section (Haldar et al., 2018).
$C_M$	mass coefficient 2.0 for a tubular section (Haldar et al., 2018).
H	monopile head = (monopile length – embedded length)

According to Bhattacharya (2019), the  $D_s$  can be calculated with the equation:

$$D_s = 2t_{TP} + 2t_g + D_{out} ; t_{TransitionPiece} + t_{grout} = 0.15 \text{ m}$$

$$D_s = 2(0.15) + 8 = 8.3 \text{ m}$$

#### 4.1.3.1 One-Year Return Period Wave Profile

The maximum force exerted by the 1-year return period wave profile can be calculated:

$$F_{D,max} = 0.5\rho_w D_s C_D \frac{\pi^2 H_{m,1}^2}{T_{m,1}^2 \sinh^2(kS)} P_D(k, S, n)$$

The function  $P_D(k, S, n)$  is calculated with the formula:

$$P_D(k, S, n) = \frac{e^{2k(S+n)} - e^{-2k(S+n)}}{8k} + \frac{S+n}{2}$$

Where  $t = \frac{T_{m,1}}{4}$  and  $n = \frac{H_{m,1}}{2}$ . Therefore,  $t = 10.36/4 = 2.59\text{s}$ ;  $n = 8.02/2 = 4.01\text{m}$ .

Angular wave number is achieved by trial-and-error method. Where  $S$  is the water depth,  $T_s$  is the 50-year significant wave peak period and  $g$  is the gravitational acceleration.

$$k = \frac{4\pi^2}{T_s^2 g \tanh(kS)} = 0.054$$

Hence,

$$P_D(k, S, n) = \frac{e^{2k(S+n)} - e^{-2k(S+n)}}{8k} + \frac{S+n}{2}$$

$$P_D(k, S, n) = \frac{e^{2(0.054)(60+4.01)} - e^{-2(0.054)(60+4.01)}}{8(0.054)} + \frac{60+4.01}{2}$$

$$P_D(k, S, n) = \frac{992.3 - 0.001}{0.432} + 32$$

$$P_D(k, S, n) = 2359.176$$

Therefore,

$$\begin{aligned}
 F_{D,max} &= 0.5(1030)(8.3)(1.3) \frac{\pi^2 8.02^2}{10.36^2 \sinh^2(0.054)(60)} (2359.176) \\
 F_{D,max} &= (5556.85) \frac{634.82}{17440.32} (2359.176) \\
 \mathbf{F_{D,max} = 477.183 \text{ kN}}
 \end{aligned}$$

Then, the inertia force component  $F_{I,max}$  can then be calculated:

$$\begin{aligned}
 F_{I,max} &= 0.5\rho_w D_s^2 C_m \frac{\pi^3 H_{m,1}}{T_{m,1}^2 \sinh^2(kS)} P_I(k, S, n) \\
 P_I(k, S, n) &= \frac{\sinh(k(S+n))}{k} \\
 P_I(k, S, n) &= \frac{\sinh(0.054(60+4.01))}{0.054} = 293.30 \\
 F_{I,max} &= 0.5(1030)(8.3)^2(2.0) \frac{\pi^3(8.02)}{10.36^2 \sinh^2(0.054)(60)} (293.30) \\
 F_{I,max} &= (70956) \frac{(248.67)}{(17440.32)} (293.30) \\
 \mathbf{F_{I,max} = 296.735 \text{ kN}}
 \end{aligned}$$

Then, the total horizontal force exerted by the wave is summed:

$$\begin{aligned}
 F_{wave} &= F_{D,max} + F_{I,max} \\
 \mathbf{F_{wave,1-yr} = 477.183 + 296.735 = 773.918 \text{ kN}}
 \end{aligned}$$

The overturning moment ( $M_{wave}$ ) at the seabed level caused by the total wave loads is calculated from the equation:

$$M_{wave} = M_{D,max} + M_{I,max}$$

The overturning moment at the seabed level caused by the drag force of the wave loads ( $M_{D,max}$ ) is calculated from the equation:

$$M_{D,max} = 0.5\rho_w D_s C_D \frac{\pi^2 H^2}{T^2 \sinh^2(kS)} Q_D(k, S, n)$$

$$Q_D(k, S, n) = \left( \frac{S+n}{8k} - \frac{1}{16k^2} \right) e^{2k(S+n)} - \left( \frac{S+n}{8k} - \frac{1}{16k^2} \right) e^{-2k(S+n)} + \left( \frac{S+n}{2} \right)^2 + \frac{1}{8k^2}$$

$$Q_D(k, S, n) = \left( \frac{60 + 4.01}{8(0.054)} - \frac{1}{16(0.054)^2} \right) e^{2(0.054)(60+4.01)} - \left( \frac{60 + 4.01}{8(0.054)} - \frac{1}{16(0.054)^2} \right) e^{-2(0.054)(60+4.01)} + \left( \frac{60 + 4.01}{2} \right)^2 + \frac{1}{8(0.054)^2}$$

$$Q_D(k, S, n) = (148.17 - 21.43)e^{6.91} - (148.17 - 21.43)e^{-6.91} + (1024.32 + 42.87)$$

$$Q_D(k, S, n) = 127024.82 - 0.1265 + 1067.19$$

$$Q_D(k, S, n) = 128422.64$$

$$M_{D,max} = 0.5(1030)(8.3)(1.3) \frac{\pi^2 8.02^2}{10.36^2 \sinh^2(0.054 \times 60)} (128,422.64)$$

$$M_{D,max} = (5556.85) \frac{634.817}{17440.322} (128,422.64)$$

$$\mathbf{M_{D,max} = 25.975525 \text{ MNm}}$$

The overturning moment at the seabed level caused by the inertia force of the wave loads ( $M_{I,max}$ ) is calculated from the equation:

$$M_{I,max} = 0.5\rho_w D_s^2 C_m \frac{\pi^3 H}{T^2 \sinh^2(kS)} Q_I(k, S, n)$$

$$Q_D(k, S, n) = \left( \frac{S+n}{2k} - \frac{1}{2k^2} \right) e^{k(S+n)} - \left( \frac{S+n}{2k} - \frac{1}{2k^2} \right) e^{-k(S+n)} + \left( \frac{1}{k^2} \right)$$

$$Q_D(k, S, n) = \left( \frac{64.01}{2(0.054)} - \frac{1}{2(0.054)^2} \right) e^{(0.054)(64.1)} - \left( \frac{64.01}{2(0.054)} - \frac{1}{2(0.054)^2} \right) e^{-(0.054)(64.1)} + \left( \frac{1}{(0.054)^2} \right)$$

$$Q_D(k, S, n) = 13776.88$$

where  $k$  = wave number;  $S$  = water depth, m;  $n$  = surface elevation, m;  $H$  = design wave height, m;  $T$  = design wave period, s;  $D_s$  = substructure diameter, m;  $z_{hub}$  = hub height, m;  $\rho_w$  = water density, kg/m<sup>3</sup>.

$$M_{I,max} = 0.5(1030)(8.3)^2(2.0) \frac{\pi^3(8.02)}{10.36^2 \sinh^2(0.054)(60)} (13776.88)$$

$$\mathbf{M_{I,max} = 13.938,427 MNm}$$

Then, the total overturning moment exerted by the wave is summed:

$$M_{wave} = M_{D,max} + M_{I,max}$$

$$M_{wave,1-yr} = 25.976 + 13.939 = 39.915 \text{ MNm}$$

#### 4.1.3.2 Fifty-Year Return Period Wave Profile

The 50-year return period wave profile is evaluated with the same procedure. The maximum wave drag load is calculated:

$$F_{D,max} = 0.5\rho_w D_s C_D \frac{\pi^2 H_{m,50}^2}{T_{m,50}^2 \sinh^2(kS)} P_D(k, S, n)$$

The function  $P_D$  can be calculated with the formula:

$$P_D(k, S, n) = \frac{e^{2k(S+n)} - e^{-2k(S+n)}}{8k} + \frac{S+n}{2}$$

Where  $t = \frac{T_{m,50}}{4}$  and  $n = \frac{H_{m,50}}{2}$ . Therefore,  $t = 11.13/4 = 2.7825\text{s}$ ;  $n = 9.86/2 = 4.93\text{m}$ .

$$P_D(k, S, n) = \frac{e^{2k(S+n)} - e^{-2k(S+n)}}{8k} + \frac{S+n}{2}$$

$$P_D(k, S, n) = \frac{e^{2(0.054)(64.93)} - e^{-2(0.054)(64.93)}}{8(0.054)} + \frac{64.93}{2}$$

$$P_D(k, S, n) = 2602.74$$

$$F_{D,max} = 0.5(1030)(8.3)(1.3) \frac{\pi^2 9.86^2}{11.13^2 \sinh^2(0.054)(60)} (2602.74)$$

$$\mathbf{F_{D,max} = 689.4261 kN}$$



and the inertia force component  $F_{I,max}$  is calculated with:

$$F_{I,max} = 0.5\rho_w D_s^2 C_m \frac{\pi^3 H_{m,1}}{T_{m,1}^2 \sinh^2(kS)} P_I(k, S, n)$$

$$P_I(k, S, n) = \frac{\sinh(k(S+n))}{k}$$

$$P_I(k, S, n) = \frac{\sinh(0.054(64.93))}{0.054} = 308.26$$

$$F_{wave} = F_{D,max} + F_{I,max}$$

$$F_{wave,50-yr} = 689.426 + 332.209 = 1022 \text{ kN}$$

$$F_{I,max} = 0.5(1030)(8.3)^2 (2.0) \frac{\pi^3 (9.86)}{11.13^2 \sinh^2(0.054)(60)} (308.26)$$

$$F_{I,max} = 332.20932 \text{ kN}$$

The overturning moment at the seabed level caused by the drag force of the wave loads ( $M_{D,max}$ ) is calculated from the equation:

$$M_{D,max} = 0.5\rho_w C_D D_s \frac{\pi^2 H^2}{T^2 \sinh^2(kS)} Q_D(k, S, n)$$

$$Q_D(k, S, n) = \left( \frac{S+n}{8k} - \frac{1}{16k^2} \right) e^{2k(S+n)} - \left( \frac{S+n}{8k} - \frac{1}{16k^2} \right) e^{-2k(S+n)} + \left( \frac{S+n}{2} \right)^2 + \frac{1}{8k^2} \quad (3.3.10)$$

$$Q_D(k, S, n) = \left( \frac{60 + 4.93}{8(0.054)} - \frac{1}{16(0.054)^2} \right) e^{2(0.054)(60+4.93)} - \left( \frac{60 + 4.93}{8(0.054)} - \frac{1}{16(0.054)^2} \right) e^{-2(0.054)(60+4.93)} + \left( \frac{60 + 4.93}{2} \right)^2 + \frac{1}{8(0.054)^2}$$

$$Q_D(k, S, n) = 144186.06$$

$$M_{D,max} = 0.5(1030)(8.3)(1.3) \frac{\pi^2 9.86^2}{11.13^2 \sinh^2(0.054 \times 60)} (144186.06)$$

$$M_{D,max} = (5556.85) \frac{959.519}{20129.144} (144186.06)$$

$$M_{D,max} = 38.192687 \text{ MNm}$$

The overturning moment at the seabed level caused by the inertia force of the wave loads ( $M_{I,max}$ ) is calculated from the equation:

$$M_{I,max} = 0.5\rho_w D_s^2 C_m \frac{\pi^3 H}{T^2 \sinh^2(kS)} Q_I(k, S, n)$$

$$Q_D(k, S, n) = \left( \frac{S+n}{2k} - \frac{1}{2k^2} \right) e^{k(S+n)} - \left( \frac{S+n}{2k} - \frac{1}{2k^2} \right) e^{-k(S+n)} + \left( \frac{1}{k^2} \right)$$

$$Q_D(k, S, n) = \left( \frac{64.93}{2(0.054)} - \frac{1}{2(0.054)^2} \right) e^{(0.054)(64.93)} - \left( \frac{64.93}{2(0.054)} - \frac{1}{2(0.054)^2} \right) e^{-(0.054)(64.93)} + \left( \frac{1}{(0.054)^2} \right)$$

$$Q_D(k, S, n) = 14649.73$$

$$M_{I,max} = 0.5(1030)(8.3)^2(2.0) \frac{\pi^3(9.86)}{11.13^2 \sinh^2(0.054)(60)} (14649.73)$$

$$\mathbf{M_{I,max} = 15.787896 MNm}$$

Then, the total overturning moment exerted by the wave is summed:

$$M_{wave} = M_{D,max} + M_{I,max}$$

$$\mathbf{M_{wave,50-yr} = 38.193 + 15.788 = 38.981 MNm}$$

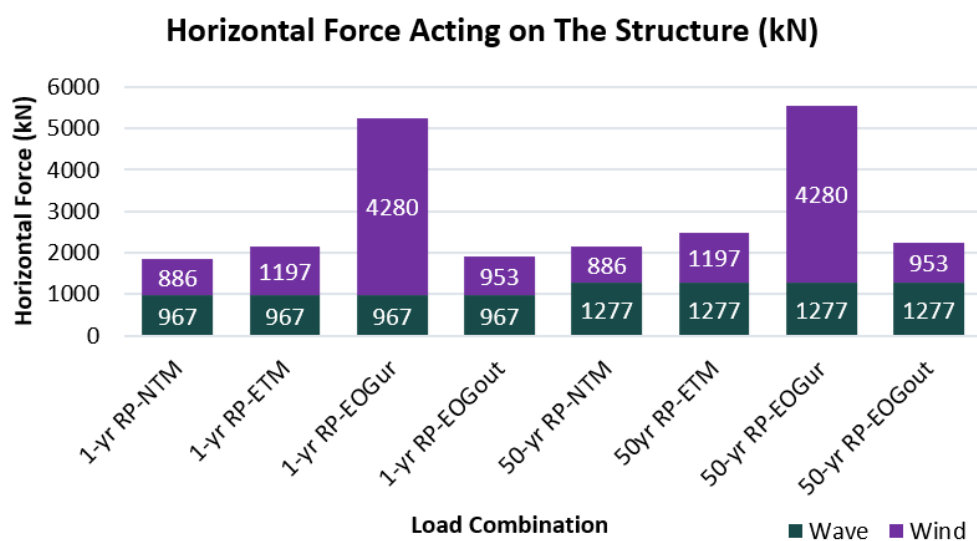
#### 4.1.4 Loads Analysis Discussion

After achieving the wave loads ( $F_{wave}$ ) and overturning moments ( $M_{wave}$ ), an environmental load factor  $\gamma_L = 1.25$  must be incorporated into the values. The data are tabulated as follows:

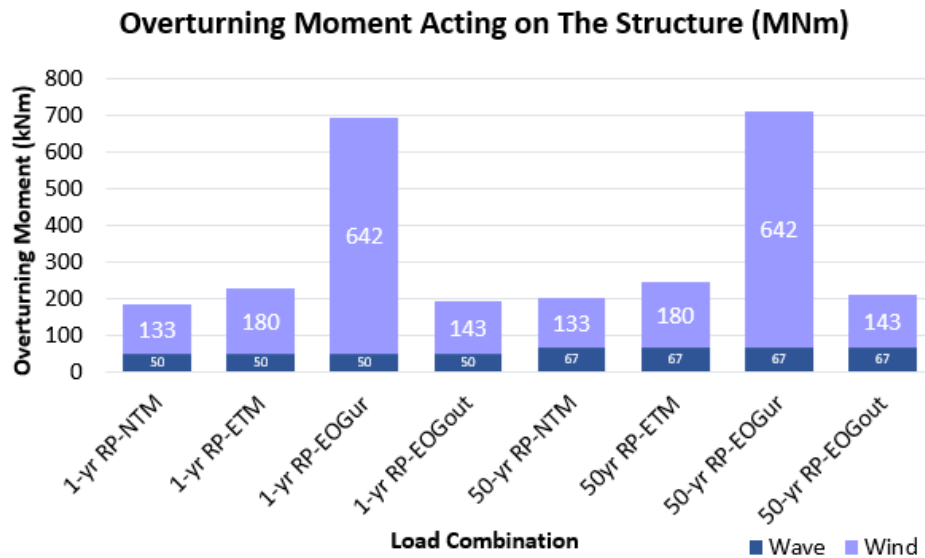
Table 4.1.4 Tabulated Data of Metocean Loads.

Metocean Horizontal Loads	Wave		Wind			
	1-yr RP	50-yr RP	NTM	ETM	EOGur	EOGout
Max. load (kN)	773.918	1021.635	708.73	957.522	3424	762.026
Environmental SF (x1.25)	967.3975	1277.0438	885.9125	1196.9025	4280	952.5325

Metocean Horizontal Loads	Wave		Wind			
	1-yr RP	50-yr RP	NTM	ETM	EOGur	EOGout
Max. moment (MN)	39.915	53.981	106.309	143.628	513.633	114.304
Environmental SF (x1.25)	49.89375	67.47625	132.88625	179.535	642.04125	142.88



Graph 4.1.4.1 Horizontal Force Acting on The Structure.



Graph 4.1.4.2 Overturning Moment Acting on The Structure.

The graphs 4.1.4.1 and 4.1.4.2 illustrates the horizontal force and overturning moment acting on a marine structure under different environmental load combinations. They are consistent with established empirical and theoretical knowledge on offshore structural loading. Specifically, these graphs highlight how extreme gust events such as the extreme operating gust at rated wind speed (EOG<sub>ur</sub>) produce the most critical loading conditions, both in terms of lateral forces up to 4280 kN and overturning moments that reaches 642 MNm. The extreme case combinations in this study happens to peak at the 50-year RP and EOG<sub>ur</sub> scenario, producing a combined horizontal force of 5777 kN and overturning moment of 709 MNm. These values are not only realistic but fall within expected design limits for offshore wind turbine (OWT) support structures, especially for monopile foundations, under wave conditions with return periods (RP) of one and fifty years.

Recent investigations have confirmed that wind gust loading plays a dominant role in moment amplification, particularly when applied at hub heights. For instance, Abdullahi et al. (2022) modelled various wind cases and observed that horizontal wind loads in extreme events can generate mudline moments exceeding 600 MNm, similar to the peak values evaluated in this study. Another study conducted by Arshad & O'Kelly (2016) states that offshore monopiles subjected to simultaneous wave and wind loads experience maximum structural stress during turbulent wind gust events. Their analysis showed that under extreme environmental combinations, the horizontal

force from wind could significantly exceed typical wave loading, particularly at the superstructure level. This explains the peak values observed during the one-year or fifty-year RP-EOG<sub>ur</sub> scenarios in the graph. Moreover, the research emphasized that wind loading, especially from sudden gusts, introduces large transient horizontal forces that drastically increase overturning moments at the seabed level, consistent with the 642 MNm observed in the presented results.

Moreover, Hallowell, Myers, and Arwade (2016) examined variability in breaking wave characteristics and their impact on monopile-supported OWTs. Their study found that under breaking wave conditions combined with storm winds, horizontal loads could reach 4000–5000 kN, and mudline overturning moments ranged from 600 to 700 MNm, depending on the stiffness and height of the monopile. This enhances the validity of your extreme loading scenario values, especially under RP with EOG<sub>ur</sub> or EOG<sub>out</sub> cases. Besides that, wave loading contributes a stable yet substantial component of both horizontal force and moment. In wave-dominated scenarios such as those under long-period swell or nonlinear wave crests, the forces can reach up to 1500–2000 kN without any wind influence (Zeng et al., 2021). This aligns with the examined data, where wave-only scenarios consistently produce base forces above 900 kN, even in the absence of significant wind consideration. The results are especially realistic in the context of nonlinear wave impacts, as emphasized by Wang et al. (2021), who used a fully nonlinear wave model to analyse a 10 MW monopile-supported turbine. Their results showed that irregular wave crests and breaking waves produced forces and moments within the same range of magnitude observed in the graphs.

Recent literature also shows that the effect of wave-current interaction, as modelled by Buljac et al. (2022), leads to additional complexities in monopile loading. Their study, which included simultaneous wind, wave, and current simulations, found that total moment values could increase by over 20% when wave-current interactions were modelled versus wave-only assumptions. This supports the data reflecting simultaneous peak combinations that is capturing more than just linear superposition.

Overall, the combined values shown in graphs 4.1.4.1 and 4.1.4.2 especially the 5777 kN peak force and 709 MNm overturning moment are fully consistent with recent experimental and simulation studies. The data is reflective of both upper-bound

design scenarios and average operational loading under current offshore environmental modeling. The environmental loads evaluation closely aligns with recommended design thresholds and modern modelling practices which confirms the necessity of coupled environmental load combinations in structural design for offshore wind applications. The behaviour where gust-related combinations result in the highest values is a well-documented phenomenon in offshore structural engineering. The results are therefore structurally acceptable, and reflect a rigorous and conservative approach to environmental load modelling.

## 4.2 Initial Geometry Estimation

The initial monopile wall thickness can be estimated with the equation (API, 2005):

$$t_p \geq 6.35 + \frac{D_{out}}{100} mm$$

$$t_p \geq 6.35 + \frac{8000}{100} = 86.35 mm$$

$$t_p \approx 90 mm$$

According to Bhattacharya (2019), the following condition must be satisfied to prevent yielding of pile:

$$\frac{D_{out}}{I_p} \leq \frac{2f_{yk}}{\gamma_m M_{wind,EOG}} ;$$

*ultimate yield strength,  $f_{yk} > 316 MPa$*

Where  $\gamma$  is the material factor with a value of 1.1. Then, the area moment of inertia ( $I_p$ ) of the cross section has to be determined using the equation:

$$I_p = \frac{1}{8} (D_{out} - t_p)^3 t_p \pi$$

$$I_p = \frac{1}{8} (8000 - 90)^3 (90) \pi = 17.49 \times 10^{12} mm^4$$

$$\frac{8000(513.633 MNm)}{17.49 \times 10^{12}} \leq \frac{2f_{yk}}{(1.1)}$$

$$129.25 MPa \leq f_{yk} = 335 MPa$$

Due to this requirement to prevent yielding a, structural steel S355 of the industrial standard can be chosen as the pile material, which has an ultimate yield strength  $f_{yk}$  of 335 MPa. Correspondingly, the value of the Young's modulus, density and Poisson's ratio in the elastic range are obtained from the EN 1993-1-1:2005+AC2:2009 Sections 3.2.1 & 3.2.6:

Table 4.2.1: Steel Properties of The Monopile

Parameter	Values
Yield stress, $f_{yk}$ (MPa)	335
Young's modulus, $E_P$ (MPa)	210000
Density, $\rho$ ( $kg/m^3$ )	7850
Poisson's ratio in the elastic range, $\nu$	0.3

The initial pile diameter can then be calculated with the equation:

$$\frac{D_p}{I_p} \leq \frac{2f_{yk}}{\gamma_m M_{wind,EOG}}$$

$$\frac{D_p}{(17.49 \times 10^{12})} \leq \frac{2(335)}{(1.1)(513.633 \text{ MNm})}$$

$$D_p \leq 20731.8 \text{ mm}$$

Since  $8000 \text{ mm} < 20721.8 \text{ mm}$ , hence, 8 m diameter is suitable. The embedment depth of the monopile is estimated with the equation:

$$L = 4.0 \frac{(E_P I_p)^{\frac{1}{5}}}{n_h}$$

The modulus of subgrade reaction ( $n_h$ ) is obtained with the equation:

$$n_h = \frac{A \times \gamma'}{1.35}$$

$$n_h = \frac{(600) \times (8000 \text{ N/m}^3)}{1.35} = 3.56 \text{ MN/m}^3$$

where  $A = 600$ , is the subgrade coefficient for medium soil (Bhattacharya, 2019), and the submerged unit weight  $\gamma' = 8 \text{ kN/m}^3$ .

$$L = 4.0 \frac{(E_p I_p)^{\frac{1}{5}}}{n_h}$$

$$L = 4.0 \frac{((21 \times 10^{10}) \text{ Pa} \times (17.49 \times 10^{12}) \text{ mm}^4)^{\frac{1}{5}}}{3.56 \times 10^6 \text{ N/m}^3} = 63.6 \text{ m} \approx 65 \text{ m}$$

The total length ( $L_T$ ) of the monopile foundation is determined by the type of grout connection between the transition piece, the foundation, and the water depth. Typically, apart from the embedment depth, the remaining length spans the distance from the seabed to the water surface. Hence, the initial monopile dimensions are 8-diameter monopile, pile thickness of 90 mm, and 65 m embedment depth which makes the total pile length 125 m long. The initial geometries are tabulated below:

Table 4.2.2 Initial Monopile Geometries

<b>Water Depth (h)</b>	<b>Embedment Depth (L)</b>	<b>Pile Outer Diameter (D<sub>out</sub>)</b>	<b>Pile Thickness (t)</b>
60 m	65 m	8 m	0.09 m



### 4.3 Monopile Calibration Models Results

Figure 4.3 shows the colour coding for each geometry dataset (GeoDS). This colour code is used to represent each respective GeoDS for the reaction of horizontal force vs lateral displacement as presented in Graph 4.3.

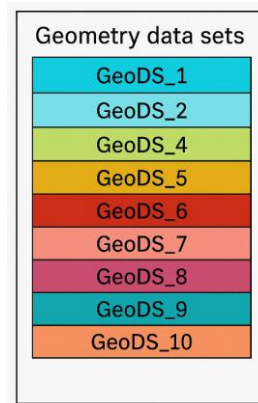
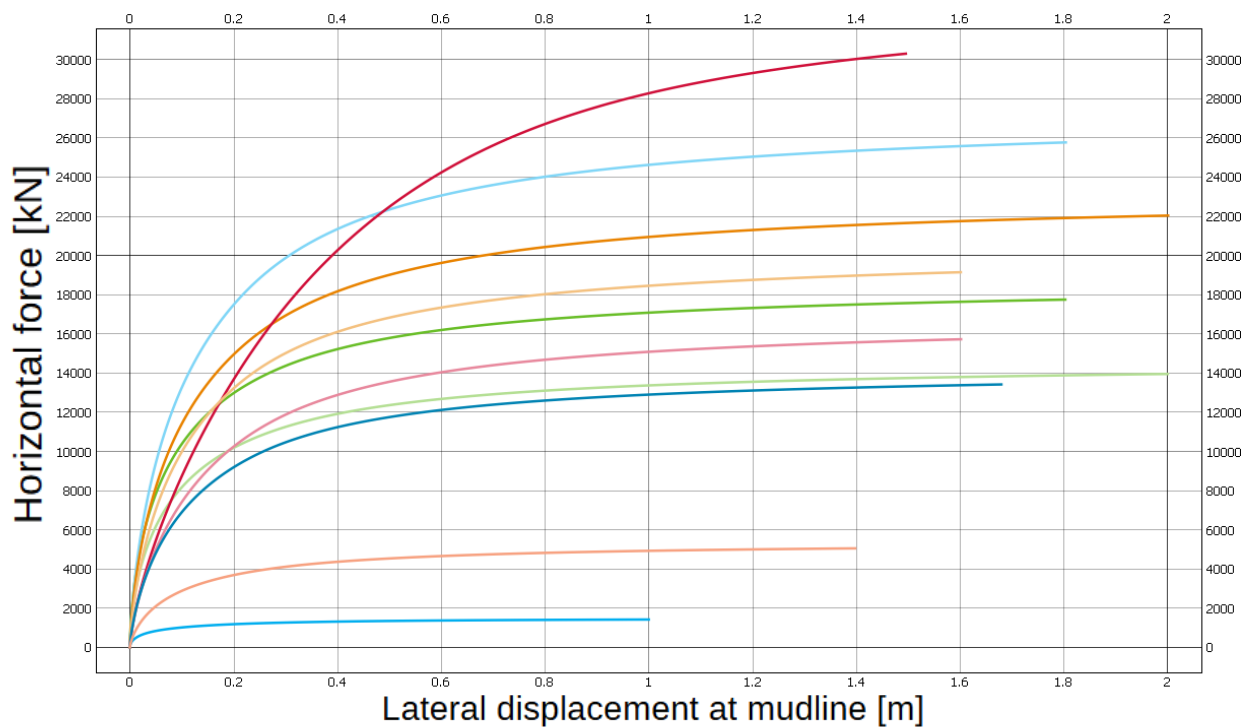


Figure 4.3.1 Colour Coding for Respective Geometry Dataset.



Graph 4.3.2 Horizontal Force (kN) vs Lateral Displacement (m) for Calibrated Monopile Geometries.

Graph 4.3.2 shows the horizontal force (kN) vs lateral displacement (m) for calibrated monopile geometries. In Plaxis Monopile Designer's calibration mode, the horizontal force results are not user-defined inputs but are instead reactions generated by the soil in response to a prescribed lateral displacement at the mudline. This mode is specifically designed to calibrate p–y curves, and it does so by simulating soil-structure interaction (SSI). As displacement increases, the model computes how much resistance the surrounding soil mobilizes. This explains why a force is produced even though no external horizontal load was applied. The large magnitude of these generated forces occurs due to the full mobilization of soil resistance due to the large imposed lateral displacements by the software.

The model considers nonlinear soil behaviour, and once certain displacement thresholds are crossed, resistance escalates sharply. Moreover, the monopile's structural geometry particularly its embedment depth, diameter, and wall thickness significantly amplify the magnitude of the mobilized forces. Aleem et al. (2024) observed that in simulation environments like Plaxis, high soil stiffness and pile rigidity in deeper soils tend to generate significant force magnitudes, especially when lateral displacements are imposed to extreme levels as part of the calibration process.

Among the geometries analysed, GeoDS 6 exhibited the highest force capacity, while GeoDS 1 the lowest. This difference can be attributed to the contrast in their geometric and structural parameters. GeoDS 6 had a large outer diameter of 7.5 m, thick wall, and the deepest embedment of 60 m, all of which contributed to higher lateral stiffness and enhanced engagement with deeper, stiffer soil layers. In contrast, GeoDS 1, with the smallest diameter of 5 m, shortest pile with embedment depth of 25 m, and thinnest wall, offered minimal structural resistance and interacted with relatively weaker upper soil layers, resulting in the lowest horizontal force mobilization. Duan (2016) demonstrated that monopiles with greater diameter and depth mobilize more soil resistance and achieve higher bending moments and lateral forces under displacement loading.

GeoDS 5 experienced the highest lateral displacement at the mudline, while GeoDS 1 again showed the least. GeoDS 5 has a long pile length of 45 m, large diameter of 10 m, and embedment depth of 50 m, displayed significant flexibility under lateral loading, which allowed for extended deformation before mobilizing full

resistance. Conversely, GeoDS 1 has small and rigid geometry meant it reached peak soil resistance quickly with minimal lateral deflection. According to Gupta (2018), longer monopiles with relatively high length-to-diameter ratios allow greater flexibility and larger displacement capacity under soil pressure, particularly in loose to medium sands.

Interestingly, GeoDS 6, despite generating the highest horizontal force, did not display the largest displacement. This is explained by its inherently high stiffness. The thick-walled, wide-diameter monopile with deep embedment offers significant bending resistance, limiting deflection under load. As Jindal (2024) explains, high bending stiffness in monopiles leads to a steeper force–displacement curve, with rapid force build-up and limited displacement.

The force–displacement graph is essential for optimizing monopile design because it reveals how different pile geometries respond to lateral soil resistance, highlighting balance between stiffness and ductility. This enables performance-based design, ensuring piles are neither over-designed nor too flexible, and helps calibrate soil resistance models for accurate, cost-effective foundation solutions tailored to specific site conditions while ensuring serviceability and strength requirements are met.

#### 4.4 Plaxis Monopile Designer Results and Discussion

The initial geometries which include the water depth, embedment depth, pile outer diameter and pile thickness are firstly inputted into the analysis mode in the Plaxis Monopile Designer for the initial analysis as shown in Figure 4.4.1. The structural properties and workload will remain constant throughout the analysis due to the selected economical steel specification and evaluated load conditions. The adjustable Young's modulus will be set at 210000 MPa and the horizontal force exerted by the wave on the monopile at 60 m height is 1277 kN while the overturning moment occurring at the monopile head due to aerodynamic loads is  $642.0 \times 10^3$  kNm.

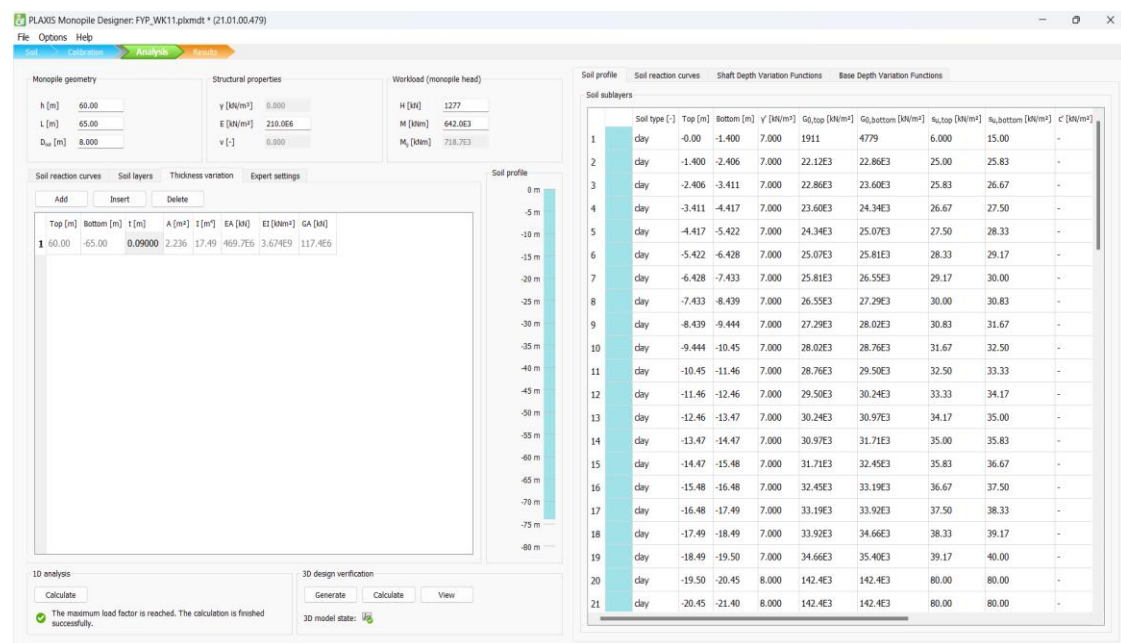
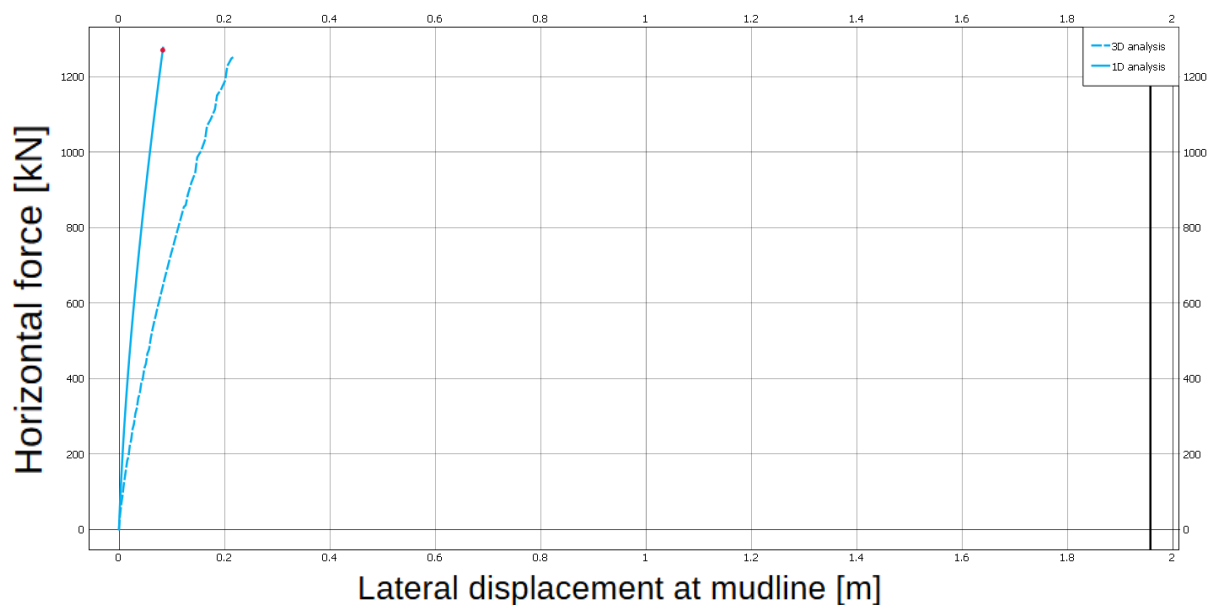
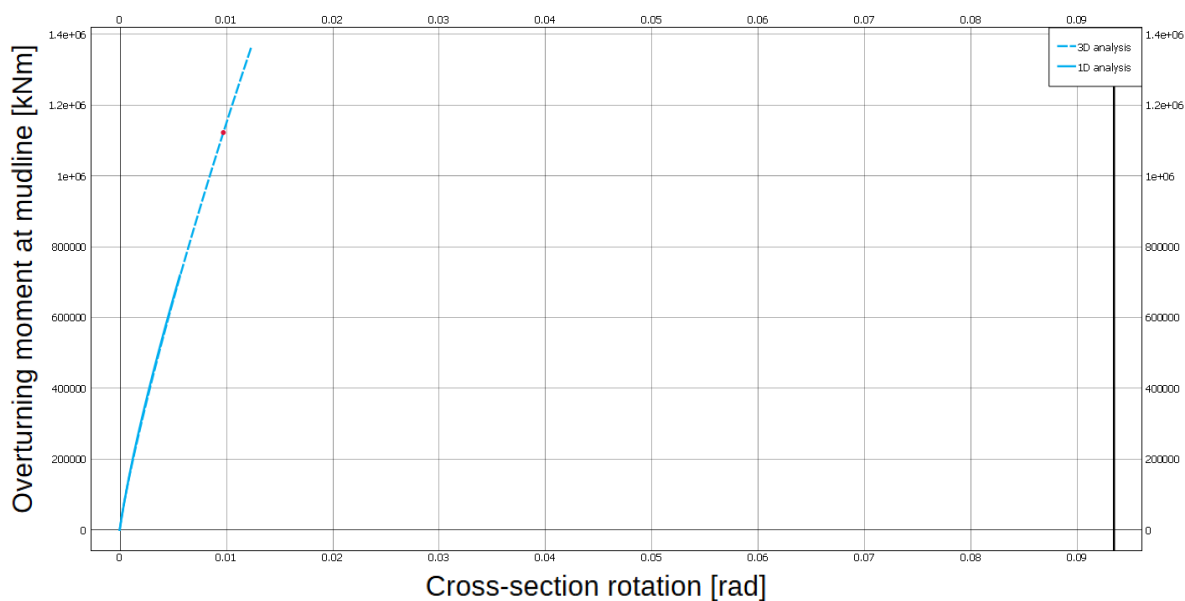


Figure 4.4.1 Interface for The Analysis Mode of The Plaxis Monopile Designer.

As seen in figure 4.4.1 the calculation for the 1D analysis and 3D analysis at the bottom left corner of the figure are both successful, with an indication of a green check mark. In the results mode, the graph for horizontal force against lateral displacement and overturning moment against cross section rotation are generated as shown in Graph 4.4.2 and 4.4.3 respectively.



Graph 4.4.2 Horizontal Force (kN) Against Lateral Displacement (m) for 65 m of embedment.



Graph 4.4.3 Overturning Moment (kNm) Against Mudline Rotation (rad.) for 65 m of embedment.

Graph 4.4.2 illustrates that both the 1D and 3D analyses exhibit closely matching trends. Despite minor variations, the results from both models remain well under the maximum threshold of 0.1D (0.8 m) for lateral displacement, indicating acceptable compliance with the design criteria for this section. Graph 4.4.3 shows that the 1D

and 3D analyses align very closely as seen. The cross-section rotation for both cases is around 0.0056 radians (roughly 0.3 degrees), which is comfortably below the serviceability limit of 0.5 degrees. This indicates that the initial geometry performs well within acceptable limits. However, achieving a more cost-effective design is still important. Hence, the pile geometry was gradually refined through a trial-and-error approach until the results met both structural requirements and practical efficiency. The optimised geometries are tabulated in Table 4.4.1 below, and the satisfactory results are generated shown in Graph 4.4.1.1 and Graph 4.4.2.1.

Table 4.4.1 Optimised Monopile Geometry

<b>Water Depth (h)</b>	<b>Embedment Depth (L)</b>	<b>Pile Outer Diameter (D<sub>out</sub>)</b>	<b>Pile Thickness (t)</b>
60 m	43 m	8 m	0.06 m

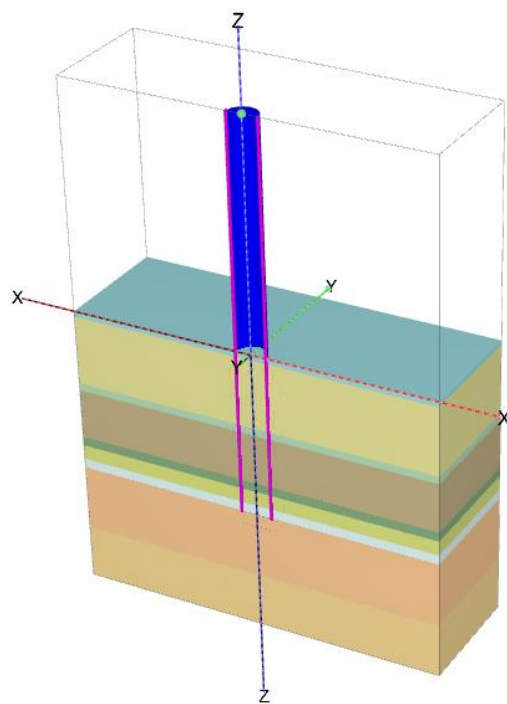
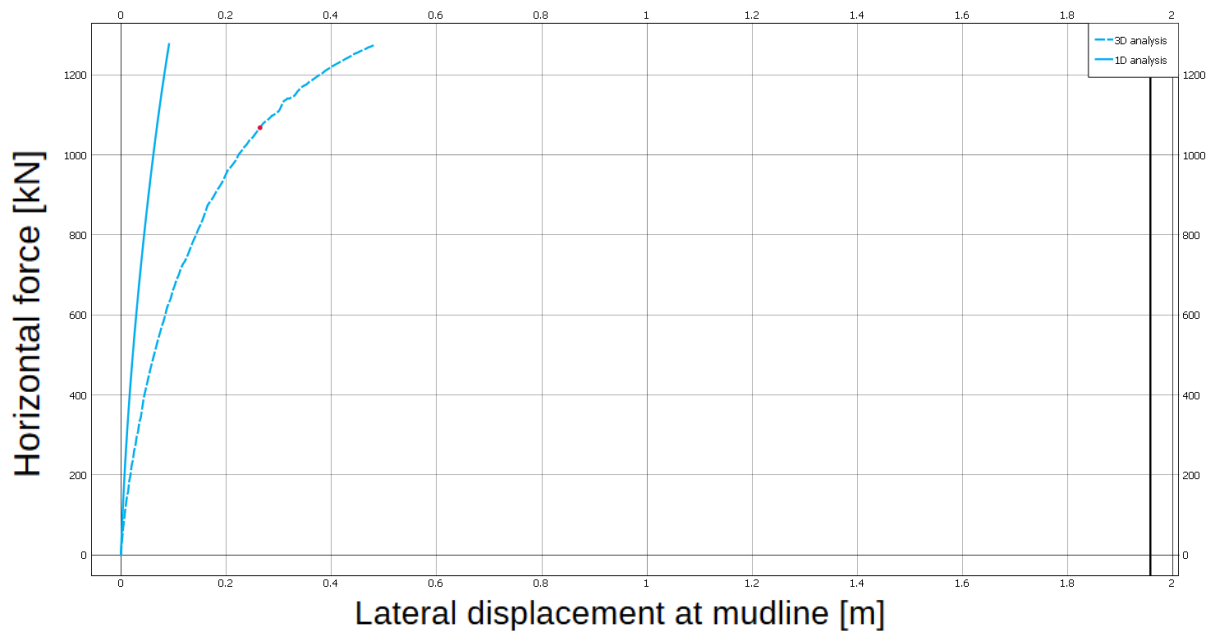


Figure 4.4.4 Optimised Monopile Geometry and Soil Layers Generated in Plaxis 3D.

#### 4.4.1 Results of Horizontal Force (kN) Against Lateral Displacement (m) for Optimised Monopile Design



Graph 4.4.1.1 Horizontal Force (kN) Against Lateral Displacement (m) for 43 m of embedment.

Graph 4.4.1.1 presents the lateral response of an 8-meter diameter monopile subjected to a horizontal wave load of 1277 kN and a head moment of 642 MNm. The analysis was conducted using PLAXIS Monopile Designer (PMD), where both 1D and 3D simulations were run for the same pile configuration for a 43-meter embedded depth and 0.6-meter wall thickness, constructed with S335 steel. The key distinction lies in the predicted lateral displacement at the applied load where the 1D analysis estimates a displacement of 0.09149 meters, while the 3D analysis shows a significantly higher value of 0.4821 meters. This difference shows that simplified approaches, such as the 1D analysis method, may not accurately reflect the true interaction between the soil and the structure under real-world conditions, often leading to an underestimation of the actual response. Despite the differences, both the 1D and 3D analysis still satisfies the required guidelines where the displacements are to be less than 0.1 times the pile outer diameter, which in this case is 0.8 m.

In the 1D analysis (solid line), the soil response is modelled using the beam-on-nonlinear-Winkler-foundation (BNWF) approach with parameterized p-y curves. These curves, while efficient and widely adopted, are inherently empirical and were

originally developed for slender, small-diameter piles. They do not account for the stress redistribution, confinement effects, or three-dimensional interaction zones that are especially relevant for large-diameter monopiles, such as the one in this study. Consequently, the 1D model tends to overestimate stiffness and underpredict displacement, potentially leading to unconservative estimates of serviceability.

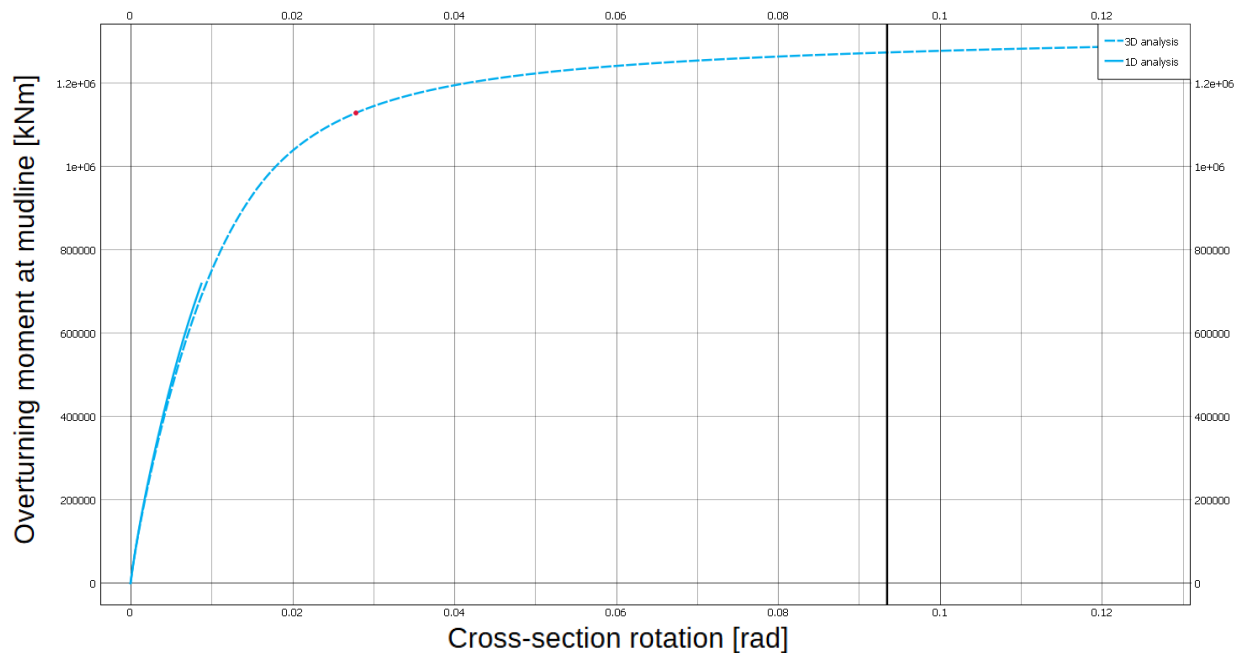
Conversely, the 3D analysis (dashed line), generated in PLAXIS 3D and visualized within PMD, captures the full continuum behaviour of the surrounding soil. It includes nonlinear material models, stress redistribution, and the complex shear transfer between soil layers. This allows for a more realistic prediction of the pile's deformation behaviour under lateral loading. Literature supports this observation; for example, Murphy et al. (2018) and Jindal et al. (2024) show that 3D FE models consistently predict greater displacements for monopiles beyond 5 meters in diameter, emphasizing that 1D models may not be sufficiently reliable for large-scale offshore foundations.

The irregular or “squiggly” pattern at the upper end of the 3D curve is another notable feature. This irregularity is typically linked to numerical convergence issues, mesh distortion, or local yielding of the soil near the pile head, where moment and rotation are highest. These fluctuations are well-documented in FE simulations of large monopiles, as discussed by Jindal et al. (2024), and often indicate the onset of plastic deformation or instability in shallow soil layers. Despite appearing visually unstable, such results still provide valuable insight into the failure mechanisms and response limits of the system.

Given that PMD uses the same underlying engine for both 1D and 3D simulations, the difference in results reflects the inherent compromise between computational efficiency and the level of accuracy achievable in modelling complex soil–structure interactions. The 1D mode offers computational efficiency and is useful for preliminary design and parametric studies. However, it lacks the depth and detail of the 3D mode, which, although more computationally intensive, offers greater reliability particularly in the serviceability limit state (SLS) assessments where precise displacement prediction is critical.



#### 4.4.2 Results of Overturning Moment (kMn) Against Mudline Rotation (rad.) for Optimised Monopile Design



Graph 4.4.2.1 Overturning Moment (kNm) Against Mudline Rotation (rad.) for 43 m of embedment.

Graph 4.4.2.1 illustrates the relationship between bending moment at the mudline and cross-section rotation for a monopile foundation analysed in both 1D and 3D using PMD. In this same case, the monopile has a diameter of 8 meters, an embedded depth of 43 meters, and a wall thickness of 0.6 meters, made from S335 steel. The applied head moment is 642 MNm.

Given the same loading conditions, the 1D model estimates a cross-section rotation of 0.0065 radians ( $0.372^\circ$ ), while the 3D model gives 0.007 radians ( $0.401^\circ$ ). Both values are well below the Serviceability Limit State (SLS) criterion of  $0.5^\circ$ , confirming that the design meets the rotational performance requirements under the applied moment.

Interestingly, unlike the previous lateral displacement comparison, the 1D and 3D curves in this case are closely aligned throughout most of the loading range. This is because the rotational response is more dominantly influenced by the monopile's flexural stiffness, which is accurately represented in both the 1D beam model and the 3D continuum model. As highlighted by Murphy et al. (2018) and Versteijlen et al.

(2016), for structural parameters like bending moment and rotation, especially in the elastic to early-plastic range, the 1D model can provide reasonable approximations when proper stiffness values are used.

However, the 3D curve continues further into higher overturning moment levels and shows a more gradual flattening at larger rotations. This extended response reflects the soil's progressive yielding and redistribution of stress around the pile, a behaviour that the 1D model is unable to fully replicate due to its limitation by predefined  $p$ - $y$  and  $m$ - $\theta$  curves. Research by Jindal et al. (2024) and Tombari et al. (2025) noted that 1D methods are adequate for routine design checks but they tend to underestimate system capacity under extreme or nonlinear loading conditions. The overestimation by the 3D analysis does not necessarily mean that the pile will experience higher bending moments in reality. Instead, it reflects that the 3D model offers a more accurate picture of how the soil and structure interact under load. The 3D model which accounts for soil softening and stress redistribution, may show a longer or extended response curve but still remain within serviceability limits. The difference does not imply that the pile is structurally inadequate, but rather that the 3D model provides a more conservative and reliable basis for assessment, especially when evaluating soil-structure interaction under large or complex loading.

Ultimately, the smaller difference between the 1D and 3D results for rotation, as compared to the noticeable gap in lateral displacement, suggests that rotational stiffness is influenced more by the monopile's own structural properties than by variations in local soil conditions. This explains why both modelling approaches produce similar outcomes in terms of rotation. However, when dealing with more complex loading scenarios, layered or variable soil profiles, or when higher precision is required, 3D modelling remains the more dependable choice due to its ability to capture detailed soil-structure interaction effects.

In summary, while the 1D analysis remains a valuable tool for conceptual design, this study clearly demonstrates that for large-diameter monopiles under significant lateral loads, 3D modelling is essential for achieving accurate and reliable predictions. The insights derived from PMD reaffirm the importance of choosing the right level of modelling detail depending on the design stage and performance requirements.

#### 4.4.3 Calibrated Design Space Check

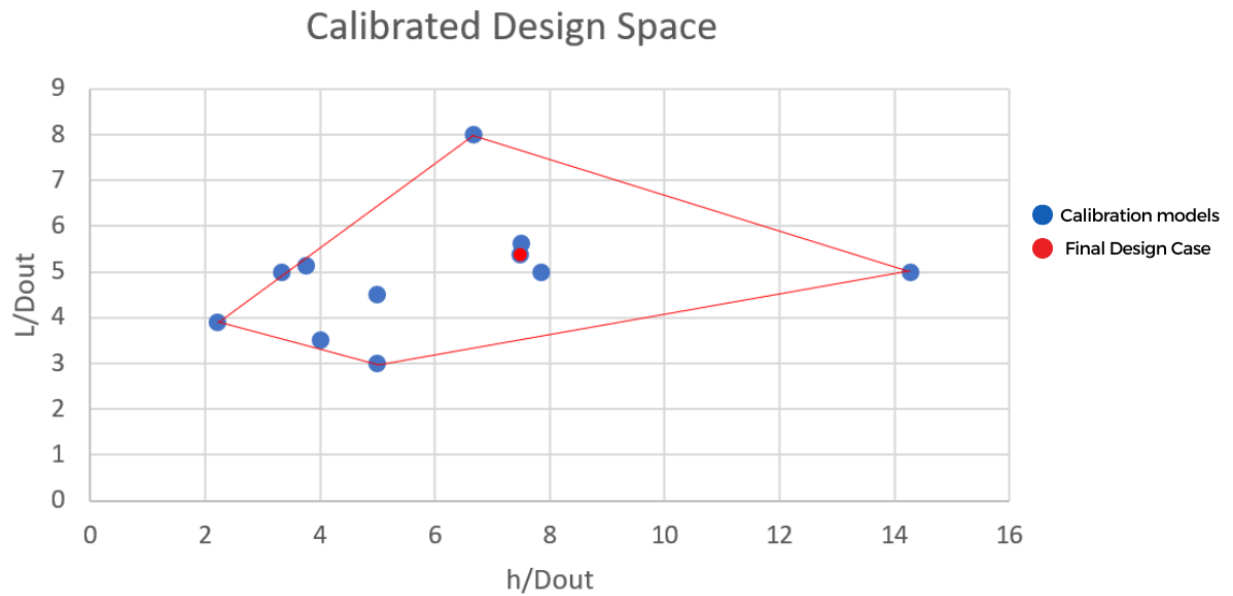


Figure 4.4.3.1 Final Design Case in The Design Space

The final monopile design lies within the boundaries set by the eight calibration models, confirming it is well inside the validated design space. This placement ensures that the 1D model, calibrated using 3D analysis data, can be applied with confidence. The design meets the serviceability requirement of keeping lateral displacement at the mudline below  $0.1 \times D$  under the applied load. Additionally, the close match between 1D and 3D results for rotation adds further confidence in the design's performance, showing that the simplified model provides reliable outcomes within the considered conditions.

## 4.5 Connection Joint Design

Connection joints are vital in monopile foundations by securely linking the monopile to the transition piece or tower and allowing loads to transfer efficiently between structural elements. These joints are subject to high bending, shear, and axial forces from environmental and operational conditions. If not properly designed or constructed, they can become weak points that lead to fatigue damage or stiffness loss over time. Based on the optimised monopile geometry in Table 4.4.1, a conical connection joint can be introduced to link the offshore wind turbine (OWT) tower and the monopile. Offshore Engineering (n.d.) presents a simplified methodology for calculating the geometry of the transition piece, adhering closely to established industry standards, including DNVGL-ST-0126 “Support Structures for Wind Turbines”, DNVGL-RP-C203 “Fatigue Design of Offshore Steel Structures”, and the structural design provisions of API RP 2A-WSD and ISO 19902.

The length of the grouting required ( $L_G$ ) is calculated:

$$L_G = 1.5 \times D_{pile} + 0.5 \quad (4.5.1)$$

$$L_G = 1.5 \times (8.0 \text{ m}) + 0.5 = 12.5 \text{ m}$$

The thickness of the transition piece ( $t_{TP}$ ) and grout ( $t_g$ ) is given according to Bhattacharya (2019) as:

$$t_{TP} + t_g = 0.15 \text{ m} \quad (4.5.2)$$

$$t_{TP} = 0.15 \text{ m} - 0.10 \text{ m} = 0.05 \text{ m}$$

Where the minimum grout thickness recommended in the DNVGL-ST-0126 is 100 mm. Hence, the diameter of the transition piece is calculated:

$$D_{TP} = D_p + 2(t_g + t_{TP}) \quad (4.5.3)$$

$$D_{TP} = (8.0 \text{ m}) + 2(0.15 \text{ m}) = 8.3 \text{ m}$$

The geometry for the transition piece is tabulated in Table 4.5.1. The value for the tower base diameter of 6 m is referred from a study done by Jonkman et al. (2009) regarding a 5 MW wind turbine with a rotor diameter of 126 m, similar to this study. The tower base diameter is required for the installation of the conical joint as illustrated in Figure 4.5.1. The illustration for the monopile cross section and the optimised monopile geometry as presented in respective Figure 4.5.1 and Figure 4.5.2 are drawn using the AutoCAD 2025 software. The overall conceptual design for the optimised monopile and transition piece to support a 6.0 MW offshore wind turbine (OWT) is also drawn and presented in Figure 4.5.3.

Table 4.5.1: Transition Piece Geometry

Transition Piece Geometry	Value
Tower Base Diameter (m)	6.00
Monopile Diameter (m)	8.00
Transition Piece Outer Diameter (m)	8.30
Grout Thickness (m)	0.10
Grouting Length on Monopile (m)	12.5
Grouting Length on Tower (m)	12.5
Total Transition Piece Length (m)	25.0

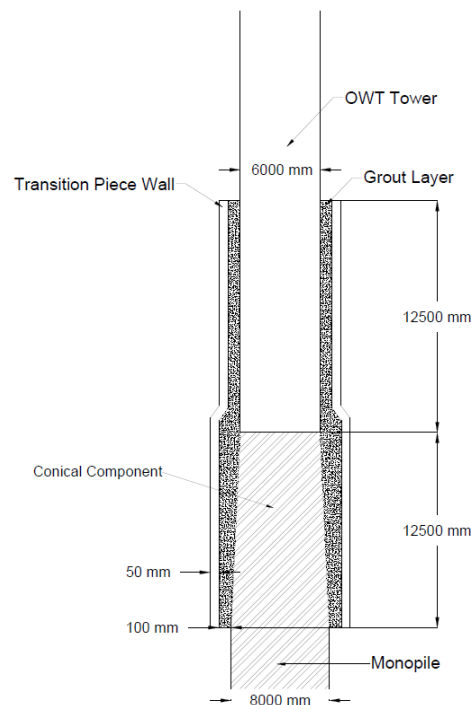


Figure 4.5.1: Cross-section Design of The Transition Piece.

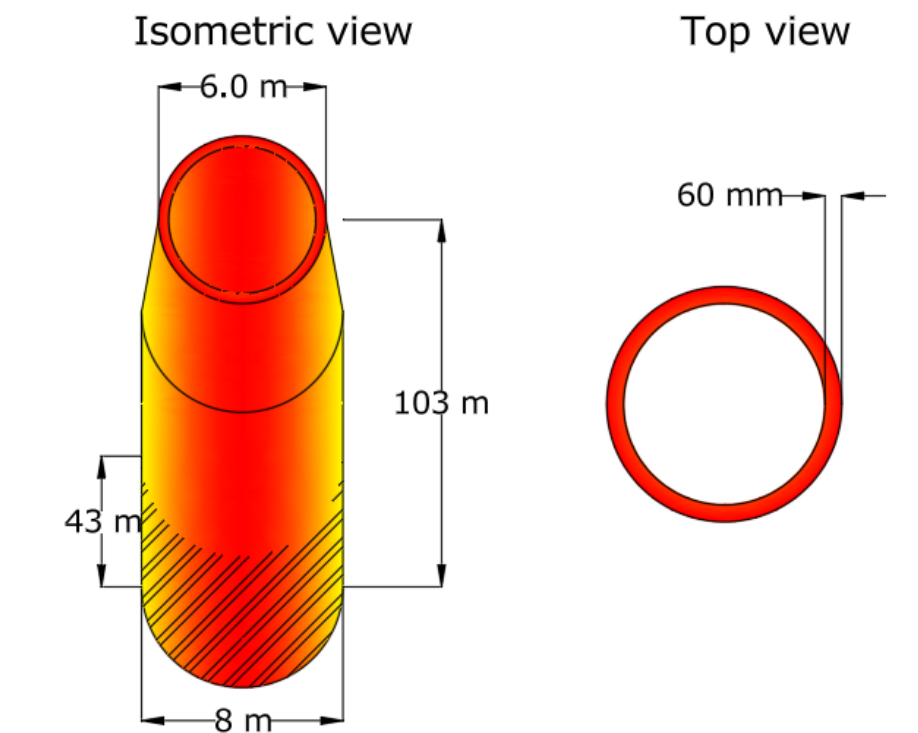


Figure 4.5.2: Optimised Monopile Design.

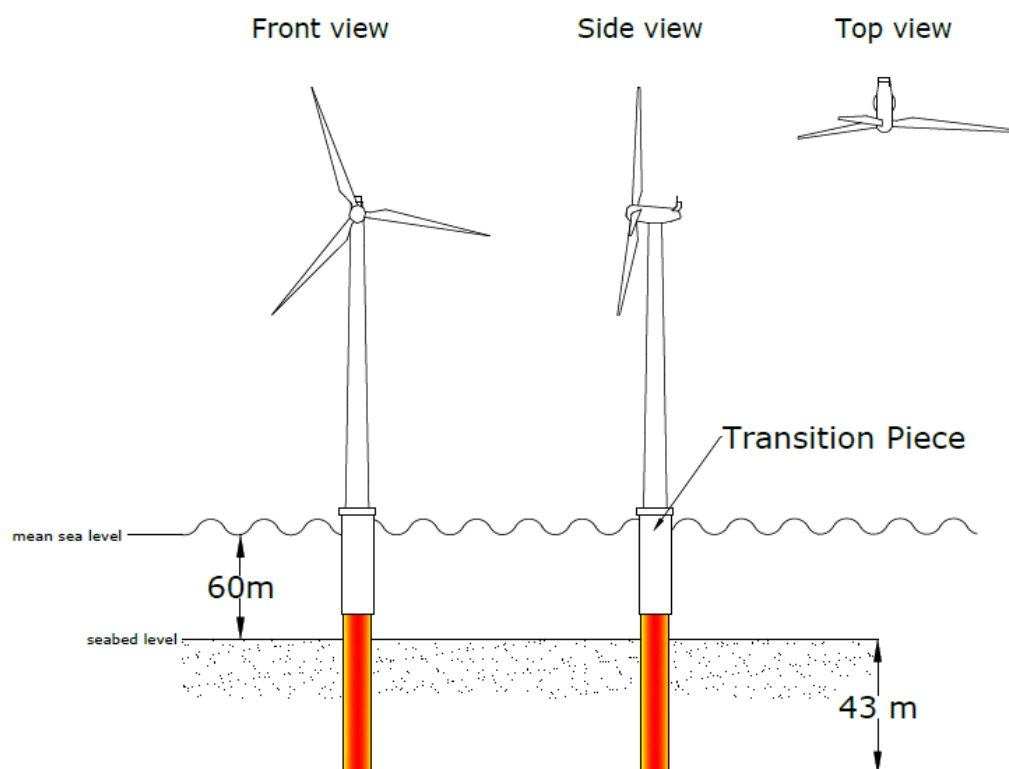


Figure 4.5.3: Conceptual Design of Monopile-supported 6.0 MW Wind Turbine with 43 m Embedment Depth in 60 m Water Depth.

#### 4.6 Sustainability Impact from This Research

The deployment of offshore wind turbines significantly contributes to reducing greenhouse gas emissions and dependency on fossil fuels. Offshore wind systems, especially when strategically placed in low-wind tropical regions like Malaysia, utilize vast marine spaces with minimal land disruption. According to Fauzi et al. (2024), this transition offers a sustainable pathway to meet national energy targets while limiting ecological harm, as the impact on seabed ecology is manageable with proper siting and scour protection. Moreover, wind energy produces no air or water pollution during operation, aligning well with regional goals for climate resilience (Pambudi et al., 2025). The research's focus on optimizing monopile design enhances structural reliability, indirectly preventing environmental degradation due to foundation failure.

Offshore wind power has increasingly become economically viable in low-resource regions due to advances in turbine technology and foundation design. Langer et al. (2022) highlight that with innovations like those presented in this study such as optimizing monopile geometry, the initial capital costs can be reduced while maintaining operational integrity. In the Malaysian context, Nizamani et al. (2024) showed that such advancements could lower the levelized cost of electricity (LCOE), making offshore wind more competitive with traditional energy sources. The findings from this project support these outcomes by demonstrating that SLS-compliant designs with lateral displacement less than  $0.1D_{out}$  and rotation less than  $0.5^\circ$  can maintain safety and performance under tropical loading conditions, thereby minimizing maintenance costs and enhancing economic attractiveness.

Socially, the development of offshore wind farms offers job creation in construction, operation, and maintenance, as well as infrastructure development in coastal communities. Furthermore, increasing energy independence and access contributes to long-term energy security and social equity. As noted by Quirapas and Taeihagh (2021), communities involved in renewable energy projects often report increased public support due to cleaner environments and improved employment. The

current study, by advancing design standards and ensuring structural resilience, plays a foundational role in enabling these broader social benefits, making offshore wind integration more socially acceptable and technically feasible in Malaysia



## **CHAPTER 5**

### **CONCLUSION AND RECOMMENDATIONS**

#### **5.1 Conclusion**

This research comprehensively investigates the design and performance of offshore monopile foundations for wind turbines at a challenging water depth of 60 meters, specifically tailored to the environmental and geotechnical conditions of Malaysia's offshore regions located at Abu Kecil, Kuala Terengganu. The first objective, to investigate the environmental load effects on the wind turbine at this depth, was addressed through a detailed metocean analysis incorporating site-specific wind, wave, and current data from the Abu Kecil offshore region. The most critical loading scenario was identified as an extreme operating gust coinciding with a 50-year return period wave event, resulting in a lateral load of 5,777 kN applied at a hub height of 90 meters. This condition produced an overturning moment of 709 MNm at the mudline, which served as the governing design case.

The second objective focused on designing, analysing, and assessing optimized monopile cross sections for a 6 MW offshore wind turbine. By utilizing PLAXIS Monopile Designer with the PISA methodology and incorporating both one-dimensional and three-dimensional finite element modelling under Timoshenko beam theory, a site-specific and structurally efficient design was achieved. The resulting optimized monopile geometry comprises an outer diameter of 8.0 meters, a wall thickness of 0.06 meters, an embedment depth of 43 meters, and a total length of 103 meters. This configuration was found to ensure both structural integrity and material efficiency under extreme offshore loading conditions.

The third objective, comparing lateral displacements versus horizontal loads across different monopile designs, was met through systematic modelling and simulation. The optimized monopile demonstrated a lateral displacement for the 1D analysis to be 0.09149 meters, while the 3D analysis shows a significantly higher value of 0.4821 meters. However, both conditions are still less than 0.8 meters at the mudline corresponding to less than 0.1 times the pile diameter thereby satisfying the Serviceability Limit State (SLS) criterion for displacement. Moreover, the cross-section rotation at the mudline remained below 0.5 degrees, where the cross-section rotation for the 1D analysis is 0.0065 radians ( $0.372^\circ$ ), while the 3D model gives the result of 0.007 radians ( $0.401^\circ$ ), hence meeting the SLS rotational limit. These outcomes confirm that the proposed design not only withstands the applied environmental loads but also performs reliably within established operational thresholds.

In conclusion, this research has successfully achieved its aims by delivering an optimized monopile design suitable for deeper water applications in Malaysia's offshore zones. The integration of environmental loading analysis, advanced numerical modelling, and compliance with serviceability criteria demonstrates that the proposed foundation design is both technically robust and economically viable for future offshore wind energy development.

## **5.2 Recommendation**

To improve the quality and resilience of future monopile foundation designs for offshore wind turbines, the following recommendations are proposed:

### **5.2.1 Consider Environmental and Geotechnical Uncertainties**

Variations in metocean conditions such as wind, wave, current and soil properties like shear strength and stratification should be addressed using probabilistic approaches. These uncertainties can significantly affect structural performance and must be included in design assessments.

### **5.2.2 Implement Performance-Based Assessment**

A performance-based framework enables engineers to evaluate the probability of exceeding key performance limits, such as lateral displacement and rotation, over the structure's life. This method improves design accuracy by incorporating site-specific hazards and environmental variability (Wang et al., 2022).

### **5.2.3 Refine Numerical Simulations**

Finite element modelling should be combined with nonlinear soil models and dynamic load simulations to capture realistic monopile responses under cyclic and extreme loading. This approach provides more reliable predictions and supports safer foundation designs (Wang et al., 2022).

## REFERENCES

Abdullahi, A., Bhattacharya, S., Li, C., Xiao, Y. and Wang, Y., 2022. Long-term effect of operating loads on large monopile-supported offshore wind turbines in sand. *Ocean Engineering*, 258, p.111809. <https://doi.org/10.1016/j.oceaneng.2021.110404>

Aleem, M., Rahmanli, U., Jindal, S. and Cui, L., 2024. Geotechnical challenges in monopile foundations and performance assessment of current design methodologies. *Ocean Engineering*, 297, Article 116112. 10.1016/j.oceaneng.2024.118469

American Petroleum Institute, 2007. *API RP 2A-WSD: Recommended Practice for Planning, Designing and Constructing Fixed Offshore Platforms – Working Stress Design*. 21st ed. Washington, D.C.: American Petroleum Institute.

API, 2014. *API RP 2A-WSD: Planning, designing and constructing fixed offshore platforms—working stress design*. 22nd ed. Washington, DC: American Petroleum Institute. Available at: [https://www.api.org/~media/files/publications/whats%20new/2a-wsd\\_e22%20pa.pdf](https://www.api.org/~media/files/publications/whats%20new/2a-wsd_e22%20pa.pdf) [Accessed 2 May 2025].

Arshad, M. and O’Kelly, B.C., 2016. *Analysis and design of monopile foundations for offshore wind-turbine structures*. *Marine Georesources & Geotechnology*, 34(2), pp.134–146. Available at: <https://doi.org/10.1080/1064119X.2015.1033070>

Bhattacharya, S., 2019. *Design of foundations for offshore wind turbines*. John Wiley & Sons.

Buljac, A., Kozmar, H., Yang, W. and Kareem, A., 2022. Concurrent wind, wave and current loads on a monopile-supported offshore wind turbine. *Engineering Structures*, 252, p.113554. <https://doi.org/10.1016/j.engstruct.2022.113950>

Byrne, B.W. & Houlsby, G.T., 2003. Foundations for offshore wind turbines. *Philosophical Transactions of the Royal Society A: Mathematical, Physical and Engineering Sciences*, 361(1813), pp.2909-2930.

Cong, N.C., Nizamani, Z., Fakhurddin, K.A., Muhammad, A.K. and Wahab, M.A., 2024. Performance evaluation of the monopile foundation using PISA methodology under extreme loading conditions in Malaysia. *Ocean Engineering*, 309, p.118515.

DNV, 2021. *DNV-RP-C205: Environmental conditions and environmental loads*. Høvik: DNV. Available at: <https://www.dnv.com>

DNV GL, 2016. *DNVGL-RP-C203: Fatigue Design of Offshore Steel Structures*. Det Norske Veritas Germanischer Lloyd. [online] Available at: <https://rules.dnv.com/docs/pdf/DNV/RP/2016-12/DNVGL-RP-C203.pdf> [Accessed 3 May 2025].

DNV GL, 2018. *DNVGL-ST-0126: Support Structures for Wind Turbines*. Det Norske Veritas Germanischer Lloyd. [online] Available at: <https://rules.dnv.com/docs/pdf/DNV/ST/2018-07/DNVGL-ST-0126.pdf> [Accessed 3 May 2025].

Duan, N., 2016. *Mechanical characteristics of monopile foundation in sand for offshore wind turbine*. MSc thesis. University College London. [online] Available at: <https://www.researchgate.net/publication/306347736> [Accessed 1 May 2025].

Fauzi, F.N., Puryantini, N. and Prabowo, A.R., 2024. Implementation Assessment of the offshore wind turbine (OWT) for remote regions' electrification in Indonesia based on geographical potential and economic viability. *Engineered Science Journal*. [online] Available at: <https://doi.org/10.30919/es1295>

Gupta, B.K., 2018. *Soil-structure interaction analysis of monopile foundations supporting offshore wind turbines*. MSc thesis. University of Waterloo. [online] Available at: <http://hdl.handle.net/10012/13546> [Accessed 1 May 2025].

Hallowell, S., Myers, A.T. and Arwade, S.R., 2016. *Variability of breaking wave characteristics and impact loads on offshore wind turbines supported by monopiles*. *Wind Energy*, 19(2), pp.301–316. Available at: <https://doi.org/10.1002/we.1833>

Hau, E. and Hau, E., 2013. The wind resource. *Wind Turbines: Fundamentals, Technologies, Application, Economics*, pp.505-547.

Houlsby, G.T., Ibsen, L.B. & Byrne, B.W., 2005. Suction caissons for wind turbines. *Frontiers in Offshore Geotechnics*, pp.75-94

Jana, K., Sarkar, R. and Bhattacharya, S., 2024. Adequacy and performance of monopile foundations of multi-megawatt offshore wind turbines along Indian coastal regions. *Ocean Engineering*, 307, p.118173.

Jindal, S. (2024) *Soil damping curves for monopile supported offshore wind turbine structures*. PhD thesis, University of Surrey. Available at: [https://openresearch.surrey.ac.uk/view/pdfCoverPage?instCode=44SUR\\_INST&filePid=13213175380002346&download=true](https://openresearch.surrey.ac.uk/view/pdfCoverPage?instCode=44SUR_INST&filePid=13213175380002346&download=true) [Accessed: 1 May 2025].

Jindal, S., Rahmanli, U., Aleem, M. and Cui, L., 2024. Geotechnical challenges in monopile foundations and performance assessment of current design methodologies. *Ocean Engineering*, 286, p.116186. <https://doi.org/10.1016/j.oceaneng.2024.118469>

Jonkman, J., Butterfield, S., Musial, W. and Scott, G., 2009. *Definition of a 5-MW reference wind turbine for offshore system development*. NREL/TP-500-38060. Golden, CO: National Renewable Energy Laboratory (NREL). [online] Available at: <https://www.nrel.gov/docs/fy09osti/38060.pdf> [Accessed 3 May 2025].

Kresning, B., Hashemi, M.R., Shirvani, A. and Hashemi, J., 2024. Uncertainty of extreme wind and wave loads for marine renewable energy farms in hurricane-prone regions. *Renewable Energy*, 220, p.119570.

Langer, J., Simanjuntak, S., Pfenninger, S. and Laguna, A.J., 2022. How offshore wind could become economically attractive in low-resource regions like Indonesia. *iScience*, 25(12). 10.1016/j.isci.2022.104945

LeBlanc, C., Houlsby, G.T. & Byrne, B.W., 2010. Response of stiff piles in sand to long-term cyclic lateral loading. *Geotechnique*, 60(2), pp.79-90.

Manwell, J.F., Branlard, E., McGowan, J.G. and Ram, B., 2024. *Wind Energy Explained: On Land and Offshore*. John Wiley & Sons.\

Martínez, E., Sanz, F., Pellegrini, S., Jiménez, E. and Blanco, J., 2009. Life-cycle assessment of a 2-MW rated power wind turbine: CML method. *The International Journal of Life Cycle Assessment*, 14, pp.52-63.

Maurizio Collu, 2015, *Why Do We Need Different Types of Wind Turbines* [Online]. Available at: <https://www.weforum.org/agenda/2015/01/why-we-need-different-types-of-wind-turbines/> [Accessed: 26 August 2024].

McKinsey & Company, 2023. *Global Energy Perspective 2023*. [online] Available at: <https://www.mckinsey.com/business-functions/sustainability/our-insights/global-energy-perspective-2023> [Accessed 25 Aug. 2024].

Morten, D., Ben, B., 2021. GWEC, Global Wind Energy Report.

Murphy, G., Igoe, D., Doherty, P. and Gavin, K., 2018. 3D FEM approach for laterally loaded monopile design. *Computers and Geotechnics*, 100, pp.76-83. <https://doi.org/10.1016/j.compgeo.2018.03.013>

Nadzari, N.A., 2007. *Soil Investigation for Suriya-B Location, Offshore Terengganu*, Kuala Lumpur.

Nizamani, Z., Muhammad, A.K., Ali, M.O.A., Wahab, M.A., Nakayama, A. and Ahmed, M.M., 2024. Renewable wind energy resources in offshore low wind speeds regions near the equator: A review. *Ocean Engineering*, 311, p.118834.

Offshore Engineering, n.d. Structural dimensions – Monopile foundation design example. *OffshoreEngineering.com*. [online] Available at: <https://www.offshoreengineering.com/wind-monopile-design/structural-dimensions-monopile-foundation-design-example/> [Accessed 3 May 2025].

Page, A.M., Skau, K.S., Jostad, H.P. and Eiksund, G.R., 2017. A new foundation model for integrated analyses of monopile-based offshore wind turbines. *Energy Procedia*, 137, pp.145–154. <https://doi.org/10.1016/j.egypro.2017.10.337>

Pambudi, N.A., Ulfa, D.K., Nanda, I.R., Gandidi, I.M. and Wiyono, A., 2025. The Future of Wind Power Plants in Indonesia: Potential, Challenges, and Policies. *Sustainability*, 17(3), p.1312. <https://doi.org/10.3390/su17031312>

Petronas, 2009. Metocean Design Data for ABU and PUTERI.

PLAXIS, 2018. *PLAXIS Monopile Designer manual*. Edited by S. Panagoulas, R.B.J. Brinkgreve and L. Zampich. Delft, Netherlands: PLAXIS bv, a Bentley Systems company.

Qin, M., Shi, W., Chai, W., Fu, X., Li, L. and Li, X., 2023. Extreme structural response prediction and fatigue damage evaluation for large-scale monopile offshore wind turbines subject to typhoon conditions. *Renewable energy*, 208, pp.450-464.

Quirapas, M. and Taeihagh, A., 2021. Ocean renewable energy development in Southeast Asia: Opportunities, risks and unintended consequences. *Renewable and Sustainable Energy Reviews*, 137, p.110403. <https://doi.org/10.1016/j.rser.2020.110403>

Randolph, M.F., Dolwin, R. and Beck, R., 1994. Design of driven piles in sand. *Geotechnique*, 44(3), pp.427-448.

Whitehouse, R.J.S., Harris, J.M., Sutherland, J. & Rees, J., 2011. The nature of scour development and scour protection at offshore windfarm foundations. *Marine Pollution Bulletin*, 62(1), pp.73-88.



Satari, S.Z., Zubairi, Y.Z., Hussin, A.G. and Hassan, S.F., 2015. Some statistical characteristic of Malaysian wind direction recorded at maximum wind speed: 1999-2008. *Sains Malaysiana*, 44(10), pp.1521-1530.

Sustainable Energy Development Authority (SEDA) Malaysia, n.d. *Feed-in Tariff (FiT) Mechanism*. [online] Available at: <https://www.seda.gov.my/reportal/fit/> [Accessed 26 Aug. 2024].

Sustainable Energy Development Authority (SEDA) Malaysia, n.d. *About SEDA*. [online] Available at: <https://www.seda.gov.my/> [Accessed 26 Aug. 2024].

Taşbaşı, A.D., 2024. *Preliminary geotechnical design of offshore wind turbine monopiles in Türkiye using FEM* (Master's thesis, Middle East Technical University).

Tombari, A., Rostami, R. and Mackay, E., 2025. Stiffness-proportional foundation damping to linearise soil–monopile interaction models for wind turbines. *Soil Dynamics and Earthquake Engineering*, 195, p.109387. <https://doi.org/10.1016/j.soildyn.2025.109387>

Versteijlen, W.G., Metrikine, A.V. and Van Dalen, K.N., 2016. A method for identification of an effective Winkler foundation for large-diameter offshore wind turbine support structures based on in-situ measured small-strain soil response and 3D modelling. *Engineering Structures*, 124, pp.221-236. <https://doi.org/10.1016/j.engstruct.2016.06.007>

Wang, C., Wu, Q., Zhang, H. and Liang, F., 2024. Effect of scour remediation by solidified soil on lateral response of monopile supporting offshore wind turbines using numerical model. *Applied Ocean Research*, 150, p.104143.

Wang, S., Larsen, T.J. and Bredmose, H., 2021. Ultimate load analysis of a 10 MW offshore monopile wind turbine incorporating fully nonlinear irregular wave kinematics. *Marine Structures*, 76, p.102922. <https://doi.org/10.1016/j.marstruc.2020.102922>

Wang, T., Zhang, Z., Zhang, J., Chen, Z., Xian, J. and Zhang, L., 2022. Performance-based assessment of the monopile foundation of offshore wind turbines. *Ocean Engineering*, 266, p.113083.

wind-turbine-models.com, 2024. *Siemens SWT-6.0-120 Wind Turbine*. Available at: <https://en.wind-turbine-models.com/turbines/159-siemens-swt-6.0-120> [Accessed 27 August 2024].

Wu, X. et al., 2019. Foundations of Offshore Wind Turbines: A Review. *Renewable and Sustainable Energy Reviews*, 104, pp.379–393.

Zeng, X., Shi, W., Michailides, C., Zhang, S. and Li, X., 2021. Numerical and experimental investigation of breaking wave forces on a monopile-type offshore wind turbine. *Renewable energy*, 175, pp.501-519.  
<https://doi.org/10.1016/j.renene.2021.05.009>

## APPENDICES

### APPENDIX A: DEPTH VARIATION FUNCTIONS

Variable on x-axis	Definition
$\bar{\nu}_{pu}$	normalised ultimate lateral displacement
$\bar{p}_u$	normalised ultimate lateral soil reaction
$k_p$	normalised initial stiffness of the lateral soil reaction
$n_p$	normalised curvature of the lateral soil reaction
$\bar{\psi}_{mu}$	normalised ultimate rotation
$\bar{m}_u$	normalised ultimate moment reaction
$k_m$	normalised initial stiffness of the moment reaction
$n_m$	normalised curvature of the moment reaction

#### Shaft Depth Variables

Fitting parameter	Definition
$\bar{\nu}_{Hu}$	normalised ultimate lateral base displacement
$\bar{H}_{Bu}$	normalised ultimate lateral base soil reaction
$k_H$	normalised initial stiffness of the lateral base soil reaction
$n_H$	normalised curvature of the lateral base soil reaction
$\bar{\psi}_{Mu}$	normalised ultimate base rotation
$\bar{M}_{Bu}$	normalised ultimate moment base reaction
$k_M$	normalised initial stiffness of the base moment reaction
$n_M$	normalised curvature of the base moment reaction

#### Base Depth Variables

APPENDIX B:  
PUBLICATIONS

1. Z. Nizamani, Loh Kein Yuin, M. Azeem, A. Nakayama. Performance evaluation of offshore wind turbine support structures - A review. 14th International Conference on Renewable Energy Research and Applications (ICRERA 2025) held at Vienna, Austria, October 27 – October 30, 2025. (Paper to be published in IEEE Xplore)
2. Loh Kein Yuin and Z. Nizamani. Optimised Design of The Offshore Monopile Foundation Under Extreme Conditions. Paper in submission to the Journal of Ocean Engineering, Elsevier publications.